Efficient Method for Geometry Independent Multipactor Modelling

by

Aviviere Telang

A thesis
presented to the University of Waterloo
in fulfillment of the
thesis requirement for the degree of
Master of Applied Science
in
Electrical and Computer Engineering

Waterloo, Ontario, Canada, 2009

I hereby declare that I am the sole author of this thesis. This is a true copy of the thesis, including any required final revisions, as accepted by my examiners.

I understand that my thesis may be made electronically available to the public.

Abstract

As modern satellite communication systems move toward multi-carrier high power communications, there is an increased need for high-power RF devices in the space industry. However, at high-power some RF devices have exhibited an electron plasma (multipactor electron avalanche discharge) that severely damages the RF device and could render it unusable. This is especially a problem in space where repairs to communication equipment is cost-prohibitive.

As a result, a number of models have been developed in recent years to predict the onset of multipactor discharge. However, most existing models can only analyze selected geometries and they also require a large number of electrons to predict the power at which multipactor discharge will occur. This has placed a limitation on the types of RF structures that can be analysed for multipactor breakdown.

This research work, uses a new generalized procedure to develop an efficient multipactor model that could be used to analyze the complex structures found in the commercial space industry, by coupling EM field information from established industry-standard EM solvers. A robust secondary emission model is also developed in order to model the advanced phenomenoligcal characterisitcs of secondary emission that are not taken into account in other models. The result of the generalized approach taken in this research is a highly efficient multipactor model that requires far fewer electrons to be analysed in order to converge to accurate results, and the ability to analyse more complex RF structures than current models.

Multipactor analysis for different structures were performed, and the breakdown results predicted by this model were in good agreement with other models where expected. However, for other cases where certain simplifying assumptions do not hold true, such as higher order waveguide multipaction and high impedance transmission line multipaction, results provided by this model were found to be more accurate and efficient when compared to other models.

Acknowledgements

I would like to thank Antonio Panariello at COM DEV for his hardwork and dedication in helping me during the course of my research at COM DEV. Without the vision and passion he has and continues to have, this work would not have been so successful. I would also like to thank my research supervisors Professor Ming Yu (Director of Research and Development at COM DEV) and Professor Raafat Mansour for their guidance and direction everytime I needed it.

To mom, dad, Tyron and Heather thank you for your patience and understanding through out my studies, even the little things you did for me was invaluable and helped me significantly.

Finally, I want to give thanks to the Lord Jesus Christ without whom, I might have gained this whole world, but lost my very soul....

To my Mom, Dad, Chickoo and Heather

Contents

List of Figures **ix**

1 Introduction **1**

1.1 Scope 1

1.2 Motivation 2

1.3 Research Objectives and Contributions 4

1.4 Thesis Organization 5

2 Literature Review **6**

2.1 Multipactor Breakdown Basic Theory 6

2.1.1 Secondary Emission 7

2.1.2 Multipactor Order 10

2.1.3 Phase Focusing 11

2.1.4 Susceptibility Zones 12

2.1.5 Saturation 15

2.1.6 Particle Trajectory 16

2.2 Current Multipactor Models 17

2.2.1 Full-wave EM Simulation Tool [FEST] 17

2.2.2 TRAK_RF 19

2.2.3 MEST - Multipactor Electron Simulation Tool 21

2.2.4 MultP 21

2.2.5 ESA Multipactor Calculator 22

2.2.6 Sazontov Models 23

2.2.7 Comparison of Models 24

2.2.8 Other Simulators 26

3 Analytical Particle Trajectory Tracker **27**

3.1 Analytical Formulation 27

3.1.1 Parallel Electrodes 28

3.1.2 Rectangular Waveguide 29

4 Secondary Emission Model **39**

4.1 Secondary Emission Yield 40

4.1.1 Vaughan Formulation 42

4.1.2 Modification of Vaughan formulation: 44

4.1.3 Modified Vaughan Formulation 44

4.2 Incident Impact Angle Calculation 46

4.3 Emission Direction 47

4.4 Trajectory Termination 51

4.5 Advanced Concepts in Secondary Emission 51

4.5.1 Out of Phase Secondary Emission 52

4.5.2 Emission Energy 53

4.5.3 Reflected Primary Particles 54

4.5.4 True Secondary Electron Tracking 56

4.6 Conclusion 57

5 Multipactor Model & Simulation Results **59**

5.1 Numerical Engine 60

5.1.1 Time and Phase Advancement 61

5.1.2 Field Interpolation 63

5.1.3 Trajectory Differential Equations 64

5.2 Multipactor Model Algorithm 65

5.3 Simulation Results 70

5.3.1 Waveguide Simulations 70

5.3.2 Square-Axial Transmission Line 74

5.4 Contributions of Multipactor Model 80

5.4.1 Key Techniques 81

5.5 Key Contributions 82

6 Conclusion and Future Work **87**

6.1 Contribution of Research 87

6.2 Conclusion 88

6.3 Future Work 89

References **90**

List of Figures

1.1 Generalized procedure used in this research 4

2.1 Multipactor Build-Up 7
2.2 Typical SEY curve showing components of secondary emission . . . 8
2.3 Creation of Secondary Electrons[1] 9
2.4 Typical SEY curve for 0° incidence 10
2.5 Constant Velocity Multipactor Chart 13
2.6 Hatch & Williams Multipactor Chart 14
2.7 Woode and Petit Multipaction Charts for Aluminum[2] 15
2.8 Woo Multipactor Chart for Coaxial Lines 16
2.9 Conformal Mesh in TRAK_RF showing meshing of curves 20
2.10 Table 3.4 - MultP Summary 22

3.1 Coordinate System for Parallel Plate Setup 28
3.2 Coordinate system for Small Gap Rectangular Waveguide showing field vectors 30
3.3 Expected velocity curve for rectangular waveguide 30

4.1 Typical SEY curve for 0° incidence and 60° 41
4.2 Typical Bruining curve for g_n as z is swept, to find z_m 42
4.3 Cosine Law Distribution 47
4.4 Switching between GCS (XYZ) to LCS ($X'Y'Z'$) 50
4.5 Energy distribution curve for Copper surface [3] 55

5.1 Cube showing Trilinear Cubic Interpolation 63
5.2 Generalized Procedure used in this research 66
5.3 Particle Growth Curves for 9th Order Multipaction in Waveguides . 73

5.4 2D view of Field vectors for 30 ohm square-axial TL 74
5.5 3D view of Field Vectors for 30 ohm square-axial TL 75
5.6 2D view of Field vectors for 90 ohm square-axial TL 76
5.7 3D view of Field Vectors for 90 ohm square-axial TL 77
5.8 Particle Trajectory for 3rd order multipactor in Sq-Ax (Low V) . . 84
5.9 Particle Trajectory for 3rd order multipactor in Sq-Ax (High V) . . 85
5.10 Particle Trajectories for 3rd order multipactor breakdown in Sq-Ax 86

Chapter 1

Introduction

The emission of electrons through avalanche-like multiplication at RF frequencies known as multipaction was discovered by P. Farnsworth in 1934 [4]. Although Farnsworth did realize the ability of multipaction to cause damage, he viewed it as an effective way to amplify signals. After a few years of research, he eventually used this phenomenon to amplify very weak signals such that it was possible for his television camera tubes to pick up outdoor scenes that had no natural sunlight. He called these television camera tubes "Multipactors".

By the mid-1940s the name moved towards describing the phenomenon rather than the tubes, and today it is used either as a noun (multipaction) or a verb (multipact)[4]. Researchers have been studying multipaction for many years, trying to find out what causes it, how to suppress it and in some cases how to exploit it.

1.1 Scope

The multipactor phenomenon has been studied in a number of different fields in the past. Particle physicists have studied the phenomenon in relation to plasma science and particle beam dynamics where as engineers have used the phenomenon to amplify signals in vacuum tubes and klystrons [4]. Depending on the application then, the multipactor phenomenon can be viewed either as a valuable tool or an undesirable effect. This research work focuses on the effects of multipaction breakdown for RF devices in the space-industry. In the space-industry, multipactor breakdown is viewed as an undesirable phenomenon since it can cause irreparable damage to RF devices on board satellites and could render the device unusable. In the context of this research, the typical RF devices for space applications are waveguides, diplexers, filters and multiplexers. While the power handling of these devices has increased in recent years, so has their geometric complexity. Since most multipactor models are make a number of simplifying assumptions and are based

on simple geometries, current models are becoming increasingly inaccurate and inefficient as device geometries become more complex. This research work begins the development of more efficient multipactor models that eventually could be used to analyze more complex structures used in the space-industry. This research work was directed at COM DEV in Cambridge, Ontario, Canada in partnership with the University of Waterloo, Waterloo, Ontario, Canada.

1.2 Motivation

Multipaction has been a major topic of interest in space-research due to the damaging effects it has on space hardware operating in vacuum. Since low frequency waves cannot propagate through the ionosphere, satellite-communications ("satcom") use microwave frequencies to communicate with terrestrial base-stations. Microwave frequencies also allow engineers to design electronics that are compact (and therefore light weight) reducing payload, which is essential for satellite systems. This also makes microwave systems operating in vacuum susceptible to multipaction. Multipactor breakdown is a critical area in space-research because in extreme cases it can cause permanent damage to microwave communication systems on-board spacecraft, which is difficult or impossible to repair or replace after launch[2].

As modern satcom systems moved toward multi-carrier high power communications, multipactor prediction becomes even more critical as it can increase intermodulation levels and cause abrupt discontinuities in transmission, severely degrading system performance. Multipaction can also degrade the return loss of the satcom system (if output power is reduced) and when sustained for a sufficient amount of time, it can cause outgassing of device walls which increases the pressure inside the device and initiates a more destructive phenomenon: corona discharge [5],[6]. As a result, the space-industry has had a renewed interest to find ways to model and suppress multipactor breakdown in microwave structures, in order to be able to increase the power handling capability of RF devices. In order to achieve this however, an accurate model is required to predict the breakdown level for various space-borne RF devices such as waveguides and multiplexers.

Multipaction is triggered when free electrons that may be generated by cosmic radiation for space-borne equipment are subject to electromagnetic (EM) fields that are strong enough to lift these electrons off the surface walls. Due to vacuum conditions the electrons can be accelerated very quickly toward another surface wall since there are no gas particles to collide with and slow the electrons down. Upon impact with the wall, depending on the energy, angle and secondary emission characteristics of the wall surface, these impacting electrons can cause secondary electrons to be emitted. If the RF signal then changes phase at this time, these secondary electrons can then be accelerated to the other device wall generating even more secondary electrons and enabling an exponential growth in the electron population. This build-up, known as an RF discharge can be sufficiently large to reflect the incident power damaging the system.

Past works have focused their research on an analytical study of multipactor modelling, deriving equations to predict the multipaction breakdown for simple geometries. In recent years most other multipactor models are only able to predict multipactor breakdown for a selected set of geometries and are also very inefficient due to the number of electrons the models require for simulation results to converge [7],[5],[8],[9].

1.3 Research Objectives and Contributions

Referring to Fig. 1.1 this research develops an efficient and generalized procedure that could potentially predict the onset of multipaction for complex microwave structures. In order to achieve this objective, this research develops a vigorous secondary emission model (Component 1 in Fig. 1.1) and uses an efficient numerical engine (Component 2 in Fig. 1.1) to couple the field information from established industry-standard commercial EM solvers (Component 3 in Fig. 1.1). in order to create a more efficient multipactor model.

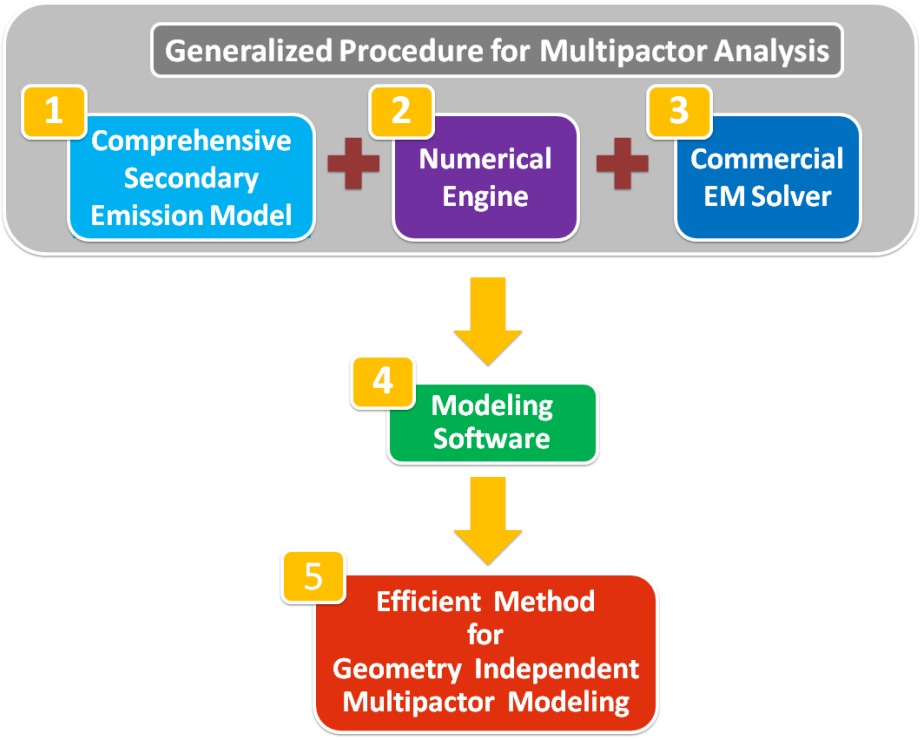

Figure 1.1: Generalized Procedure used in this research to develop an efficient method for geometry independent multipactor modeling

The contribution of this research is that the multipactor model that has been developed using this generalized procedure is much more efficient that other multipactor models since it requires far fewer electrons to provide accurate predictions of multipactor breakdown levels. Additionally, since the procedure developed in this research abstracts the complexities of EM field analysis and moves it to well established commercial EM solvers (CEM), this multipactor model can be potentially used to predict multipactor breakdown for complex RF structures found in the space-industry.

1.4 Thesis Organization

This thesis is organized as follows: Chapter 2 presents a brief literature review and discussion of the key concepts of multipaction. Chapter 2 also reviews some of the other multipactor models in recent development. A few multipactor models are compared to each other and details of other published models are also outlined.

Chapter 3 presents the analytical version of the particle trajectory tracker. The trajectories for two geometries; parallel-plane and rectangular waveguide are presented in this chapter. Since multipaction for a parallel-plate geometry has been studied in detail, it provides for an excellent preliminary calibration point for the model.

Chapter 4 presents the robust secondary emission model in detail. Since this research aims to develop a generalized procedure for multipactor breakdown, many aspects of the secondary emission process that have not been accounted for in other multipactor models are considered in this research.

Chapter 5 presents the numerical engine that solves the equations of motion differentially. This engine replaces the analytical engine in the previous chapter. This also details the final procedure developed in this research and presents the simulation results (with comparisons to other models) of two structures.

Chapter 6 summarizes the conclusions and findings derived from this research and summarizes the key contributions of this research. Finally, direction for future work in this area is also provided.

Chapter 2

Literature Review

Chapter Summary

This chapter reviews some of the basics of multipactor breakdown. The major topics discussed are the multipactor resonance condition, multipactor order, the secondary emission process and susceptibility charts that have been widely accepted by researchers. Many of these topics will be discussed in more detail in the following chapters. The chapter also reviews some of the current multipactor prediction models being used by a number of research teams in the academic arena. A brief summary of each multipactor model is presented, outlining strengths and limitations as stated in published materials. The chapter ends with a comparison of the major multipactor models and a list of other models that have been widely cited for the interested reader to review.

2.1 Multipactor Breakdown Basic Theory

Even though there are two kinds of multipaction, single surface and double (multi) surface, this thesis will focus on the double surface multipaction since it is the predominant case in satcom systems, however the models developed are general and the final model can predict single-side multipaction breakdown levels as well.

Concisely stated, multipaction starts out when free electrons in vacuum electronic devices are lifted off the device surface (Fig. 2.1a) and accelerated toward another device surface due to high-power EM fields (Fig. 2.1b). Depending on the EM field intensity, these electrons may impact the wall with enough energy to release more than one secondary electron from the surface of the structure (Fig. 2.1c). If, at this exact moment of impact, the field switches direction the emitted electrons are accelerated towards the opposite wall, liberating even more electrons upon impact(Fig. 2.1d), this is known as the resonance condition. If this process

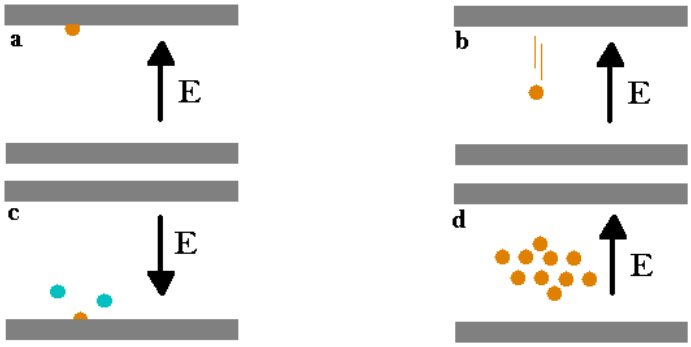

Figure 2.1: Multipactor Build-up, (a) Free electron lifted from surface, (b) electron accelerated to opposite wall, (c) secondary particles emitted (d) formation of electron cloud over time

is sustained for a few RF cycles, the electron- population grows exponentially and a multipactor discharge is created.

Experimental results show that this exponential discharge does not continue to grow indefinitely but eventually saturates[10]. A number of theories have been presented in literature to explain the cause of this, but most agree that the underlying cause is that of the space-charge effect also known as the electron cloud effect[11]. This is discussed in later sections.

2.1.1 Secondary Emission

This section provides a brief background on secondary emission, introducing general concepts and equations.

In order to develop models for the secondary electron emission (SEE) phenomenon, numerous researchers have been working together to develop formulae to accurately describe the phenomenon. Many formulae are empirically obtained using curve fitting techniques on measured data from numerous test set-ups. This report primarily presents the work of J.R.M Vaughan (who has many publications on the subject and has since been cited by many researchers), whose well-accepted secondary emission yield (SEY) formulae is used in this research. As shown in Fig. 2.2 the total secondary yield is modeled as the sum of true secondary-electrons, inelastically reflected (rediffused or RD) primary particles and in-elastically reflected (backscattered or BS) primaries [12].

Thus:

$$SEY_{tot}(E_p, \theta_p) = TS(E_p, \theta_p) + BS(E_p, \theta_p) + RD(E_p, \theta_p) \tag{2.1}$$

where E_p is the energy of the impacting particle and θ_p is the angle of incidence for the impact.

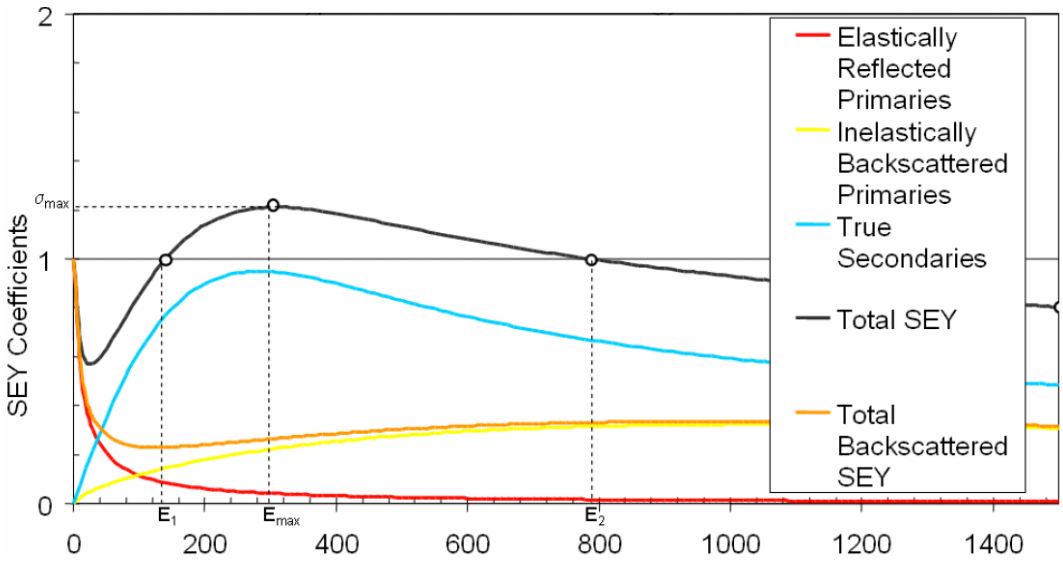

Figure 2.2: Typical SEY curve showing components of secondary emission - True Secondary, Rediffused and Backscattered primaries [$\theta_p = 0$ degrees] [12]

In order to understand Fig. 2.2, each component of the total SEY will be briefly discussed to give the reader a sense of the physical process that creates them, and their emission energy levels. Referring to Fig. 2.3 the three types of electrons emitted upon impact can be classified into three categories each with different probability models of emission[1], they are:

1. **True Secondaries (Low Energy):** True secondary particles, are the particles that are generated in an inelastic collision between a primary free electron and an atom close to the surface of the material. The kinetic energy that is lost by a primary electron upon collision with the atom, is absorbed by the atom, and is radiated soon after so that the atom can return to the ground state quickly. However, if a collision occurs when the electric field is high enough, a primary particle can knock off an electron from the atom, creating a secondary (free) electron, and a positive ion. These secondary electrons are created (launched) with relatively lower energies. The emission energy of true secondaries has been somewhat arbitrary based on empirical measurements, but has been conventionally chosen to be in the range of about around 0 to 50eV [1], [13].

2. **Elastically Reflected or Elastically Backscattered (High Energy):** Even though these particles are considered part of the total secondary yield, these particles are actually high-energy primary electrons that simply bounce off the material surface. This collision is a (almost) strictly elastic collision since the kinetic energy involved in the collision is not converted to other forms of energy, i.e. the kinetic energy is conserved, and no energy is used

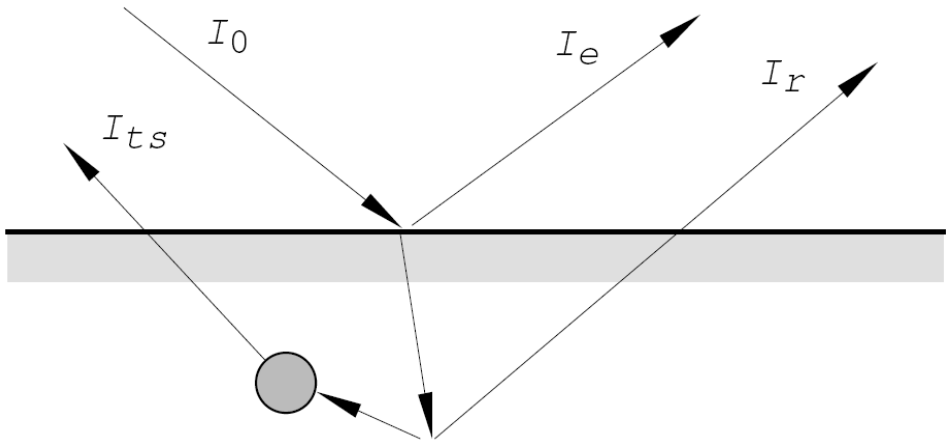

Figure 2.3: Creation of Secondary Electrons[1]

to change the internal state of the atom, so no "true-secondary" electrons are produced. Due to the nature of this type of collision, elastically reflected electrons are reflected with energies very close (around 99%) to the primary electrons. The range of energies for these electrons is typically around 99% of the energy of the impacting electron [13], [14].

3. **In-elastically Reflected or Re-diffused (Mid-Energy)**: Unlike the elastically reflected electrons that bounce off the material surface, re-diffused electrons are primary electrons that penetrate the surface, interact with atoms in a more complicated way, and are then reflected back into the vacuum. Due to the in-elastic nature of these collisions, these primary electrons lose some of their kinetic energy upon collision, and are launched with lower energies than their elastically backscattered counterparts. These particles are launched with energies in the range between 50ev up to the energy of the impacting electron [13], [14] .

A typical SEY curve for a orthogonal impact (0° with respect to the surface normal) is shown in Fig. 2.4, where V_1 and V_2 are called the first and second crossover points. At these two points, the SEY (δ) is exactly one, and no multipaction can occur since there can be no electron population growth. In order for multipaction to occur, the SEY must be greater than 1 in order to create an exponential electron growth, and so the range of voltages between the two crossover points are of concern in high power devices. The existence of the two crossover points can be easily explained. If the energy of the impacting particle is too low, the SEY < 1 since there isn't enough impact energy to eject electrons from the surface of the material. If the energy of the impact electron is too high however, the SEY <1 because the penetration depth of the electron is too deep before it can impart energy to potential secondaries (high energy impact electrons can hit electrons on the

surface of the material, however due to their high energy (speed) they are not able to transfer enough energy to the surface particles since they do not have enough time to interact with the surface particles. As the particles slow down within the metal, they are able to transfer more energy to other free electrons, however by this time they have penetrated the surface quite deep and it is highly unlikely that secondaries can be ejected from the surface. $V_{\max}$ is the impact voltage at which the maximum SEY ($\delta_{\max}$) has been measured and V_o is the impact voltage at under which the SEY converges to zero. In other words, secondary electrons that impact a surface with an energy that is less than V_o do not create any secondary electrons.

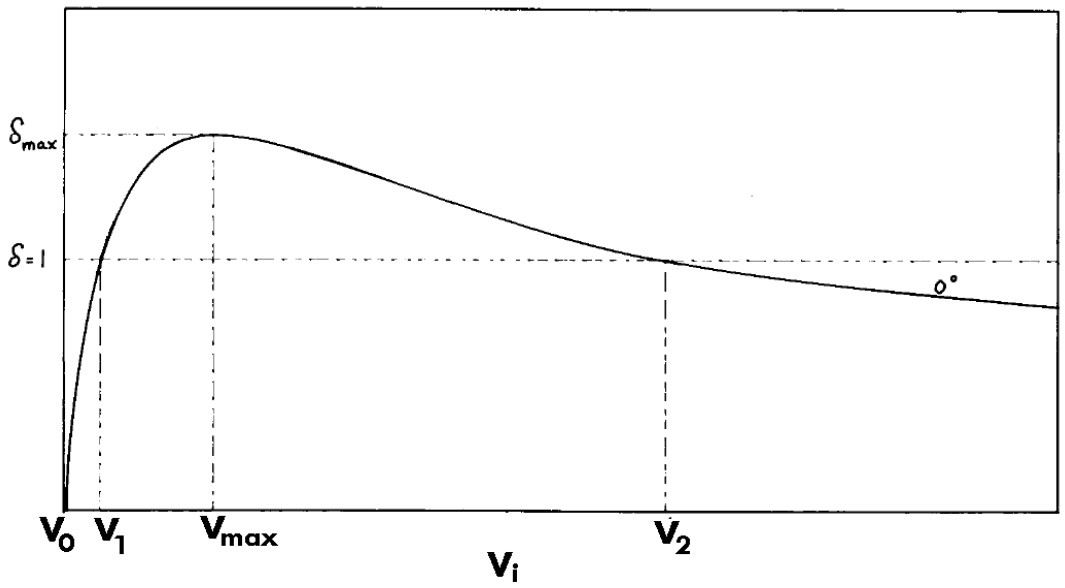

Figure 2.4: Typical SEY curve for 0° incidence

2.1.2 Multipactor Order

In order for multipaction to occur, a resonant condition must be met. The resonant condition states that the electrons being lifted off the device wall should traverse the gap in an odd number of half RF cycles. This means that the electron must impact the wall during the accelerating (positive) phase of the RF field, ensuring that the returning electrons are subject to the same conditions in reverse, and the electron growth can be sustained. The number of half-cycles defines the multipactor mode order. The mode-order has a strong impact on how quickly the electron population in the RF discharge grows and the growth can be stated by:

$$N(t) = N_0 \sigma_g^{\left(\frac{2ft}{n}\right)} \tag{2.2}$$

if no saturation mechanism is considered[15]. Here N is the electron population at time t, N_0 is the number of seed particles, n is the multipactor order and f is the

frequency of the applied RF signal, and σ_g is the average secondary yield of the respective generation. Eqn. 2.2 shows that an increasing mode order results in a decreasing population growth rate and therefore it can be said that in many systems the higher order multipactor are not as critical as the lower order multipactor.

Experimentally, multipactor orders that occur in satcom systems are usually in the range of first to ninth order, although higher order multipaction has been recorded as well[4].

2.1.3 Phase Focusing

As discussed earlier multipaction is highly dependent on the resonance condition being met, and as such is very sensitive to the phase angle of the EM field at which an electron is emitted. In order for an electron to participate in the breakdown discharge, it must be close to the nominal (resonant) phase. The nominal phase is defined as the (EM field) phase angle at which an electron is emitted such that it is able to traverse the gap in exactly n-half cycles and impact with sufficient energy to create secondary electrons. After some simplification[15] the phase α, can be found as:

$$\alpha_n = \arctan\left[\frac{1}{2}\left(\frac{2\omega d - n\pi(v_1 + v_0)}{v_1 - v_0}\right)\right] \tag{2.3}$$

where d is the gap distance, ω is the angular frequency of the RF signal, v_0 is the initial velocity of the electron and v_1 is the impact velocity of the electron. The nominal phase (α_n) can be found by letting v_1 equal the first cross-over point on the SEY curve. Even though electrons emitted at the nominal phase are perfectly synchronized for the resonant condition, electrons with a phase that is close to but not exactly equal to the nominal phase can also be part of the RF discharge through a process termed "phase-focusing".

Due to the spread of electron velocities and the time delay between impact and emission of a new electron, many electrons acquire a phase error with respect to the nominal phase. Important research conducted in the late 1950s was able to show that electrons within a certain range of the nominal phase eventually were able to converge to the nominal phase after successive gap traversals. This range of emission angles where the electron phase error gradually decreases until it converges to the nominal phase was termed "phase-focusing range". Outside of this range, the phase error grows with each transit and eventually the electron is lost due to an out-of-phase impact (i.e. they are above the "non-returning electron limit"), or they impact with insufficient energy. Inside the phase focusing range, the phase error gradually decreases with successive transits and the electron will converge towards the nominal phase. This implies that electrons in the RF discharge travel at or close to the nominal phase and as such are tightly bunched together forming an

"electron-cloud" as is seen in Fig. 2.1d. In later stages of multipaction, the electron-cloud works against electron growth, and eventually an equilibrium is reached (see section 2.1.5).

Assuming a zero initial velocity for emitted electrons, Henneburg, Orthuber and Steudel[16] calculated that 1st order multipactor could only occur if $0° \leq \alpha \leq 65°$ and that the phase-focusing occurred in the range $0° \leq \alpha \leq 32.5°$. Myers[17] and Greenblatt[18], also assuming a zero initial velocity, concluded the focusing range to be $0° \leq \alpha \leq 65°$. Although setting the initial emission velocity to zero allowed for a simplified analytical model, the phase ranges were found to be inadequate since in reality particles did have a non-zero initial velocity. A.Hatch[19] then studied the impact of non-zero initial velocities on the phase-focusing range and found that the range includes negative angles since electrons were energetic enough to overcome the force exerted by a retarding field and still arrive in-phase. Hatch's findings concluded ranges for first order multipactor to be $-90° \leq \alpha \leq 90°$ and higher orders ranges of $-90° \leq \alpha \leq -40°$.

It follows then that multipaction can only occur within a certain range: where the electrons are at nominal phase or within the phase-focusing region and the secondary yield is greater than one. These regions of breakdown are described in the next section.

2.1.4 Susceptibility Zones

Researchers have conducted numerous theoretical and experimental studies to chart the "multipactor zones"; input power boundaries that could initiate and sustain multipactor breakdown. These charts use frequency (f) gap (d) product ($f \times d$) to allow for scaling of the breakdown threshold for various gap sizes and frequencies. These susceptibility curves are used in the design of multipactor-free high-power RF devices. Through the years there have been a number of researchers who have developed curves both through analytical and experimental means. A few of them are discussed below.

Constant Velocity Chart

J.Sombrin[20] was one of the early researchers to publish the boundaries for different multipactor orders. Making the assumption that all electrons were emitted with a constant initial velocity between parallel plates, he showed that each multipactor order had its own susceptibility zone and these zones decreased in range as the order increased. However Hatch & Williams found this assumption to be quite unrealistic[19], (since secondary electrons individual velocity is statistically random) and they developed similar curves improving on the constant initial velocity approach. Figure 2.5 shows a typical multipactor chart using the constant velocity approach [20]. Note the tapering that occurs at higher $f \times d$ products in

each multipactor order where the effects of the constant velocity assumption are more apparent since the transit times are longer.

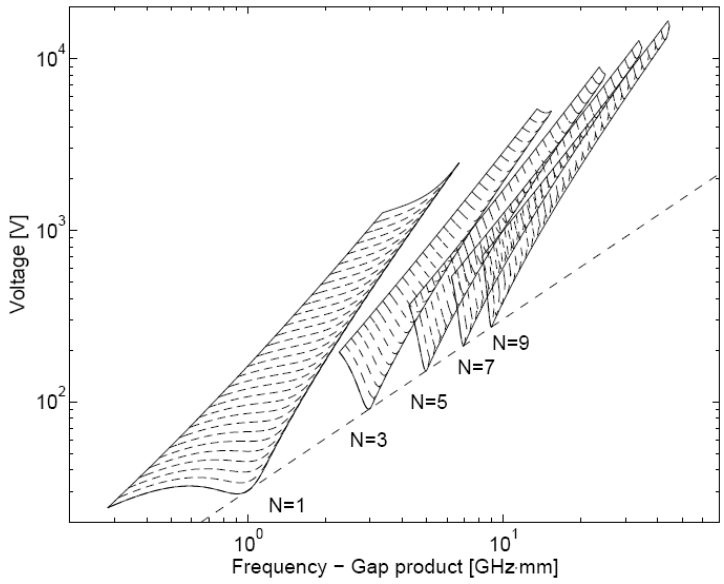

Figure 2.5: Multipactor Chart (Constant Velocity method) $W_o = 3.68eV, W_1 = 23eV, W_2 = 1000eV$ [20]

Hatch & Williams Chart

Claiming the constant initial velocity approach as unrealistic Hatch and Williams used a different approach to chart the multipactor susceptibility curves using a parallel plate model. Rather than keeping the initial velocity constant, Hatch and Williams[21] kept the ratio 'k' between the impact and initial velocities constant. The constant 'k' theory then forced a reformulation for the resonant phase condition (Eqn.2.4), the derivation of which can be found in [15].

$$\alpha = \arctan\left[\frac{1}{k-1}\left(\frac{k\omega d}{v_1} - (k+1)n\frac{\pi}{2}\right)\right] \tag{2.4}$$

Compared to the constant velocity charts in the above section, the Hatch & Williams charts showed multipactor zones of constant width, due in part to the constant ratio between the impact and initial velocity for each electron. As a result for a given multipactor order, higher $f \times d$ products result in a greater divergence between the two charts since the Sombrin zones taper off for high $f \times d$ products. Figure2.6 shows a typical Hatch & Williams multipaction chart for $k = 2.5$ [21]. However, both charts are in good agreement for lower f×d products in the same multipactor order.

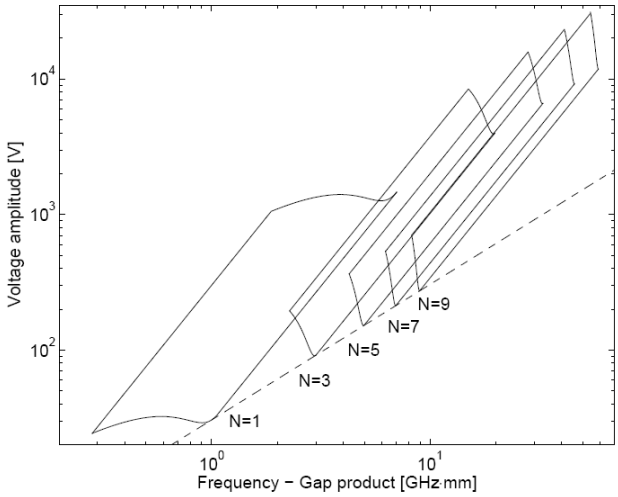

Figure 2.6: Hatch & Williams Multipactor Charts for k=2.5 [21]

Woode & Petit Charts

In the 1980s Woode & Petit [22] multipactor charts (parallel-plate model) were obtained through numerous experiments and used the Hatch & Williams charts to curve fit their data. In order to do this, parameters such as k and v_o had to be tuned for each multipactor order. Although unrealistic, this resulted in multipactor charts that agreed well with the experimental data. This procedure did not aid in the understanding of multipaction from a modelling perspective, nevertheless, it is useful from an engineering-design perspective. For this reason, The Woode & Petit Multipactor charts are the design-standard at the European Space Agency (ESA) and are very well accepted in the space industry [6]. The Woode & Petit chart for parameters specific to Aluminum [22] is shown in Figure 2.7 .

Woo Report

In 1970 R. Woo[23] released a report that has been widely used by engineers designing high-power RF devices due to the robust test and measurement procedures that were used to create the multipactor charts published in the report. As such over the years this report has been affectionately called the "Woo Report". Woo was able to conduct a good number of reliable experiments at NASA's Jet Propulsion Laboratory and created multipactor charts for coaxial transmission lines of different impedances and parallel electrodes. In subsequent experiments Woo considered the effects of outgassing and DC Electric Fields on multipaction, and was able to generate charts for these conditions as well. Figure 2.8 shows the multipactor chart for coaxial transmission lines, with and without outgassing for different impedances and gap sizes.

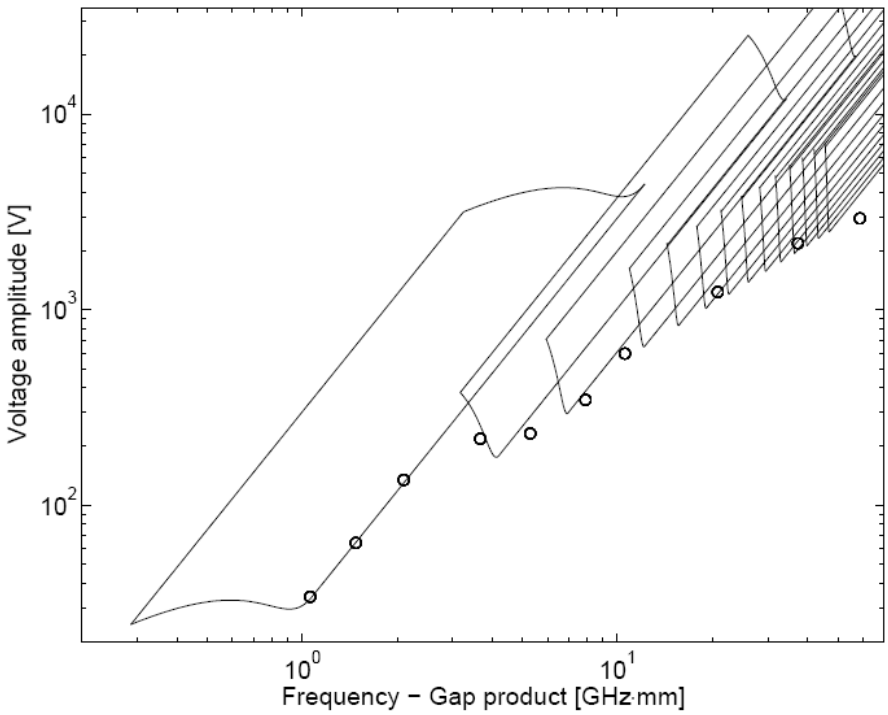

Figure 2.7: Woode and Petit Multipaction Charts for Aluminum[2]

2.1.5 Saturation

It is quite clear that the avalanche effect caused by microwave discharge cannot continue indefinitely, there has to be some physical phenomenon to slow this process down. In later stages of multipaction, the volume of the electron cloud grows along with a proportional growth in electron density (due to phase focusing). This creates a space charge effect (also known as electron cloud effect), whereby the forces of mutual repulsion act upon electrons in the cloud. This means that many electrons could be driven into the walls by their own field, and as a result impinge on the wall with very low energy, extracting zero secondaries. This mutual-replusion could eventually lead to an equilibrium state where SEY =1. If the electron cloud becomes very large, the mutual repulsion of the electrons will eventually be large enough to cause them to fall out of the resonance condition. Additionally, in the deep breakdown region, as the electron cloud grows exponentially, as electrons are multiplied by secondary emission at a wall, a positive charge could be left there, since more electrons leave the wall than impinge on it. This positive charge will perturb the secondary electron's motion as it leaves the wall, and the electron could fall out of resonance if the effect on its transit time is large. These effects could cause the behavior that has been observed empirically where by after a period of exponential grown in the electron population, in deep breakdown the rate of growth decelerates and eventually stabilizes to imply that as many electrons are being lost to the walls as are being added by impacting electrons.

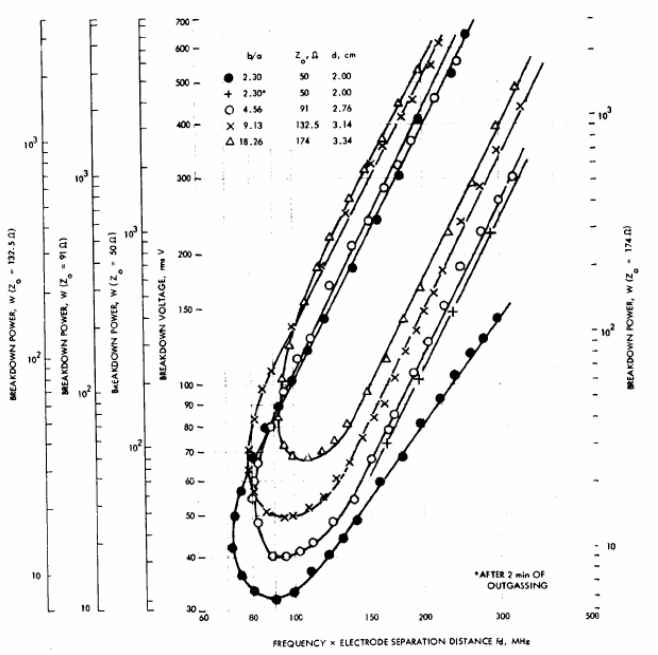

Figure 2.8: Woo Multipactor Chart for Coaxial Lines (various Z) [23]

2.1.6 Particle Trajectory

In order to successfully predict the onset of multipaction, the electron's path through the device must be calculated in order to record information about the impact, such as impact position, energy and time. This component of the model is the Electron Trajectory Module. In order to do this, the position of the electrons needs to be determined over time. The closed form solution to the problem of finding the spatial position of the electron can be found using the non-relativistic Lorentz force equation.

$$\vec{F} = q\left[\vec{E} + \vec{v} \times \vec{B}\right] \tag{2.5}$$

where F is the force in Newtons, E is the electric field in V/m, v is the instantaneous velocity in m/s, and B is the Magnetic Field in Tesla and q is the elementary particle charge in Coulombs. The non-relativistic Lorentz force is used here because it is reasonably certain that the electron will not be accelerated such that the velocity approaches that of light (highest speeds reached by the electrons are typically on the order of $10^7 m/s$).

From the Lorentz force equation it is clear that the particle will experience two forces, one due to the electric field ($q\vec{E}$) and the other due to the magnetic field (q·[$\vec{v} \times \vec{B}$]). This means that a positively charged particle will be accelerated in the same direction as the E field, but will bend normal to the magnetic field as dictated by the right hand rule. The Lorentz force forms the main equation that will be used to calculate the electron trajectory inside the device walls. In following chapters, this formula is used to find the equations of motion for parallel electrodes

and rectangular waveguides for the analytical model. Eventually, the equations of motion will be solved using differential equations and the Runge-Kutta 4th-5th Order method will be used as the numerical integrator, the details of which are presented in chapter 5.

Particle in Cell Method

Many multipactor models that solve the Lorentz force numerically use the particle in cell approach to calculate the electron trajectory under the influence of an EM field. The Particle in cell method, (PIC) utilizes a set of computational particles for representing the motion of particles such as electrons. for EM applications, PIC methods consist of the coupled solution of the equations of motion (Lorentz Force) and that of Maxwell equations on a spatial grid. PIC methods are used extensively in particle physics to model the interactions between particles and other materials. In multipactor modeling, PIC methods are used to calculate electron trajectories and also model particle interactions such as the space charge effect (i.e. the mutual repulsion between electrons) that is the reason the multipactor discharge saturates after a period of time. PIC methods typically use a mesh grid of known EM fields to calculate the field information at any point within the region using interpolation and smoothing techniques. For a more in-depth review of the PIC method, readers are referred to [24].

2.2 Current Multipactor Models

In this section, a review of multipaction models that are in development and have been recently published by researchers are detailed. It is important to note that not all published models that have been studied, but rather the models that are well understood and most relevant to this work will be outlined. Table 3.5 at the end of the chapter briefly summarizes the findings, and Table 3.6 lists other published models that are not detailed in this writing.

2.2.1 Full-wave EM Simulation Tool [FEST]

The Full-wave Electromagnetic Simulation Tool (FEST) was originally designed as EM simulator tool, but also has added the capability to perform multipactor modelling[25] in recent years. The model has been developed primarily at the European Space Agency, and first calculates the field distribution inside the microwave device before performing the multipactor simulation. The field calculation of the tool has been compared with Microwave studio[9] and has been found to be accurate and very fast. Although, FEST does have the capability to calculate the field distribution rectangular, circular and arbitrarily shaped waveguides composed of rectangular or circular waveguides, to the author's knowledge multipactor simulations can only be performed on structures simulated within FEST.

The reason for this is that although FEST was originally developed for waveguide design in space applications, the driving force behind the development of the tool was waveguide analysis using advanced techniques like boundary integral-resonant mode expansion[25]. The multipaction module was added later, and as such multipaction simulations can only be performed on selected geometries in FEST's library, to evaluate the field information. Simulations track each electron individually, including secondary electrons.

At each collision, important parameters such as impact energy, angle of incidence and impact location are recorded. Convergence of results in multipactor simulations in FEST are found to vary with the number of primary particles used in the simulation [26], even though secondary electrons are the main cause of breakdown. It was found that the number of primary particles to be launched depends on the geometry of the particular device [26] and its field distribution. FEST has the ability to simulate fringing fields such that if the ratio of gap height (y-axis) to gap width (x axis) is larger than one, more electrons tend to accelerate along curved paths (and may fall out of the high field region as a result) rather than straight line paths between walls. This behavior significantly increases the breakdown threshold since higher power is required to drive the secondary electrons across the gap and also because more electrons are driven outside the high field region [27]due to their long transit times. FEST can also simulate the space charge effect that is created during breakdown is the main cause of changes in microwave components after breakdown has occurred. Specifically, the fields created by the space charge propagate through the structure causing the incident power to be reflected and some other non-linear effects such as Passive Intermodulation (PIM) effects.

FEST can calculate the space charge effect by using a Particle in Cell model where the field created by space charges are interpolated to the mesh nodes and are added to the fields calculated by FEST. The total field is then used to apply the force of motion on the electrons. This ability to model the space charge effect has important implications on being able to correlate the simulation results with experimental parameters such as evaluating the change in scattering parameters before and after breakdown and evaluating the noise and harmonics generation of the device under test[28]. However, FEST can only predict breakdown for geometries in its library and convergence of simulation results is partly defined by the number of primary particles [26]. FEST also does not account for in-elastically reflected electrons and elastically reflected electrons.

FEST - Full-wave Electromagnetic Simulation Tool				
Research Organization	**Research Team**	**EM Solver**	**Numerical Solver**	**Algorithm**
University of Valencia, Spain European Space Agency, Netherlands	S. Anza, C. Vicente D. Raboso, V.E. Boria	FEST	Velocity Verlet	PIC, Maxwell Distribution
Strengths • Simulator accounts for complex Space Charge effects and Fringing Fields • Noise and Harmonics analysis				
Limitations • Simulator can only predict multipaction for structures found in FEST Library • Convergence depends on number of primary particles chosen • Does not account for backscattered and re-diffused electrons				

Table 3.1 - FEST Summary

2.2.2 TRAK_RF

Track_RF is a multipactor modeler developed collaboratively by Raytheon and The University of New Mexico, by lead researchers S. Humphries and N. Dionne. The model uses a conformal triangular mesh to discretize the regions of the structure as shown in Fig. 2.9. The conformal triangular mesh ensures that the sides of the elements are shifted so that vertices lie along material surfaces [29], the advantage of this form of mesh is that the edges of elements conform closely to curved and angled material boundaries, ensuring that each element is associated with a single material. This is important since it allows an accurate identification of surface collisions [30] if each element is represents only a single material. Trak_RF also has the ability to model three types of regions, 'vacuum' (region C in Fig. 2.9), 'secondary' (region B in Fig. 2.9)and 'material' (region A in Fig. 2.9). The model can associate different secondary emission and tracking properties to each material. For example, if an electron enters a 'material' element, it is absorbed and the electron orbit is terminated. However if it enters a 'secondary' element, the emission properties are calculated based on the impact parameters and the electron orbit is launched. Secondary electrons are created using a Maxwell distribution and the particle trajectory is calculated using field information provided by WaveSim or the TriComp code provided by Field Precision [30].

To simulate the particle trajectories, the code uses the macro-particle method where by the maximum number of particles in the simulation never increase. Each macro-particle is associated with a unique weighting and is launched as a seed electron. When marco-particles impact a surface, their weighting is multiplied by the secondary emission yield of that impact. At any point within the simulation, the weighting of a macro-particle represents the effective number of secondary electrons. In other words, a macro-particle simply represents all the secondary electrons it has created, only within a single particle. Therefore, each macro-particle represents a history that includes several generations of secondaries [29]. This method is used

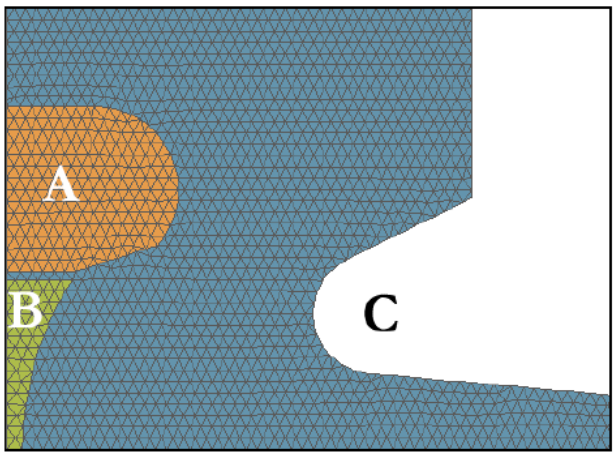

Figure 2.9: Conformal Mesh in TRAK_RF showing meshing of curves

for computational efficiency and is accurate in some geometries, however it cannot be universally applied. Its main limitation arises when the aspect ratio (ratio between length and height) of the geometry being studied is very large and particles escape from the gap. This case makes the method inaccurate since as time progresses many macro-particles will escape the gap which implies that all its effective secondary particles have also escaped the gap, and this might not be physically true. For example, if a macro-particle with a weighting of 1000 escapes the region, it implies that 1000 electrons have escaped the gap, which might not be true since the probabilistic nature of the secondary emission process makes it highly unlikely that two particles will follow the same trajectory. Therefore, this could result in a much higher predicted breakdown voltage than the empirical results will yield and can be readily observed with fringing fields. TRAK_RF has the ability to account for different regions within a simulation, such as secondary and material that model different SEY characteristics upon impact. However, TRAK_RF only simulates systems with two-dimensional symmetry where the geometry is represented by projections in either the xy plane [29] and uses macro-particle method to simulate multipaction to keep total number of particles constant.

TRAK_RF				
Research Organization	**Research Team**	**EM Solver**	**Numerical Solver**	**Algorithm**
University of New Mexico, USA Raytheon Corporation, USA	S. Humphries N. Dionne	WaveSim TriComp	Runge-Kutta	2D Mesh, Maxwell Distribution
Strengths • Simulator an account for different regions with very different SEY parameters **Limitations** • Simulates systems with 2D symmetry, simulations collapse 3D structure into 2D • Uses macro-particle method to simulate multipaction to keep total number of particles constant that may result in inaccurate results for large fringing fields				

Table 3.2 - TRAK _RF Summary

2.2.3 MEST - Multipactor Electron Simulation Tool

Multipactor Electron Simulation Tool (MEST) is a multipaction modeler for waveguide structures that was developed at the European Space Research and Technology Centre (ESTEC). The model tracks each electron individually, and flags an event every time a particle collides with the waveguide walls. The model also has the ability to account for advanced material properties that other similar models cannot such as the atomic number of the coating material. The model follows an "event scheduling" method where events are entered into the simulation queue chronologically. Events are created every time an electron impacts a wall, regardless of whether true secondaries are created. The SEY model used with MEST creates a random number of secondary electrons dictated by two probability distributions. The first, P_s is the probability that a collision produces true secondary electrons and the second P_n is the probability that this collision produces n electrons. P_n is generated by a Poisson probability distribution. An inverse cumulative probability function then assigns the energies to the newly created secondary electrons taking into account material properties and the principle of energy conservation. That is, the total energy assigned to the secondary electrons of an event cannot be greater than the energy of the impacting electron. Finally the cosine law distribution along with a uniform distribution [31] is used to calculate the launch direction for the secondary electrons. MEST's SEY model accounts for elastically backscattered electrons and in-elastically re-diffused electrons and it has extensive material modeling capabilities using 14 parameter model including atomic number[31], [7] of the coating material of the structure, but it can only simulate parallel plate structures and geometries with 2D modeling.

MEST – Multipactor Electron Simulation Tool				
Research Organization	**Research Team**	**EM Solver**	**Numerical Solver**	**Algorithm**
University of Madrid, Spain European Space Agency, Netherlands	F. Perez J. de Lara L. Galan D. Roboso	Analytical	Analytical	Monte Carlo, Poisson Distribution
Strengths • SEY Model accounts for backscattered electrons and re-diffused electrons • Extensive material modeling capabilities using 14 parameters including atomic number				
Limitations • Simulations can only be performed for simple geometries like parallel plate structures				

Table 3.3 - MEST Summary

2.2.4 MultP

Multp is a multipaction simulation tool developed at Institute of Nuclear Research in Russia and Moscow Engineering Physics Institute. The code allows for 2D and 3D simulations of RF cavities, coaxial and waveguide [32] structures. The EM field

information is imported from a specialized EM solver called Superfish [33] before the particle tracking and secondary emission models are run. Another unique ability of this tool is to allow users to run simulations looking for specific orders of multipaction. The code can operate in two different modes. In the first mode, the tool generates trajectories, tracks particles and records statistical data on the electron evolution. This is similar to the models described above. In the second mode, the user can set up launch parameters of the electrons and the model evaluates the particle trajectories to find parameter sets that generate resonant behavior. Using this mode, it is easier to pin point the particles that have "multipacting characteristics" much faster than traditional simulations. MultP does this by generating phase-field diagrams [34] that show the trajectories that are closest to resonance. MultP has two unique tools, the first is the ability to look for specific multipaction mode orders as defined by user and the second is to generates phase-field diagrams that help to identify potential particle trajectories that are close to resonance (and that can cause multipaction). Simulations have also been shown for different structures such as waveguides and coax and RF cavities. However, MultP does not account for high energy reflected particles such as backscattered and rediffused primary electrons [34], which has implications for the MultP's predicted multipactor breakdown level, as will be discussed in section 4.5.3.

MultP

Research Organization	Research Team	EM Solver	Numerical Solver	Algorithm
Institute for Nuclear Research, Russia Moscow Engineering Physics Institute, Russia	L. Kravchuk M.A. Gusarova S.G. Tarasov	MAFIA	Unpublished	PIC

Strengths

- Ability to look for specific multipaction mode orders as defined by user
- Generates phase-field diagrams to identify potential trajectories that are close to resonance

Limitations

- Does not account for high energy reflected primaries such as backscattered and rediffused primary electrons

Figure 2.10: Table 3.4 - MultP Summary

2.2.5 ESA Multipactor Calculator

ESA's Multipactor Calculator provides predictions of multipactor breakdown levels for different structures, for example, parallel plates and square axial transmission lines and also different surface materials such as silver and aluminum. ESA's curves are based on models developed by Woode & Petit (discussed in section 2.1.4). Since Woode & Petit curve fitted their charts to experimental data, they have been well-received in the space industry and are the design standard at the European Space

Agency [6]. However, the charts used by ESA are based on the uniform field approach, and as a result have been found to be conservative in its predictions for multipactor breakdown. In other words, ESA's curves typically underestimates the power handling capability of high power RF devices and is one of the reason why more accurate multipactor models for the space industry are being developed by researchers.

2.2.6 Sazontov Models

This multipactor model was developed by a team of researchers from Russia, Sweden and France. Sazontov et. al. [35] have produced multipactor charts for different materials, with an SEY_{max} range from 1.32 to 2.25 for a parallel plane geometry. The reason this work is included in this chapter is due to the robust method of their multipactor chart creation. Sazontov et. al. developed three different algorithms, a Particle-In-Cell (PIC), a Monte-Carlo and a Statistical algorithm each with their own strengths and limitations. The particle-in-cell code simulates realistic electron dynamics during breakdown, specifically the effects of the space charge or electron cloud effect. The ability to model the mutual repulsion between the electrons in the PIC code can aid in the investigation of nonlinear phenomena in multipactor discharges, such as harmonics generation. The Monte-Carlo approach aggregates calculations of numerous independent electron trajectories, and although it is fast, it does not account for the electron-cloud effect. Finally, the statistical code evaluates a probability distribution function that represents the arrival time of the electrons emitted with arbitrary velocities and phases. This probability distribution function can be calculated using the equations of motion of the particle and the boundary conditions of the geometry.

The three different procedures generated results in good agreement with each other, even though the approach used in each procedure was different. However even though Sazontov et. al. used a comprehensive method to model the probabilistic nature of the multipaction by using different algorithms (statistical, PIC and Monte-Carlo) the author notes that the secondary emission models used in each algorithm, was slightly different. In the case of the statistical and Monte-Carlo algorithms, only electrons which cross the gap can produce secondary electrons, however in the PIC model secondary electrons can be created by electrons that do not cross the gap [35].

Additionally, Sazontov's models use Vaughan's formulation for secondary emission, but does not consider high energy reflected particles [35]. As is explained in section 4.5.3, most multipactor models do not account for reflected high energy particles and the effects of this approach on the multipactor prediction levels are discussed in section 4.5.3.

2.2.7 Comparison of Models

Table 3.5 provides a comparison of the multipactor models presented in this thesis. For a brief description on other multipactor simulators in development please refer to the next section.

Software	FEST	TRAK_RF	MEST	MultP	Multipactor Calculator	Sazontov Models
Research Org.	University of Valencia, Spain European Space Agency, Netherlands	University of New Mexico, USA Raytheon Corp, USA	University of Madrid, Spain ESA, Netherlands	INR, Russia MEPI, Russia	European Space Agency & ESTEC	Academy of Sciences, Russia CNES, France Chalmers University, Sweden
Research Team	S. Anza, C. Vicente D. Raboso, V.E. Boria	S. Humphries N. Dionne	F. Perez J. de Lara L. Galan D. Roboso	L. Kravchuk M.A. Gusarova S.G. Tarasov	S.J.G. Strijk	A. Sazontov D. Anderson J. Puech M. Lisak
EM Solver	FEST	WaveSim TriComp	Analytical	MAFIA	N/A Empirical Charts	Analytical
Numerical Solver	Velocity Verlet	Runge-Kutta	Analytical	Unpublished	N/A	Analytical
Algorithm	PIC, Maxwell Distribution	2D Mesh, Maxwell Distribution	Monte Carlo, Poisson Distribution	PIC	Curve fitting to empirical data	PIC, Statistical, and Monte Carlo
Strengths	• Complex Space Charge analysis • Fringing Fields • Noise and Harmonics Analysis	• Regions with different SEY parameters	• Models backscattered and re-diffused primaries • Extensive material modeling capabilities	• User defined search for modes • Phase-field diagrams	• Charts for different surface materials • Charts for a few commonly used RF structures	• Robust and comprehensive algorithm with good agreement between results • Charts for different surface parameters
Limitation	• Structures in FEST library only • Convergence partially depends on # of seed particles • Backscattered & re-diffused primaries omitted	• Collapses 3D structure into 2D • Macro-particle Particle Tracking	• Simple geometries like parallel plate structures	• Backscattered & re-diffused primaries not considered	• Selected Geometries • Uses uniform EM field approximation	• Backscattered & re-diffused primaries not considered • Applicable to only selected geometries

Table 3.5 - Comparison of Multipactor Simulators

2.2.8 Other Simulators

Although there have been numerous tools developed by researchers that predict multipaction breakdown such as MultiPacting Simulation (MPS) and Multipactor Development Simulator (MDS) [36] only a few of the widely published and well understood models are presented in this writing. Readers are encouraged to refer to other multipaction tools mentioned in Table 3.6 to get a complete understanding of multipaction analysis in academic research.

Software	Research Organization	Research Team	EM / Numerical Solver
MutiPacting Simulation (MPS)	Budker INP, Russia	A. V. Grudiev D.G. Myakishev	SLANS / RK
Multipactor Development Simulation (MDS)	CNES, France Chalmers University, Sweden Institute of App. Physics, Russia	J. Peuch, D. Anderson, R. Udiljak M. Buyanova	Unpublished
Object-Oriented Particle in Cell Code (XOOPIC)	Institute of Physics, Serbia Vinca Institute of Nuclear Sciences, Serbia	M. Radmilovic B. Radjnovic	Analytical / Analytical
MultiPac	Rolf-Nevanlinna Inst., Finland DESY, Germany	P.Yla-Oijala D. Proch	Internal / Runge-Kutta-Fehlberg
MULTICOAX	Polytechnic University of Valencia, Spain University of Malaga, Spain	A. Perez C. Tienda C. Vicente et. al.	Analytical / RK4
MUPAC	CEA – Saclay , France	G. Devanz	SuperFish / RK

Table 3.6 - Additional Multipactor Simulators

Chapter 3

Analytical Particle Trajectory Tracker

Chapter Summary

This chapter details the analytical formulas derived to calculate the particle motion with in parallel plates and rectangular waveguides. In the waveguide analysis, both the electric field and magnetic field were considered in deriving the final equations of motion for electrons in large gap rectangular waveguides. The analytical model was used as a first step in this research to calibrate the secondary emission model. Once the secondary emission model was finalized, the numerical engine developed in Chapter 5 is used.

3.1 Analytical Formulation

As mentioned earlier, in order to successfully predict the onset of multipactor breakdown, the trajectory of the particles must be calculated in order to determine the impact parameters (such as impact position, energy and time) that dictate the secondary emission from the wall. This chapter presents the details of the first module of the multipaction prediction model: the particle trajectory tracker. Although the final version of the model solves the equations of motions numerically, the analytical particle tracker was developed first in order to calibrate the Secondary Electron Emission model(SEM). The analytical model was used to verify the SEM by comparing simulation results of the analytical model with current multipactor charts that use similar analytical models. The particle trajectories for geometries are presented (parallel-plate and rectangular waveguide) in this chapter, Chapter 5 presents the numerical engine (using Dormand-Prince RK45) that solves differential equations of motion (Lorentz Force equations)to calculate the motion of the particles.

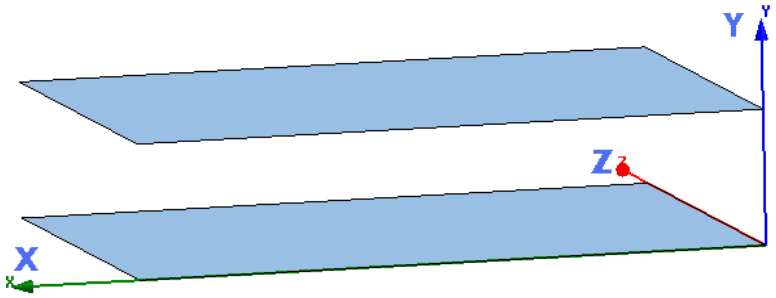

Figure 3.1: Coordinate System for Parallel Plate Setup

3.1.1 Parallel Electrodes

Many published works in multipactor analysis start with a parallel plate (PP) set-up since the EM field distribution and physics are well understood. As a result an infinite parallel-plate approach was also taken as an initial step for this research. Using the coordinate system in Fig.3.1 the electric field in a PP geometry is given by:

$$E_y = E_o \sin(\omega t) \tag{3.1}$$

Additionally the acceleration and force of a particle in the present of an EM field can be is given by Newton and Lorentz as:

$$\begin{aligned} \vec{a} &= \frac{\vec{F}}{m} \\ \vec{F} &= q\left[\vec{E} + \vec{v} \times \vec{B}\right] \end{aligned}$$

For the PP approach the magnetic field is not considered since only small gap sizes are considered in this analysis. Therefore the velocity in the y-direction can be expressed as :

$$v_y(t) = \int_{t_o}^{t} a_y \, dt \tag{3.2a}$$

$$= \frac{qE_o}{m} \int_{t_o}^{t} \sin(\omega t) \, dt \tag{3.2b}$$

$$= \frac{qE_o}{m\omega} \left[\cos(\omega t) - \cos(\omega t_o)\right] + C \tag{3.2c}$$

Setting $t = t_0$, in Eqn. 3.2c the constant becomes:

$$C = v_y(t = t_o) = v_{oy}$$

Therefore, the velocity of the particle in all three components can be expressed as:

$$[v_x(t), v_y(t), v_z(t)] = \left[v_{ox},\ \frac{qE_o}{m\omega}\left[\cos(\omega t) - \cos(\omega t_o)\right] + v_{oy},\ v_{oz} \right] \tag{3.3}$$

Since there is no electric field in the x&z direction, the velocity in those directions stay constant and is set by the initial conditions. The position of the particle at time t can then be expressed as:

$$\begin{aligned} s_y(t) &= \int_{t_o}^{t} v_y\ (t)\ dt \\ &= \frac{qE_o}{m\omega}\int_{t_o}^{t} \cos(\omega t)\ dt + \frac{qE_o}{m}\int_{t_o}^{t} \cos(\omega t_o)\ dt + \int_{t_o}^{t} v_{oy}\ dt \\ &= \frac{qE_o}{m\omega^2}\left[\sin(\omega t) - \sin(\omega t_o)\right] - \frac{qE_o}{m\omega}\cos(\omega t_o)\left[t - t_o\right] + v_{oy}\left[t - t_o\right] \\ &\quad + s_{oy} \end{aligned} \tag{3.4}$$

where $\vec{s_o} = [s_{ox}, s_{oy}, s_{oz}]$ is the position of the particle at $t = t_0$. Therefore the spatial position of the particle can be expressed as:

$$s_x = v_x[t - t_o] + s_{ox} \tag{3.5a}$$

$$\begin{aligned} s_y &= \frac{qE_o}{m\omega^2}\left[\sin(\omega t) - \sin(\omega t_o)\right] - \frac{qE_o}{m\omega}\cos(\omega t_o)\left[t - t_o\right] + v_{oy}\left[t - t_o\right] \\ &\quad + s_{oy} \end{aligned} \tag{3.5b}$$

$$s_z = v_z[t - t_o] + s_{oz} \tag{3.5c}$$

This completes the trajectory modelling for the PP. This analysis only considered the electric field, and not the magnetic field and is valid only for small gaps and low order multipactor. For a finite parallel plate where the gap is comparable with the plate size the magnetic field plays a larger role in higher order multipactor since the transit times are much longer and the magnetic field will change the electron trajectory. Since the PP approach was used as an initial calibration point, it was not deemed necessary to add the magnetic field formulation, but this is taken into account in the rectangular waveguide analysis.

3.1.2 Rectangular Waveguide

For a preliminary analysis, a rectangular waveguide as shown in Fig.3.2 with a small height "b" with respect to the width "a" is considered only with the electric field, thus the Lorentz force equation reduces to $\vec{F}$=q$\vec{E}$, due to small height of the waveguide. Additionally, only the forward based wave propagation is considered and only the TE_{10} mode is considered since it is the fundamental mode. Since no modulation is taken into account in this derivation, implying that this analysis is for single carrier systems only. Waveguides with large gaps will be discussed later in this chapter.

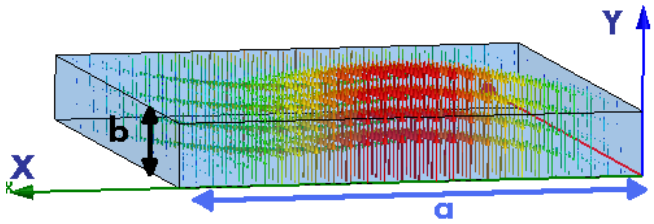

Figure 3.2: Coordinate system for Small Gap Rectangular Waveguide showing field vectors

Since the rectangular waveguide has no electric field in the x and z directions, the expected results should show the velocity in the x and z direction to be constant (specifically, the velocity in the x and z direction will be dictated by the initial velocity. set in the x and z direction) since for example:

$$\begin{aligned} v_x(t) &= \frac{q}{m}\int_{t_o}^{t} E_x \, dt \\ &= \frac{q}{m}\int_{t_o}^{t} 0 \, dt \\ &= C = v_{ox}(t_o) \end{aligned}$$

This implies that under the assumptions made above, the trajectory of the electron will only vary in the y direction. Specifically, the results are expected to show the velocity of the electron to oscillate in the y direction with time as shown in Fig. 3.3 . In other words, the results should show that the velocity in the y direction should be sinusoidal at the same frequency as the electromagnetic field.

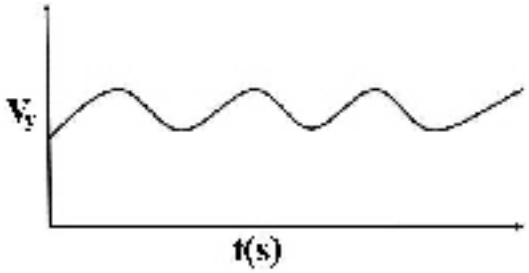

Figure 3.3: Expected velocity curve for rectangular waveguide

The electric field in the y-direction for the TE_{10} mode in a rectangular waveguide is shown below:

$$
\begin{aligned}
E_y(t) &= \frac{-j\omega\mu a}{\pi} A_{10} \sin\left(\frac{\pi x}{a}\right) e^{-j\beta z} e^{j\omega t} \\
&= E' \sin\left(\frac{\pi x}{a}\right) e^{-j\beta z} e^{j\omega t} \quad \text{where } E' = \frac{-j\omega\mu a}{\pi} A_{10} \quad \text{and} \quad A_{10} = \sqrt{\frac{4\pi^2 P_{10}}{\omega\mu a^3 b \,\mathrm{Re}(\beta)}} \\
&= E' \sin\left(\frac{\pi x}{a}\right) [\cos(\omega t - \beta z) - j \sin(\omega t - \beta z)] \qquad (3.6)
\end{aligned}
$$

where β is the propagation constant, P_{10} is the power flow down the rectangular waveguide for the TE_{10} mode, and A_{10} is the arbitrary amplitude constant as defined in Pozar[37]. Since the phase information of the field can be accounted for by advancing time, only the real part of $\vec{E}$ is considered, therefore:

$$
\begin{aligned}
v_y(t) &= \frac{qE'}{m} \sin\left(\frac{\pi x}{a}\right) \int_{t_o}^{t} E_y(t)\, dt \qquad (3.7) \\
&= \frac{qE'}{m} \sin\left(\frac{\pi x}{a}\right) \int_{t_o}^{t} [\sin(\omega t - \beta z)]\, dt \qquad (3.8)
\end{aligned}
$$

In Eqn. 3.8 although x and z are functions of time it is assumed for a very small Δt the change in position of the particle is negligible, and can therefore be omitted from the integration. In order to be consistent however, the time for each term is kept the same, and so the velocity can then be expressed as:

$$
v_y(t) = \frac{qE'}{m\omega} \sin\left(\frac{\pi x(t_o)}{a}\right) [\cos(\omega t_o - \beta z(t_o)) - \cos(\omega t - \beta z(t_o))] + C \qquad (3.9)
$$

The constant C can be calculated by imposing initial conditions for $\vec{v}_y(t)$, namely:

$$
\begin{aligned}
at\ time\ t,\ \ v_y(t &= t_o) = v_{oy} \\
\therefore\ \ C &= \vec{v}_{oy} \qquad (3.10)
\end{aligned}
$$

The velocity of the particle then becomes:

$$
\begin{aligned}
v_x(t) &= v_x(t = t_o) = v_{ox} \qquad (3.11) \\
v_y(t) &= \frac{qE'}{m\omega} \sin\left(\frac{\pi x(t_o)}{a}\right) \cos(\omega t_o - \beta z(t_o)) \qquad (3.12) \\
&\quad -\frac{qE'}{m\omega} \sin\left(\frac{\pi x(t_o)}{a}\right) \cos(\omega t - \beta z(t_o)) + v_{oy} \\
v_z(t) &= v_z(t = t_o) = v_{oz} \qquad (3.13)
\end{aligned}
$$

The spatial position of the particle can be calculated as:

$$
\begin{aligned}
s_y(t) &= \int_{t_o}^{t} v_y(t)\ dt && \text{(3.14a)}\\
&= \frac{qE^{'}}{m\omega}\int_{t_o}^{t}\sin\left(\frac{\pi x(t_o)}{a}\right)\cos(\omega t_o-\beta z(t_o))\ dt \\
&\quad -\frac{qE^{'}}{m\omega}\sin\left(\frac{\pi x(t_o)}{a}\right)\int_{t_o}^{t}\cos(\omega t-\beta z(t))\ dt+\int_{t_o}^{t} v_{oy}\ dt \\
&= \frac{qE^{'}}{m\omega}\sin\left(\frac{\pi x(t_o)}{a}\right)\cos(\omega t_o-\beta z(t_o))\ \int_{t_o}^{t} 1\ dt && \text{(3.14b)}\\
&\quad -\frac{qE^{'}}{m\omega}\sin\left(\frac{\pi x(t)}{a}\right)\int_{t_o}^{t}\cos(\omega t-\beta z(t))\ dt+\int_{t_o}^{t} v_{oy}\ dt \\
&= \frac{qE^{'}}{m\omega}\sin\left(\frac{\pi x(t_o)}{a}\right)[t-t_o]\cos(\omega t_o-\beta z(t_o)) \\
&\quad -\frac{qE^{'}}{m\omega^2}\sin\left(\frac{\pi x(t_o)}{a}\right)[\sin(\omega t-\beta z(t_o)-\sin(\omega t_o-\beta z(t_o)] \\
&\quad +v_{oy}\,[t-t_o]+C && \text{(3.14c)}
\end{aligned}
$$

In Eqn. 3.14b although the spatial position is time-dependent, in order to simplify the integration it is assumed that for small Δt the change in particle position is negligible along the x and z axis and is therefore treated as a constant versus time and removed from the integration.

The constant C can be calculated by imposing initial conditions, namely:

$$
\begin{aligned}
at\ time\ t_0,\ s_y(t &= t_o) = s_{oy} \\
&\therefore\ C = s_{oy} && \text{(3.15)}
\end{aligned}
$$

The spatial position of the particle then becomes:

$$
\begin{aligned}
s_x &= v_x[t-t_o]+s_{ox} && \text{(3.16a)}\\
s_y &= \frac{qE^{'}}{m\omega}\sin\left(\frac{\pi x(t_o)}{a}\right)[t-t_o]\cos(\omega t_o-\beta z(t_o)) \\
&\quad -\frac{qE^{'}}{m\omega^2}\sin\left(\frac{\pi x(t)}{a}\right)[\sin(\omega t-\beta z(t)-\sin(\omega t_o-\beta z(t_o)] \\
&\quad +v_{oy}\,[t-t_o]+s_{oy} && \text{(3.16b)}\\
s_z &= v_z[t-t_o]+s_{oz} && \text{(3.16c)}
\end{aligned}
$$

As stated earlier the formulation above does not consider the magnetic field. In order to complete the model for the rectangular waveguide, the particle trajectory

due to the influence of the magnetic field must be considered. Therefore, we must consider the Lorentz force once again:

$$\vec{F}_{mag} = q\left[\vec{v} \times \vec{B}\right] \tag{3.17}$$

the force in each component becomes:

$$\vec{F}_{mag} = q\left[(v_y B_z - v_z B_y)\ \hat{\imath},\ (v_z B_x - v_x B_z)\ \hat{\jmath},\ (v_x B_y - v_y B_x)\ \hat{k}\right] \tag{3.18}$$

Since the B field in the y-direction is zero, Eqn. 3.18 reduces to:

$$\vec{F}_{mag} = q\left[(v_y B_z)\ \hat{\imath},\ (v_z B_x - v_x B_z)\ \hat{\jmath},\ (-v_y B_x)\ \hat{k}\right] \tag{3.19}$$

Assuming that the force of the magnetic field on the particle in the y-direction is negligible when compared to that of the $\vec{E}$ field, it is implied that the motion of the particle in the y-direction only depends on the $\vec{E}$ field. So:

$$\vec{F}_{mag} = q\left[(v_y B_z)\ \hat{\imath},\ 0,\ (-v_y B_x)\ \hat{k}\right] \tag{3.20}$$

In order to arrive at the final formulation that considers the magnetic field, expressions for B_z and B_x must first be derived. Since the phase of the EM Field can be changed by advancing time, the phase information of the field is not required, and the equation can simplified by only taking the real part (amplitude) of the field:

$$\begin{aligned} B_z &= \mu H_z \\ &= \mathrm{Re}\left(\mu A_{10} \cos\left(\frac{\pi x}{a}\right) e^{j(\omega t - \beta z)}\right) \qquad (3.21) \\ &= \mu A_{10} \cos\left(\frac{\pi x}{a}\right) \cos(\omega t - \beta z) \qquad (3.22) \end{aligned}$$

Similarly for B_x,

$$\begin{aligned} B_x &= \mu H_x \\ &= \frac{\mu j \beta a}{\pi} A_{10} \sin\left(\frac{\pi x}{a}\right) e^{j(\omega t - \beta z)} \\ &= \mathrm{Re}\left(\frac{\mu j \beta a}{\pi} A_{10} \sin\left(\frac{\pi x}{a}\right) \left[\cos(\omega t - \beta z) - j \sin(\omega t - \beta z)\right]\right) \\ &= \frac{\mu \beta a}{\pi} A_{10} \sin\left(\frac{\pi x}{a}\right) \sin(\omega t - \beta z) \qquad (3.23) \end{aligned}$$

Therefore, the equations of motion in the x-direction (due to the magnetic field) can be derived as:

$$\begin{aligned} F_x &= q(v \times B) = q(v_y B_z) \\ &= q v_y (\mu A_{10} \cos\left(\frac{\pi x}{a}\right) \cos(\omega t - \beta z)) \qquad (3.24) \end{aligned}$$

The force can be related to the velocity using Newton's law, through:

$$a_x(t) = \frac{F_x}{m} = q\mu A_{10} \cos\left(\frac{\pi x}{a}\right) [v_y \cos(\omega t - \beta z)] \tag{3.25}$$

The velocity then becomes:

$$v_x(t) = \frac{q\mu A_{10}}{m} \cos\left(\frac{\pi x}{a}\right) \int_{t_o}^{t} [v_y \cos(\omega t - \beta z)] \; dt \tag{3.26}$$

Since, in the y-direction the electric field is much greater than the magnetic field, the motion of the particle will be primarily driven by the electric field, and the magnetic field will have a negligible effect (Eqn. 3.20), therefore Eqn. 3.12 can be used as:

$$v_{y_{\vec{E}}}(t) = \frac{qE'}{m\omega} \sin\left(\frac{\pi x(t_o)}{a}\right) \cos(\omega t_o - \beta z(t_o)) - \frac{qE'}{m\omega} \sin\left(\frac{\pi x(t_o)}{a}\right) \cos(\omega t - \beta z(t_o)) + \vec{v}_{oy_{\vec{E}}} \tag{3.27}$$

The motion in the x-direction can then be derived by substituting Eqn. 3.27 into Eqn. 3.26. Once again in order to simply the analysis, the position along the z direction although time dependent is treated as independent of time for very small Δt, in essence keeping the position constant for small time increments. The velocity can be expressed as:

$$\begin{aligned}
v_x(t) &= F_1 \int_{t_o}^{t} \cos(\omega t - \beta z(t)) \; dt - F_2 \int_{t_o}^{t} \cos^2(\omega t - \beta z(t)) \; dt \\
&\quad + F_3 \int_{t_o}^{t} \cos(\omega t - \beta z(t)) \; dt \qquad (3.28) \\
where \;\; F_1 &= \frac{q^2 \mu^2 a A_{10}^2}{m^2 \pi} \sin\left(\frac{\pi x(t_o)}{a}\right) \cos(\omega t_o - \beta z(t_o)) \cos\left(\frac{\pi x(t_o)}{a}\right) \\
F_2 &= \frac{q^2 \mu^2 a A_{10}^2}{m^2 \pi} \sin\left(\frac{\pi x(t)}{a}\right) \cos\left(\frac{\pi x(t_o)}{a}\right) \\
F_3 &= \frac{q\mu A_{10}}{m} \cos\left(\frac{\pi x(t_o)}{a}\right) v_{y_{\vec{E}}}(t_o)
\end{aligned}$$

After the integration a few simplification are made and the final velocity in the x direction can be calculated as:

$$\begin{aligned}
v_x(t) &= \frac{F_1}{\omega} [\sin(\omega t - \beta z(t)) - \sin(\omega t_o - \beta z(t_o))] \\
&\quad - \frac{F_2}{4\omega} \left[\sin(2(\omega t - \beta z(t))) + \frac{t 4\omega}{2} - \sin(2(\omega t_o - \beta z(t_o))) - \frac{t_o 4\omega}{2}\right] \\
&\quad + \frac{F_3}{\omega} [\sin(\omega t - \beta z(t)) - \sin(\omega t_o - \beta z(t_o))] + v_{ox}(t) \qquad (3.29)
\end{aligned}$$

A similar procedure is used to derive the x-position of the particle due, as:

$$
\begin{aligned}
s_x(t) &= \int_{t_o}^{t} \vec{v}_x(t)\ dt \\
&= \frac{F_1}{\omega}\int_{t_o}^{t} \sin(\omega t - \beta z(t))\ dt - \frac{F_1}{\omega}\sin(\omega t_o - \beta z(t_o)\int_{t_o}^{t} 1\ dt \\
&\quad -\frac{F_2}{4\omega}\int_{t_o}^{t} \sin(2\left(\omega t - \beta z(t)\right))\ dt + \frac{F_2}{2}\int_{t_o}^{t} t\ dt \\
&\quad -\frac{F_2}{4\omega}\sin(2\left(\omega t_o - \beta z(t_o)\right))\int_{t_o}^{t} 1\ dt \\
&\quad -\frac{F_2}{2}t_o\int_{t_o}^{t} 1\ dt + \frac{F_3}{\omega}\int_{t_o}^{t} \sin(\omega t - \beta z(t))\ dt \\
&\quad -\frac{F_3}{\omega}\sin(\omega t_o - \beta z(t_o))\int_{t_o}^{t} 1\ dt + \vec{v}_{ox}(t)\int_{t_o}^{t} 1\ dt \qquad (3.30) \\
&= \frac{F_1}{\omega^2}\left[\cos(\omega t_o - \beta z(t_o)) - \cos(\omega t - \beta z(t)) - \omega\sin(\omega t_o - \beta z(t_o))\left[t - t_o\right]\right] \\
&\quad -\frac{F_2}{8\omega^2}\left[\begin{array}{c}\cos(2\left(\omega t_o - \beta z(t_o)\right)) - \cos(2\left(\omega t - \beta z(t)\right)) \\ -2\cos(2\left(\omega t_o - \beta z(t_o)\right))\left[t - t_o\right]\end{array}\right] \\
&\quad -\frac{F_2}{4}\left(t^2 - t_o^2 - 2t_o(t - t_o)\right) + \frac{F_3}{\omega^2}\left[\begin{array}{c}\cos(\omega t_o - \beta z(t_o)) - \cos(\omega t - \beta z(t)) \\ -\omega\sin(\omega t_o - \beta z(t_o))\left[t - t_o\right]\end{array}\right] \\
&\quad +\vec{v}_{ox}(t)\left[t - t_o\right] + \vec{s}_{ox}(t) \qquad (3.31)
\end{aligned}
$$

A similar process for the z-coordinate is also presented briefly, the force in the z-direction due to the magnetic field is:

$$
\begin{aligned}
\vec{F}_z &= q(-\vec{v}_y\vec{B}_x) \\
&= -q\vec{v}_y(\mu\frac{\beta a}{\pi}A_{10}\sin\left(\frac{\pi x}{a}\right)\sin(\omega t - \beta z)) \qquad (3.32)
\end{aligned}
$$

The force can be related to the velocity using Newton‘s law, through:

$$
a_z(t) = \frac{F_z}{m} = \frac{-q\mu\beta a A_{10}}{m\pi}\sin\left(\frac{\pi x}{a}\right)\left[v_y \cdot \sin(\omega t - \beta z)\right] \qquad (3.33)
$$

The velocity then becomes:

$$
v_z(t) = -\frac{q\mu\beta a}{m\pi}A_{10}\sin\left(\frac{\pi x}{a}\right)\int_{t_o}^{t}\left[v_y \cdot \sin(\omega t - \beta z)\right]\ dt \qquad (3.34)
$$

As stated earlier in the y-direction the electric field is much greater than the magnetic field, the motion of the particle will be primarily driven by the electric field, and the magnetic field will have a negligible effect (Eqn. 3.20), and Eqn. 3.12 can be used. The motion in the z-direction can then be derived by substituting

Eqn. 3.27 into Eqn. 3.34. Once again in order to simply the analysis, the position although time dependent is treated as independent of time for very small Δt along the z direction, in essence keeping the position constant for small time increments. The velocity can then be expressed as:

$$\begin{aligned} v_z(t) &= G_1 \int_{t_o}^{t} \sin(\omega t - \beta z(t_o))\ dt \\ &\quad -G_2 \int_{t_o}^{t} \cos(\omega t - \beta z(t)) \sin(\omega t - \beta z(t))\ dt \\ &\quad +G_3 \int_{t_o}^{t} \sin(\omega t - \beta z(t_o))\ dt \end{aligned} \tag{3.35}$$

$$\begin{aligned} where\ \ G_1 &= \frac{-q^2\mu^2a^2\beta A_{10}^2}{m^2\pi^2} \sin\left(\frac{\pi x(t_o)}{a}\right) \cos(\omega t_o - \beta z(t_o)) \sin\left(\frac{\pi x(t_o)}{a}\right) \\ G_2 &= \frac{q^2\mu^2a^2\beta A_{10}^2}{m^2\pi^2} \sin^2\left(\frac{\pi x(t_o)}{a}\right) \\ G_3 &= \frac{-q\mu\beta a A_{10}}{m} \sin\left(\frac{\pi x(t_o)}{a}\right) v_{y_{\vec{E}}}(t_o) \end{aligned}$$

After the integration a few simplification are made and the final velocity in the x direction can be calculated as:

$$\begin{aligned} v_z(t) &= \frac{G_1}{\omega} \left[\cos(\omega t_o - \beta z(t_o)) - \cos(\omega t - \beta z(t))\right] \\ &\quad -\frac{G_2}{2\omega} \left[\sin^2(\omega t - \beta z(t)) - \sin^2(\omega t_o - \beta z(t_o))\right] \\ &\quad +\frac{G_3}{\omega} \left[\cos(\omega t_o - \beta z(t_o)) - \cos(\omega t - \beta z(t))\right] + v_{oz}(t) \end{aligned} \tag{3.36}$$

A similar procedure is used to derive the z-position of the particle due, shown below:

$$\begin{aligned} s_z(t) &= \int_{t_o}^{t} v_z(t)\ dt \\ &= \frac{G_1}{\omega} \cos(\omega t_o - \beta z(t_o)) \left[t - t_o\right] - \sin(\omega t - \beta z(t_o)) - \sin(\omega t_o - \beta z(t_o)) \\ &\quad +\frac{G_2}{8\omega^2} \left[\sin(2\left(\omega t - \beta z(t_o)\right)) - \sin(2\left(\omega t_o - \beta z(t_o)\right)) - 4\omega \sin^2(\omega t_o - \beta z(t_o)) \left[t - t_o\right]\right] \\ &\quad +\frac{G_2}{4\omega} \left[t - t_o\right] + \frac{G_3}{\omega} \left[\cos(\omega t_o - \beta z(t_o)) \left[t - t_o\right]\right] + v_{oz}(t) \left[t - t_o\right] + s_{oz}(t) \end{aligned} \tag{3.37}$$

The final analytical equations for the particle velocity in the RWG can be described as:

$$
\begin{aligned}
v_x(t) &= \frac{F_1}{\omega}\left[\sin(\omega t-\beta z(t_o))-\sin(\omega t_o-\beta z(t_o))\right] \qquad (3.38)\\
&\quad -\frac{F_2}{4\omega}\left[\sin(2\left(\omega t-\beta z(t)\right))+\frac{t4\omega}{2}-\sin(2\left(\omega t_o-\beta z(t_o)\right))-\frac{t_o4\omega}{2}\right]\\
&\quad +\frac{F_3}{\omega}\left[\sin(\omega t-\beta z(t_o))-\sin(\omega t_o-\beta z(t_o))\right]+v_{ox}(t)\\
v_y(t) &= \frac{-qj\omega\mu a}{\pi m}A_{10}\sin\left(\frac{\pi x(t_o)}{a}\right)\cos(\omega t_o-\beta z(t_o))\\
&\quad -\frac{qE'}{m}\sin\left(\frac{\pi x(t)}{a}\right)\cos(\omega t-\beta z(t))+v_{oy} \qquad (3.39)\\
v_z(t) &= \frac{G_1}{\omega}\left[\cos(\omega t_o-\beta z(t_o))-\cos(\omega t-\beta z(t))\right]\\
&\quad -\frac{G_2}{2\omega}\left[\sin^2(\omega t-\beta z(t))-\sin^2(\omega t_o-\beta z(t_o))\right]\\
&\quad +\frac{G_3}{\omega}\left[\cos(\omega t_o-\beta z(t_o))-\cos(\omega t-\beta z(t))\right]+v_{oz}(t) \qquad (3.40)
\end{aligned}
$$

where F and G are given in Eqn. 3.28 and Eqn. 3.35 respectively.

The final analytical equations for the particle position in the RWG can be described as:

$$
\begin{aligned}
s_x(t) &= \frac{G_1}{\omega}\cos(\omega t_o-\beta z(t_o))\left[t-t_o\right]-\sin(\omega t-\beta z(t_o))-\sin(\omega t_o-\beta z(t_o))\\
&\quad +\frac{G_2}{8\omega^2}\begin{bmatrix}\sin(2\left(\omega t-\beta z(t_o)\right))-\sin(2\left(\omega t_o-\beta z(t_o)\right))\\ -4\omega\sin^2(\omega t_o-\beta z(t_o))\left[t-t_o\right]\end{bmatrix}\\
&\quad +\frac{G_2}{4\omega}\left[t-t_o\right]+\frac{G_3}{\omega}\left[\cos(\omega t_o-\beta z(t_o))\left[t-t_o\right]\right]+v_{oz}(t)\left[t-t_o\right]+s_{oz}(t) \qquad (3.41)\\
s_y(t) &= \frac{qE'}{m}\sin\left(\frac{\pi x(t_o)}{a}\right)\left[t-t_o\right]\cos(\omega t_o-\beta z(t_o))\\
&\quad -\frac{qE'}{m\omega}\sin\left(\frac{\pi x(t_o)}{a}\right)\left[\sin(\omega t-\beta z(t_o)-\sin(\omega t_o-\beta z(t_o)\right]\\
&\quad +v_{oy}\left[t-t_o\right]+s_{oy} \qquad (3.42)\\
s_z(t) &= \frac{G_1}{\omega}\cos(\omega t_o-\beta z(t_o))\left[t-t_o\right]-\sin(\omega t-\beta z(t))-\sin(\omega t_o-\beta z(t_o))\\
&\quad +\frac{G_2}{8\omega^2}\left[\sin(2\left(\omega t-\beta z(t)\right))-\sin(2\left(\omega t_o-\beta z(t_o)\right))-4\omega\sin^2(\omega t_o-\beta z(t_o))\left[t-t_o\right]\right]\\
&\quad +\frac{G_2}{4\omega}\left[t-t_o\right]+\frac{G_3}{\omega}\left[\cos(\omega t_o-\beta z(t_o))\left[t-t_o\right]\right]+v_{oz}(t)\left[t-t_o\right]+s_{oz}(t) \qquad (3.43)
\end{aligned}
$$

where F and G are given in Eqn. 3.28 and Eqn. 3.35 respectively.

The analytical equations derived in this chapter were used to develop and calibrate the finalized secondary emission model that is presented in the next chapter. The analytical equations of motion were derived for the different structures as a first step before numerical techniques were used, in order to minimize the complexity in

the model. Using this approach, the emission model could be tested using a variety of distribution functions and advanced techniques without having to consider the effects of numerical interpolation or integration, on the breakdown results. Once the secondary emission model was finalized, the numerical engine was developed. to study the outcomes of results

The breakdown level results for low and high order multipaction in rectangular waveguides using the analytical approach in presented in Chapter 6 along with the rest of the simulation results from this research work.

Chapter 4

Secondary Emission Model

Chapter Summary

This chapter details the Secondary Emission Model (SEM) in the context of the generalized multipactor modeling approach that is taken in this research.

Since a generalized approach to multipactor modelling was taken in this research, the SEM developed in this research is a much more accurate representation of the physical process of secondary emission when compared to other models. This is because other models make simplifying assumptions in the development of geometry specific multipactor models.

This higher accuracy allows the model developed in this research to be highly efficient since far fewer seed particles are required for convergence when compared to other models. This is verified by the fact that the model developed in this research typically requires around 50 seed particles for simulation results to converge whereas other models published in recent years require between 500 and thousands of seed particles in order to converge to reasonable results.

Secondly due to the generalized approach taken in this research, the model presented here could potentially be used to predict multipactor breakdown in complex geometries when used with commercial EM solvers (CEM).

This chapter presents some of the treatment of basic secondary emission parameters used in all multipactor models such as the secondary emission yield (SEY) and emission direction vectors. However, this chapter also discusses some of the more advanced concepts that have been considered in this research such as inelastic and elastic primary electrons, emission of out-of-phase high energy electrons, individual tracking of electrons and energy distribution functions.

4.1 Secondary Emission Yield

This section focuses on the secondary emission yield (SEY) formulae that are an important part of the emission process. As mentioned earlier in section 2.1.1, this work uses the Vaughan formulation for the SEY. SEY formulae were empirically developed many years before Vaughan's research, and though the results they provide are not as accurate as Vaughan's formulae, they are nevertheless still used as cruder approximations[16]. One of the reasons Vaughan's formulation is more accurate is because in the 25+ years since Lye & Dekker, and Bruining & Muller published their formulae, the accuracy of the equipment and measurement systems have increased dramatically, along with a greater understanding of the subject in the scientific community. Since these formulae have been empirically derived, more accurate measurements and data translates into a more accurate formulation.

A typical SEY curve is shown in Fig. 4.1, where V_1 and V_2 are called the first and second crossover points where the SEY (δ) is exactly one. At these points no multipaction can occur since there can be no electron population growth. However multipaction can occur between the crossover points, since the SEY is greater than one. $V_{\max}$ is the impact voltage at which the maximum SEY ($\delta_{\max}$) has been measured and V_o is the impact voltage at under which the SEY converges to zero.

Formulas developed by Bruining and Muller [38] in 1948 expressed SEY for oblique directions in terms of the orthogonal SEY calculated for the same impact voltage. However, these formulae didn't take into account two observed trends. The first trend being the independence of a directional effect at low voltages (typically less than V_1) and the second being the increase of V_{max} and $\delta_{\max}$ as the angle of impact increases [16]. Both these trends are observed in Fig. 4.1, which shows the effect on the SEY with an oblique angle of impact of 60°.Note all impact angles are measured with respect to the surface normal. When an electron impacts the surface at a 60° impact angle the SEY increases because electrons do not penetrate as deep into the surface when compared to a 0° impact. Since electrons with higher-angle impacts typically stay closer to the surface, they have the ability to release more secondary electrons, since these electrons are closer to the surface. As the impact angle approaches zero (i.e. impacts angles are orthogonal to the surface), the electrons are driven deeper into the surface releasing fewer secondary electrons.

In order to reflect the angle of impact trend, a correction factor was later added to the V_{max} and δ_{max} formulae as:

$$V_{\max\theta} = V_{\max 0}\left(1+\frac{k_s\theta^2}{\pi}\right) \tag{4.1}$$

$$\delta_{\max\theta} = \delta_{\max 0}\left(1+\frac{k_s\theta^2}{2\pi}\right) \tag{4.2}$$

where V_{max} and δ_{max} are shown in Figure. 4.1 and k_s is a smoothness factor for the surface, ranging from 0 for rough surfaces to 2 for polished crystalline surface.

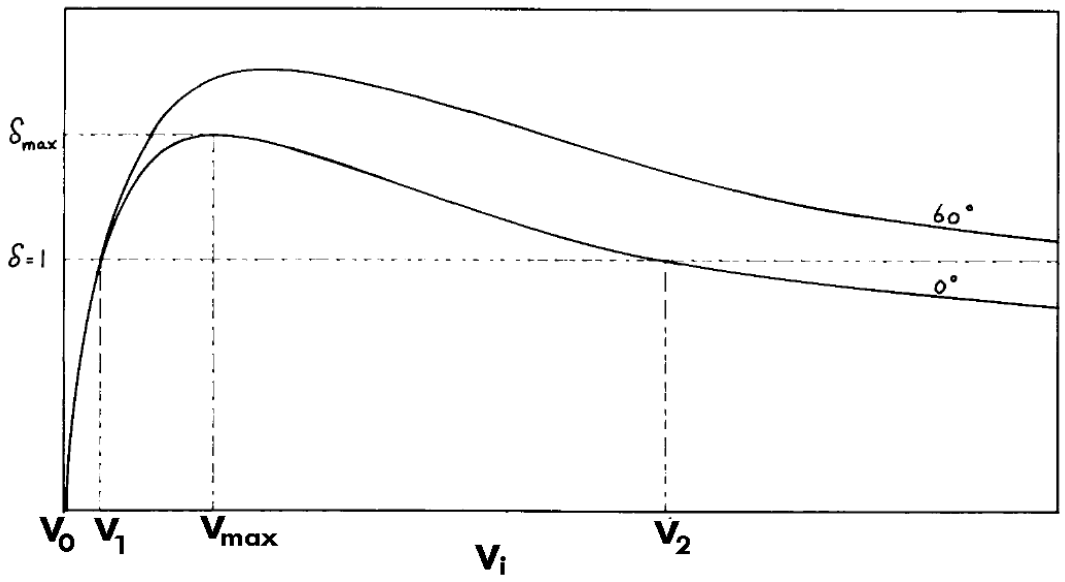

Figure 4.1: Typical SEY curve for 0° incidence and 60°

In absence of data that would suggest otherwise, a typical dull surface would be assigned a $k_s = 1$. V_{max0} is the impact voltage at which the SEY is the greatest for an orthogonal (0 degree relative to the normal) impact.

In 1957, Lye and Dekker [39] published an important empirical formulation that employed the Muller and Bruining formulae. After conducting and collecting experimental data, Lye and Dekker published breakthrough formulae to predict the SEY as a function of the impact voltage V_i, to a reasonable degree of accuracy. With a slight change in notation, the empirical formulae published are:

$$\begin{aligned} \frac{\delta}{\delta_{\max}} &= \frac{1}{g_n(z_m)} \cdot g_n\left(z_m \frac{V_i}{V_{\max}}\right) \\ where\ g_n(z) &= \frac{1 - e^{-z^{n+1}}}{z^n} \end{aligned} \tag{4.3}$$

Here, z_m is the value of z at which $g_n(z)$ is a maximum; n is an adjustable parameter where the authors adopted 0.35 to fit empirical data. However, for higher voltage impacts they suggested a higher n. Using the suggested value of $n = 0.35$, a simple variable sweep shows that $g_n(z) = 0.725$ for a $z_m = 1.84$ as shown in Fig. 4.2. This reduces the Lye and Dekker formulae to:

$$\frac{\delta}{\delta_{\max}} = 1.379 \frac{1 - e^{-\left(\frac{1.844 V_i}{V_{\max}}\right)^{1.35}}}{\left(\frac{1.844 V_i}{V_{\max}}\right)^{0.35}} \tag{4.4}$$

This formula can be reduced even further by noting that as V_i increases past V_{max} the exponential term approaches zero and becomes negligible. Therefore in the high-voltage region (above around $V_i = 3V_{max}$) , the exponential term can be ignored

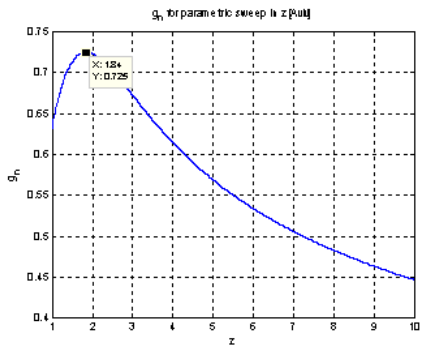

Figure 4.2: Typical Bruining curve for g_n as z is swept, to find z_m

and the numerator is approaches unty, and the formula can be further simplified to:

$$\frac{\delta}{\delta_{\max}} = 1.113\left(\frac{V_i}{V_{\max}}\right)^{-0.35} \qquad valid \text{ only for } \mathrm{V_i} > 3\mathrm{V_{max}} \tag{4.5}$$

The formula above was one of the early secondary emission formulas that were used by researchers in secondary emission modeling. Recently, a more accurate was presented by Vaughan, and is discussed in detail since it is the main SEY formulation that is used in this research.

4.1.1 Vaughan Formulation

Due to advances in measurement equipment and a better understanding of the underlying physics that causes multipaction, in 1989 Vaughan was able to publish formulae that he empirically developed with a better approximation in the low voltage region (compared to the Gibbons curve [40]) than the Lye and Dekker formula. The Gibbons curve, widely recognized in the area as the "universal curve shape" is the general characteristic that researchers agree is a good representation of the SEY for most surfaces under any angle of incidence. Even though no formula for the curve was given, the curve proved to be quite accurate as numerous test results were collected and normalized to their respective V_{max} and δ_{max}). A similar curve is shown in Fig. 4.1.

The low-voltage-region formula proposed by Vaughan in 1989, developed empirically with a curve fitting methodology is:

$$\frac{\delta}{\delta_{\max}} = \left(ve^{1-v}\right)^k \quad \text{where } v = \frac{V_i - V_o}{V_{\max} - V_o} \tag{4.6}$$

Here, V_{max} is defined in Fig. 4.1 and by Bruining and Muller's formula, and V_o is the impact voltage at which an SEY greater than zero starts to occur. He found this value to be $12.5V$ experimentally. k is a curve fit parameter where:

$$k = k_1 = 0.62 \quad \text{for v} < 1 \tag{4.7}$$

$$k = k_1 = 0.25 \quad \text{for v} > 1 \tag{4.8}$$

Using the values of k above, the Vaughan formula approximates the Gibbons curve well, and was found to be a better fit to the curve than the Lye and Dekker formula (in the low voltage region $Vi \leq 3V_{max}$). Note even though a discontinuity in k exists when $v = 1$, this is not a concern because the value of k is inconsequential when v approaches 1 in the Vaughan formulation. However, the discontinuity can be smoothed out by:

$$k = \frac{k_1 + k_2}{2} - \frac{k_1 - k_2}{\pi} \arctan(\pi \ln v) \tag{4.9}$$

$k_{1,2}$ can be determined from accurate measurements of V_1 and V_2 by:

$$\begin{aligned} k_{1,2} &= \frac{\ln \delta_{\max}}{v_{1,2} - \ln v_{1,2} - 1} \\ where \;\; v_{1,2} &= \frac{V_{1,2} - V_o}{V_{\max} - V_o} \end{aligned} \tag{4.10}$$

The procedure for finding $V_{1,2}$ if $k_{1,2}$ are given is a more involved, but is not documented here since it is not relevant to the this research.

High Voltage Region ($\mathbf{V}_i \geq \mathbf{3V}_{max}$)

The empirical formula developed by Vaughan is a better approximation of the Gibbons curve in the low voltage region only. As such, in the high voltage region it is better to return to the Lye and Dekker formula. This is because in this region Vaughan's formulation will decrease as $exp(-v)$.

The two formulae can be found to intersect (to a reasonable degree of accuracy) at:

Once again the discontinuity that occurs in δ at v_3 can be smoothed out by:

$$v_3 = \frac{1}{k_2} - 0.25. \tag{4.11}$$

Therefore, for most analysis the Vaughan formula provides more accurate results when v less than v_3 and the Lye and Dekker formula provides greater accuracy when v is greater than v_3.

Once again the discontinuity that occurs in δ at v_3 can be smoothed out by:

$$k = \frac{\delta_1 + \delta_2}{2} - \frac{\delta_1 - \delta_2}{\pi} \arctan\left(\pi \ln \frac{v}{v_3}\right) \tag{4.12}$$

This equation simply asymptotes to k_1 on the left and to k_2 on the right, with a smooth transition centered at $v = 1$.

4.1.2 Modification of Vaughan formulation:

In 1993, four years after Vaughan published his formulation, Shih and Hor [41] conducted SEE experiments using molybdenum and platinum ribbons welded onto tungsten mounting rods. The motivation for their research was the fact that previous research considered numerous materials but mostly at normal angles of incidence. Even some of the available data were collected prior to the 1960's when modern surface analytical instruments were not available. Therefore the cleanliness of the sample surface was not accounted for when doing measurements. Since the surface conditions of the material (such as surface contaminants and surface roughness) affect the SEY, Shih and Hor were able to collect more accurate data by accounting for these surface conditions by using modern measurement systems. In addition, to study how the SEY depends on the angle of incidence, a flat and smooth surface is critical, so that the angle of incidence can be accurately defined.

Once the experimental data was obtained, Shih and Hor fit their results with Vaughan's formulation. They found that even though Vaughan's formulation was a good approximation of the data, some minor modifications to the formulation had to be made.

A brief summary of the 3 criticisms they made of Vaughan's formulation are:

1. Vaughan's formulation stated that the smoothness factor (for $v \leq 1$), k_1 was constant at 0.62. Although Shih and Hor also found k_1 to be independent of θ, the best fit to the data occurred with $k_1 = 0.557 \pm 0.027$.Vaughan's prediction of 0.62 was higher than this value.

2. Conversely, Shih and Hor agreed with Vaughan's predicted value of k_2 however their test results found that k_2 has a dependence on θ, implying that k_2 is not constant as suggested by Vaughan.

3. Shih and Hor also found very different smoothness values for δ_{max} and V_{max}, when trying to fit the expressions to their data. Vaughan's formulation used the same k_s for both relations. However, they found the k_s for δ_{max} to be 1.96 ± 0.11 and 0.93 ± 0.14 for V_{max}.

4.1.3 Modified Vaughan Formulation

In light of the new accurate data collected by Shih and Hor, Vaughan [16] made some modifications to the formulation in 1993, stating that the formulation was derived from previous data that did not have the kind of surface purity attained by Shih and Hor. Vaughan reduced the value for k_1 for $v < 1$, modified the smoothness factor k_s to be distinct for V_{max} and δ_{max}, and changed the V_{max} relation to θ, by a factor of 2.

To increase the accuracy of Vaughan's formulation, the revised formulation is (modifications are in bold):

$$V_{\max\theta} = V_{\max 0}\left(1+\frac{\mathbf{k_{sV}}\theta^2}{\mathbf{2}\pi}\right) \tag{4.13}$$

$$\delta_{\max\theta} = \delta_{\max 0}\left(1+\frac{\mathbf{k_{s\theta}}\theta^2}{2\pi}\right) \tag{4.14}$$

where k_{sv} and $k_{s\theta}$ are separate smoothness factors for V and δ respectively. Both should be assigned a value of unity, which is appropriate for dull surfaces. Lower values should be used for rough surfaces down to zero for textured carbon, and higher values upto 2 for extremely smooth, clean, oxide-fee surfaces.

Then:

$$\frac{\delta(\theta)}{\delta_{\max}(\theta)} = \left(ve^{1-v}\right)^k \quad \text{where } v = \frac{V_i - V_o}{V_{\max} - V_o} \tag{4.15}$$

and:

$$\begin{aligned} k &= k_1 = \mathbf{0.56} \ \text{ for v} < 1 \\ k &= k_1 = 0.25 \ \text{ for } \mathbf{1 < v \leq 3.6} \end{aligned}$$

where V_o is the impact voltage at which the SEY is > 0, and taken to be $12.5V$, V_i is the impact voltage of the primary particle, and θ is the direction of impact relative to the normal in radians. Changes that were made to Vaughan's original formulation are in bold typeface.

In the high voltage region, for $v > 3.6$, the simplified Lye and Dekker formula provides better results in simulation codes as the expression doesn't "blow up", thus:

$$\frac{\delta(\theta)}{\delta_{\max}(\theta)} = \frac{1.125}{v^{0.35}} \quad \text{for} \quad \text{v} > 3.6 \tag{4.16}$$

Since the behavior of the electrons are always described in terms of its energy (in electronvolts), to maintain this convention the above formulation is slightly modified for the simulator.

Since 1eV is simply 1 volt (1 joule per coulomb) times the (unsigned) value of 1 elementary charge then the Vaughan formulation can be converted to electronvolts. The final formulation for the secondary emission coefficient then becomes :

$$\begin{aligned} v &= \frac{V_i - V_o}{V_{\max} - V_o} \cdot \left(\frac{1e}{1e}\right) \\ &= \frac{E_i - E_o}{E_{\max} - E_o} \end{aligned} \tag{4.17}$$

where E_i is the impact energy of the particle and E_o is the energy at which SEY is > 0. Additionally:

$$\frac{\delta(\theta)}{\delta_{\max}(\theta)} = \left(ve^{1-v}\right)^k \quad \text{for v } \leq 3.6 \tag{4.18}$$

$$\frac{\delta(\theta)}{\delta_{\max}(\theta)} = \frac{1.125}{v^{0.35}} \quad \text{for v } \geq 3.6 \tag{4.19}$$

where k takes the value of:

$$k = k_1 = 0.56 \quad \text{for v} < 1 \tag{4.20}$$

$$k = k_1 = 0.25 \quad \text{for } 1 < \text{v} \leq 3.6 \tag{4.21}$$

The maximum values required to calculate the SEY is calculated as:

$$E_{\max}(\theta) = E_{\max}(\theta)\left(1 + \frac{k_{sE}\theta^2}{2\pi}\right) \tag{4.22}$$

$$\delta_{\max}(\theta) = \delta_{\max}(\theta)\left(1 + \frac{k_{s\theta}\theta^2}{2\pi}\right) \tag{4.23}$$

Although Vaughan's formulation can provide the number of electrons that are emitted (given certain impact parameters), the results of the formulation are not integer numbers and therefore must be discretized since the number of emitted electrons in an impact event must be integer. In order to do this each impact event was discretized using a random uniform distribution.

Although Vaughan's formulation is generally well-accepted in the research community and used in numerous multipactor models for predicting the number of true secondary particles in the multipactor discharge. However the consideration of high energy reflected primary electrons is missing. Since the intent of this research is to develop an efficient and generalized procedure to model the multipaction phenomenon, this SEM model accounts for reflected primary particles in order to represent the secondary emission process more accurately than most other multipactor algorithms.

Since the accuracy of the secondary emission model is critical in determining multipactor breakdown levels, the generalized approach taken in this research ensures that this model is able to represent the physical emission process as closely as possible, unlike other models that make simplifying assumptions. Since most other models do not take this approach, they are not as vigorous as the model developed in this research and require far more seed particles to accurately predict breakdown levels in different structures. This is discussed further in section 4.6.

4.2 Incident Impact Angle Calculation

As described earlier, the secondary electron yield is heavily dependent on the incident angle of impact. Therefore, at every collision event, the impact angle (with

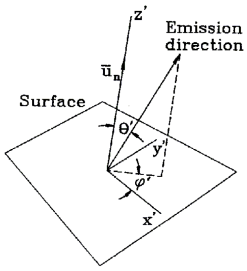

Figure 4.3: Cosine Law Distribution

respected to the surface normal at the point of impact) must be calculated. Since this research only considers metallic plated structures (most common satellite communication equipment is typically designed with a metal surface), the multipaction region will be between metal surfaces and the normal to the surface will always be in the direction of the electric field with a 180° shift in direction. In other words, the electric field is forced to be orthogonal to the metal surface by the boundary condition. Therefore the incident impact angle can be calculated as the angle between the electric field at the point of impact and the particle impact velocity as follows. The unit vector in the direction of the electric field at the point of impact is:

$$\vec{u}_{n_E} = \frac{\vec{E}}{|\vec{E}|} = \frac{1}{\sqrt{E_x^2 + E_y^2 + E_z^2}} \left[E_x \hat{\imath} + E_y \hat{\jmath} + E_z \hat{k} \right] \tag{4.24}$$

and the unit vector in the direction of the impact is:

$$\vec{u}_{n_s} = \frac{\vec{v}}{|\vec{v}|} = \frac{1}{\sqrt{v_x^2 + v_y^2 + v_z^2}} \left[v_x \hat{\imath} + v_y \hat{\jmath} + v_z \hat{k} \right] \tag{4.25}$$

therefore the angle of impact can be calculated as:

$$\theta = \arccos \left[\frac{v_x E_x + v_y E_y + v_z E_z}{\sqrt{E_x^2 + E_y^2 + E_z^2}\sqrt{v_x^2 + v_y^2 + v_z^2}} \right] \tag{4.26}$$

4.3 Emission Direction

The formulation presented earlier, evidences the fact that the SEY is highly dependent on the angle of impact, however empirical data suggests that the emission direction of the secondary electrons is largely independent of the impact angle[13], [8]. For this work, a variant of the cosine law distribution is used [30], as shown in the figure below, where θ' is the elevation angle with respect to the surface normal and φ' is the azimuth angle from the x-coordinate. In following sections, this coordinate set-up shown in the figure below will be called the **local coordinate system**. In order to preserve the statistical variance inherent in the emission process a normal probability distribution function is used to generate two random values between 0

and 1 that will be used to calculate the emission direction. The emission direction will be calculated as:

$$\begin{aligned} \theta^{'} &= 2\pi\xi_1 && (4.27) \\ \varphi^{'} &= \arcsin(\xi_1) && (4.28) \\ \text{where } 0 &\leq \xi_1, \xi_1 \leq 1 \end{aligned}$$

A transformation is used to convert the emission direction to Cartesian coordinates as :

$$\begin{aligned} ed_x &= \sin\theta^{'}\cos\varphi^{'} && (4.29) \\ ed_y &= \sin\theta^{'}\sin\varphi^{'} && (4.30) \\ ed_z &= \cos\theta^{'} && (4.31) \end{aligned}$$

where $[ed_x\hat{\imath}, ed_y\hat{\jmath},\ ed_z\hat{k}]$ is the emission direction of the secondary electron.

As shown in the diagram above, the local coordinate system that is used to calculate the emission direction always considers the surface normal to be the z' axis, i.e. the normal is always $u_n = (0, 0, 1)$. The emission direction is then computed with respect to this surface normal. However, the normal in the global coordinate system can be arbitrarily directed since for complex geometries the surface normal can be defined in any direction. A transformation is then used to create a mapping the local normal to the global normal. In so doing, the emission direction defined locally automatically is transformed into the emission direction in the global system. This is explained in the next section.

Mapping Between Local Normal and Global Normal

As shown in 4.3, the system used to calculate the emission direction of the secondary particle assumes a normal in the z direction. The surface normal in the local system (Fig. 3.0) is always considered to be the z axis, but the surface normal in the global system is defined according to the surface at the point of impact. Therefore a transformation matrix must be generated to map from one normal to the other. This matrix, is then used to transform the "local emission direction" to "the global emission direction" i.e. the matrix is used to define the emission direction with respect to the global normal, instead of the local normal.

Although different methods can be used to perform 3D mappings and rotations such as Quaternion, Direction Cosine Matrix and various other matrices, this work uses a matrix used in 3D graphics applications due to its speed and efficiency.

The transformation matrix that creates a mapping from one vector to another, namely from the global normal ($\hat{g}$) to local normal ($\hat{l}$), can be computed using the unit vector, $\vec{u}$:

$$\begin{aligned} \hat{u} &= \frac{g \times l}{|g \times l|} && (4.32) \\ \theta &= \arccos(\hat{g} \cdot \hat{l}) && (4.33) \end{aligned}$$

Rotating around the unit vector $\vec{u}$, by θ, the rotation matrix can then be defined by [42]:

$$T(g,l) = \begin{bmatrix} u_x^2 + (1-u_x^2)\cos\theta & u_x u_y(1-\cos\theta) + y_z \sin\theta & u_x u_z + u_y \sin\theta \\ u_x u_y(1-\cos\theta) + u_z \sin\theta & u_y^2 + (1-u_y^2)\cos\theta & u_y u_z(1-\cos\theta) + u_x \sin\theta \\ u_x u_z(1-\cos\theta) + u_y \sin\theta & u_y u_z(1-\cos\theta) + u_x \sin\theta & u_z^2 + (1-u_z^2)\cos\theta \end{bmatrix} \tag{4.34}$$

The above matrix is tremendously computationally intensive, thus if we let:

$$\hat{v} = \hat{g} \times \hat{l} \tag{4.35}$$

$$\hat{c} = \hat{g} \cdot \hat{l} \tag{4.36}$$

$$h = \frac{1-c}{1-c^2} = \frac{1-c}{v \cdot v} \tag{4.37}$$

Then the above transformation matrix can be simplified to:

$$T(g,l) = \begin{bmatrix} c + hv_x^2 & hv_x v_y - v_z & hv_x v_z + v_y \\ hv_x v_y + v_z & c + hv_y^2 & hv_y v_z + v_x \\ hv_x v_z - v_y & hv_y v_z + v_x & c + hv_z^2 \end{bmatrix} \tag{4.38}$$

This matrix now provides a mapping from the local normal to the global normal. In order to map from the local to the global, the inverse of the T matrix must be computed. Notice that the simplified T matrix does not have any square roots or trigonometric functions and is therefore less computationally intensive. The emission direction, which was defined with respect to the local surface normal, can now be defined with respect to the global surface normal.

Switching Between Local and Global Reference Systems

Establishing a mapping from the local normal to the global normal requires the simulator to switch coordinate systems, since the global normal needs to be imported into the local coordinate system. In this work, the global coordinate system (GCS) is defined as the coordinate system that the EM simulator uses to analyze the RF structure. The local coordinate system (LCS) on the other hand, is the system used to calculate the particle emission direction upon each impact. The two coordinate systems are separate and distinct due to the orientations of their respective axis, and as such, one must convert between the two systems appropriately in order to launch the secondary particles in the correct direction. Any computation that requires both a global vector and local vector, must first switch reference frames so that both vectors are defined in the same coordinate system before the computation takes place.

The LCS is static, in that the emission direction is always calculated using the same axis orientation. However, the global system is free to have its axis orientations defined by the user, and therefore is not static.

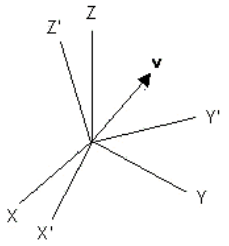

Figure 4.4: Switching between GCS (XYZ) to LCS (X′Y′Z′)

A transformation matrix must be used to convert vectors from the GCS to LCS and vice versa. For example, in Fig. 4.4, the reference has been shifted from the XYZ reference frame to the $X\prime Y\prime Z\prime$ reference frame. Although this example involves a simple rotation, the standard matrix below can generate the mapping between any two coordinate systems.

This transformation does not alter v, but rather how v is described, i.e. the Cartesian components of the vector.If we let $\hat{\imath}, \hat{\jmath}, \hat{k}$ represent the unit vectors for the XYZ system, and let $\hat{\imath}', \hat{\jmath}', \hat{k}'$ to represent the unit vectors for the $X'Y'Z'$ system, then:

$$v_x^{'} = \vec{v} \cdot \hat{\imath}' = v_x \hat{\imath} \cdot \hat{\imath}' + v_y \hat{\jmath} \cdot \hat{\imath}' + v_z \hat{k} \cdot \hat{\imath}' \tag{4.39}$$

$$v_y^{'} = \vec{v} \cdot \hat{\jmath}' = v_x \hat{\imath} \cdot \hat{\jmath}' + v_y \hat{\jmath} \cdot \hat{\jmath}' + v_z \hat{k} \cdot \hat{\jmath}' \tag{4.40}$$

$$v_z^{'} = \vec{v} \cdot \hat{k}' = v_x \hat{\imath} \cdot \hat{k}' + v_y \hat{\jmath} \cdot \hat{k}' + v_z \hat{k} \cdot \hat{k}' \tag{4.41}$$

This can be represented in matrix form as:

$$T_{G/L} = \begin{bmatrix} \hat{\imath} \cdot \hat{\imath}' & \hat{\jmath} \cdot \hat{\imath}' & \hat{k} \cdot \hat{\imath}' \\ \hat{\imath} \cdot \hat{\jmath}' & \hat{\jmath} \cdot \hat{\jmath}' & \hat{k} \cdot \hat{\jmath}' \\ \hat{\imath} \cdot \hat{k}' & \hat{\jmath} \cdot \hat{k}' & \hat{k} \cdot \hat{k}' \end{bmatrix} \tag{4.42}$$

Therefore the transformation matrix that converts from the global reference frame to the local reference frame can be written as:

$$\begin{bmatrix} v_x^{'} \\ v_y^{'} \\ v_z \end{bmatrix} = T_{G/L} \begin{bmatrix} v_x \\ v_y \\ v_z \end{bmatrix} \tag{4.43}$$

Similarly, to map the local reference frame to the global reference frame, the inverse of the T matrix is generated:

$$T_{L/G} = \left[T_{G/L}\right]^{-1} = \left[T_{G/L}\right]^{t} \tag{4.44}$$

Therefore, as mentioned in the previous section, in order to obtain the emission direction of the secondary particle, the global normal is imported into the LCS as defined earlier. Before doing this however, the global normal has its reference

frame switched using the matrix above, so that it can be used in the LCS. Using this methodology, the secondary electron emission direction for any arbitrary surface in 3D can be found.

4.4 Trajectory Termination

Unless trajectories of particles that have a low probability to trigger multipaction are not terminated, the model would not be able to analyze all particles as the multipactor discharge grows. Note that the multipactor discharge typically grows at an exponential rate and therefore, a proper definition of the trajectory termination condition is required. However, this model ensures that all termination conditions are reflected in the physical process, and are not 'simplifying assumptions'. Conditions under which particle tracking is terminated are:

1. As per the requirements of the SEY formulae if the kinetic energy of the electrons impacting the surface is below cutoff value E_o, particles are not tracked. This condition stops the simulator from tracking extremely low-energy impacting electrons as they will not have enough energy to generate secondary electrons and participate in the multipactor discharge.

2. As per the requirements of the SEY formulae if the kinetic energy of the electrons impacting the surface is above a cutoff value E_{max}. This condition stops the simulator from tracking extremely high-energy impacting electrons as they probabilistically can penetrate through the material at high velocities and not generate any secondary emission. This termination condition usually sets the upper bound of the multipaction susceptibility curves discussed in Chapter 2.

3. Trajectories that have been tracked for more than the maximum number of RF cycles. The maximum number of RF cycles is set according to the accuracy required in the breakdown results. This condition ensures that the model does not track a single particle trajectory for an undetermined period of time.

Although, these conditions state the parameters that control the termination criteria, no numerical values are stated as these parameters can be changed in the model depending on the rigidity of the required accuracy and computation time.

4.5 Advanced Concepts in Secondary Emission

The SEM in this research was developed to be as close to the physical emission process as possible. Therefore a vigorous approach was used in order to include

advanced concepts of secondary electron emission so that the SEM developed in this research is more accurate and more efficient that other multipactor models in development. This section outlines the points of distinction between this research work and other similar works. The strengths of the model developed in this research is that it is highly efficient since far fewer seed particles are required for convergence of multipactor breakdown levels when compared to other models. This is verified by the fact that the model developed in this research typically requires around 50 seed particles for breakdown prediction results to converge whereas other models published in recent years require between 500 and thousands of seed particles in order to converge to reasonable results.

Secondly due to the generalized approach taken in this research, the model presented here could potentially be used to predict multipactor breakdown in complex geometries when used with commercial EM solvers (CEM).

This section presents some of the more advanced concepts that have been considered in this research such as inelastic and elastic primary electrons, emission of out-of-phase high energy electrons, individual tracking of electrons and energy distribution functions of secondary electrons.

4.5.1 Out of Phase Secondary Emission

As discussed in section 2.1.2, the basic theory of multipactor breakdown is that in order for particles to participate in the multipactor discharge, they must impact the wall in an integer number of half RF cycles. This translates into the requirement that only particles that impact the wall in the accelerating phase (or in-phase duration) of the RF field are taken into account.

Almost all other multipactor models [5],[29],[26],[14],[35] do not emit secondary electrons when impacts occur in the decelerating (or out-of-phase) phase of the RF field. This is a simplifying assumption made in most other multipactor models since the models are used for select geometries and therefore a generalized approach is not required in the development of the model. This can be shown in the case of parallel plane [7], coaxial lines [5], and rectangular waveguides [9]. Additionally, this assumption greatly reduces the number of particles that need to be tracked, making this approach very attractive for computational reasons.

However, since this research uses a generalized approach, this assumption was not made. This is a major point of difference between the model developed in this research and most other multipaction models. While it is true that impacts during the retarding phase of the RF field cannot participate in the multipaction discharge since they are out of phase in terms of the resonance requirement (i.e. the impact occurred in an even half cycle of the RF field rather than the required odd half cycle for the multipactor resonance condition), statistically some secondary particles could have enough energy to escape the surface and remain in the vacuum for a period of time until the RF field switches to a favorable phase.

In other words some high energy particles could still be emitted from the surface during an even half cycle, and if the RF field switches phase fast enough, the particle could survive in the vacuum before being accelerated to the opposite wall and releasing more particles. This process was considered in the secondary emission model since it has been empirically found that high energy particles have a larger phase-range than low energy electrons [43], and can travel further through a retarding RF field. Accounting for the high energy particles in this manner has been shown to result in lower breakdown levels in some cases. In other words, the model developed in this research would predict a multipactor discharge where under normal techniques multipactor breakdown is predicted not to occur.

Most other multipactor simulators drop particles created during out of phase impacts since they do not meet the resonance condition, however the author believes that the process stated previously is closer to the physical behavior of the electrons during multipaction. The electron dynamics, phase of the RF field and statistical variations employed within this model are then allowed to determine if these 'out of phase' particles can take part in the multipactor discharge.

Since particles are emitted regardless of phase, there are quite a few low energy particles that are emitted during the 'out of phase' impact. These particles do not affect the breakdown level since soon after emission they are forced to return to the surface by the RF field and as a result they impact the surface with extremely low energy (i.e. energy levels lower than V_o in Fig. 4.1). Therefore do not create any secondary electrons and in effect, they are terminated upon their next impact. As such they have no affect on the breakdown level since their low energy impacts ensure that no additional electrons are emitted.

4.5.2 Emission Energy

Once the emission direction of the electron is calculated, launch energies must be assigned to each secondary electron. There are numerous ways to assign these energies, previous works have defined various energy spectrums [44], [13], Maxwell distribution [26], or different probability functions [45]. Many SEM also use a Gaussian distribution with a distribution of a few eV width. It is important to note however that some of the multipactor models that use these distributions do not account for the energy of the primary electrons [46] and [5]. In other words, some models emit secondary electrons based on distribution functions that do not account for the impact energy of the primary electron. Assuming there are no super-elastic collisions, it is extremely rare for secondary electrons to be emitted with more energy than the impacting primary. While models that do not account for the primary energy when calculating secondary emission launch energies never violate the principle of conservation of energy, these models could assign energies that are inconsistent with the impact energy. For example, in the case of a primary electron impacting at 100eV, there is a chance that the true secondaries released from this impact could be around 10-15 eV. However in models where distributions do not

consider primary energies such as [46] and [5], the energy assigned to secondaries will be around 5eV. Therefore, it is important for the emission energy of true secondary electrons be coupled to the primary energy and that the principle of conservation of energy is met.

In the model developed in this research, an e$\not$cient probability distribution function was used to couple the energy of the primary particle upon impact to the secondary electrons that are released upon impact. The exact details of assigning the secondary electron emission energy along with other important details of this work, with will be published at a later date.

4.5.3 Reflected Primary Particles

As discussed in section 2.1.1 reflected primary electrons are categorized as either inelastically reflected (re-diffused primary electrons) or elastically reflected (backscattered primary electrons). These high energy electrons along with the true secondary electrons make up the total secondary yield. Empirical measurements of the secondary emission energy spectrum typically look like Fig. 4.5, which shows the secondary energy spectrum results for a copper surface bombarded with electrons with 200eV of energy. Although the curve is for copper, the curve has almost the same shape for any metal surface. It is clear from this figure that although most low energy electrons are true secondaries, some higher energy electrons (rediffused (RE in Fig. 4.5) or backscattered (EE in Fig. 4.5) electrons) are also emitted. Therefore reflected primary electrons make a noticeable contribution in the overall secondary emission phenomenon, and this contribution is not reflected in Vaughan's formulation. By extension, most multipactor models that use Vaughan's formulae also do not take the effects of high energy reflected electrons into account.

Although Vaughan's formulation provides accurate results for the SEY, it is not able to account for the reflected primary portion of the SEY. This is because Vaughan's formulation is in essence an integration of the energy distribution function of the emitted electrons over a sweep of impacting electron energies. In other words, electrons with a specific energy were bombarded onto a surface and the energy distribution of the emitted electrons were then recorded. This energy distribution function probably had a similar shape as the curve in Fig. 4.5. This curve was then integrated to find the total SEY for a specific impact energy. Therefore information about energy distributions and probability of reflected primaries and secondary electrons are combined into the formula, in a way that access to this important information is lost. In other words, Vaughan's formulation presumes that all electrons emitted from a surface are released with very low energies and therefore primary reflection is not taken into consideration [43].

Unlike other multipactor models in development [8],[30],[26] this research accounts for backscattered and rediffused primaries since it is closer to the physical emission process and also because it has been shown that reflected primaries have a noticeable effect on the predicted breakdown level in certain scenarios. In other

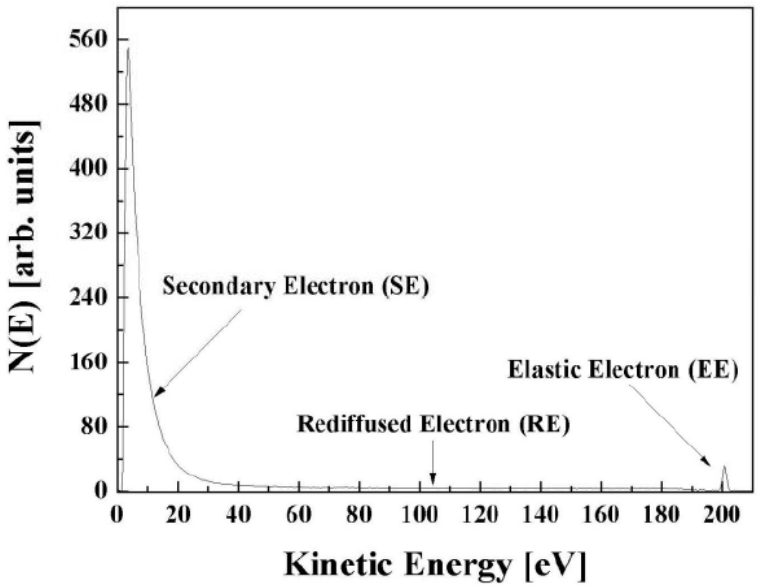

Figure 4.5: Energy distribution curve for Copper surface [3]

words, including the reflected primary electrons in this research will result in a multipactor discharge where other multipactor models would not predict multipactor breakdown to occur. This in effect means that in certain situations, the multipactor breakdown level predicted by the model developed in this research could be lower than other multipactor models [43].

Due to the generalized approach used in this research, it was deemed important to include the effects of reflected primaries in the model since the model developed in this research could potentially be used for arbitrary complex structures. The results of the added accuracy of this research when compared to other models will be shown in Chapter 5.

In order to model the reflected primaries within the secondary emission model, it is important to be able to estimate the number of reflected primaries in the multipactor discharge and assign realistic launch energies to the particles.

This work will use the approach described by Spangenberg [47], who studied the properties of reflected primary particles and using empirical data found the following:

1. **In-elastically Reflected or Re-diffused (Mid-Energy)**: 7% of the emitted electrons are launched mid-energy, ranging from 50eV to 98% of the incident electron impact energy. Using empirical measurements, Spangenberg was able to define the number and range of energies for typical re-diffused primaries. In the model developed in this research a randomized uniform distribution function was used to assign individual launch energies to the re-diffused primary electrons.

2. **Elastically Reflected or Backscattered (High Energy):** These particles are actually reflected primary electrons and are not "emitted" in the strictest sense. 3% of the secondary electrons are considered reflected primaries and are very close to the impact energy (usually 99%) of the incident particle.

The approach above was used in addition to Vaughan's secondary emission formulas, in order to create a more realistic representation of the physical emission process. Most other multipactor models are not accurate representations of the physical process as they simply use Vaughan's formulae to model the secondary electrons and do not account for reflected primaries which have been shown to affect predicted breakdown levels.

4.5.4 True Secondary Electron Tracking

Many previous multipactor models have used the macroparticle theory [29],[14], [30] where by the maximum number of particles in the simulation never increase. Each macro-particle is usually associated with a base weighting and is launched as a seed electron. When a marco-particle impacts a surface, its weighting is multiplied by the secondary emission yield of that impact. At any point within the simulation, the weighting of a macro-particle represents the effective number of secondary electrons that it has generated. In other words, a macro-particle can represent all the secondary electrons it has created, but only within a single particle. Therefore, each macro-particle represents a history that includes several generations of secondaries.

This method is used for computational efficiency and is accurate in some geometries, however it cannot be universally applied. Its main limitation arises when the aspect ratio (ration between length and height) of the geometry being studied is very large and particles start to escape from the gap. This makes the macroparticle method inaccurate since as time progresses many macro-particles will escape the gap which implies that all its effective secondary particles have also escaped the gap, which might not be physically true. For example, if a macro-particle with a weighting of 1000 escapes the region, it implies that 1000 electrons have escaped the gap, which might not be true since the probabilistic nature of the secondary emission process makes it highly unlikely that two particles will follow the same trajectory. Therefore, this could result in a much higher predicted breakdown voltage than the empirical results will yield. This effect can be readily observed when low field regions are adjacent to high field regions as in fringing fields [26] and significantly affects the breakdown voltage.

A variation on the macroparticle concept is the enhanced counter function. Using this method, researchers have handled secondary electrons by using Eqn. 4.45 as shown in [5],[48],[49].

$$e_N = \Pi_{1=1}^{N} \delta_i \tag{4.45}$$

where N is the total number of impacts, i is the index for each impact and δ_i is the SEY calculated for each impact. When e_N for a certain particle converges to 0, that

particle is dropped. If e_N increases beyond a minimum level, the model predicts a multipactor discharge could occur. The result of this approach is that once again true secondary particles are not tracked and the SEY is just recorded to predict the onset of multipactor breakdown. This approach is sufficient for simpler structures with no fringing field profile, however it would be inaccurate if used within arbitrary structures.

Another inaccuracy with the macroparticle approach is that information about the energy distribution of emitted electrons cannot be determined since that information is integrated over and smoothed out[43]. This means that a macroparticle approach cannot differentiate between reflected primary electrons and true secondary electrons. As explained in section 4.5.3, this information has to be considered in the interest of accuracy and in order for the model to represent the physical emission process as closely as possible.

Since the multipactor procedure developed in this research is aimed to be used for complex structures, the inaccuracies inherent in the macroparticle approach are unacceptable. Therefore the model developed in this research calculates the trajectory of each individual electron as it takes part in the multipactor discharge. Although this is computationally expensive, it is important that every particle be tracked individually due to the probabilistic nature of the emission process. In other words it is highly unlikely for two particles to ever follow the same trajectory or have the same impact parameters, and a robust secondary emission model should take this into account. However, even though the approach of individual tracking of electrons is computationally expensive, the gains made in the accuracy of the model using this method and other methods described earlier in this chapter, allow for far fewer seed particles required in simulations when compared to other multipactor models. This makes the multipactor model developed in this research far more efficient compared to other models and is discussed further in Chapter 5.

4.6 Conclusion

This chapter discusses the SEM developed in this research in detail. Basic SEM parameters such as SEY and emission direction vectors are discussed as well as more advanced concepts in the secondary emission process. The inclusion of these advanced concepts within the model, result in a highly efficient and generalized multipactor model as will be shown in Chapter 6. Additionally, the inclusion of these advanced secondary emission concepts results in a robust SEM that is aligned to the phenomenological behavior of the secondary emission process thereby providing more accurate multipactor prediction results. Unlike most other multipactor models, the secondary emission concepts taken into consideration in this multipactor model are:

1. The careful modeling of the inelastically and elastically reflected primary electrons such that the susceptibility curves for multipactor breakdown are

broadened. This effect cannot be predicted by other models [8],[30],[26] since they do not account for high energy reflected primary particles.

2. The individual tracking of secondary electrons such that no enhanced counter function or macro-particle approach is used, resulting in more accurate modeling of particle trajectories in fringing fields and non-uniform fields.

3. The modeling of the emission of 'out of phase' particles that result in an enlarged phase-range and the lowering of the multipactor breakdown level [43]

4. Coupling of primary impact energy with the energy distribution of the secondary electron emission energy to provide a realistic range of energies for particle emission. Without this consideration, some model use a very narrow-band approximation of energies as in [46] and [5], which is not a realistic representation of the physical emission process.

Since the model developed in this research takes into account these secondary emission characteristics, the model is well suited to predict multipactor breakdown in complex arbitrary structures. This is because, unlike other multipactor models, the model developed in this research is a much closer representation of the physical emission process. Therefore, when used to predict multipactor breakdown for more complex structures with non-uniform fields and/or fringing fields, this model can deliver more accurate multipactor prediction levels when compared to other models. This is discussed further in Chapter 5.

Chapter 5

Multipactor Model & Simulation Results

Chapter Summary

This chapter first details the numerical algorithm used in the final multipactor model. Components of the numerical algorithm such as the interpolation scheme as well as the numerical integrator used to solve the differential equations of motion are discussed. The Dormand-Prince numerical method which itself is in the family of Runge-Kutta solvers is used in this research work due to its accuracy and extended numerical stability [50].

The second part of this chapter discusses how each component within the model (detailed in earlier chapters) is integrated into the overall multipactor model. For additional insight, a simplified flowchart is also presented to give the reader a high-level view of the model developed in this research work.

Finally, the chapter analyzes predicted breakdown levels for RWG and square axial structures and compares the results with ESA curves and Sazontov et. al. For lower order multipaction in rectangular waveguides and multipaction in low impedance square-axial geometries, the results were found to be in good agreement with curves from ESA and Sazontov. This is expected, since the parallel plate approximation holds true in both cases. For higher order multipaction in waveguides, the results of the model diverged from ESA and Sazontov, and were found to typically be between the breakdown levels predicted by ESA and Sazontov. The reason for the divergence of the results in ESA's case is due to the fact that the uniform field assumption does not hold true for higher order multipaction in waveguides. In Sazontov's case, the divergence is due to the fact that their secondary emission model does not account for reflected primaries, which results in the prediction of higher breakdown levels as explained in Chapter 4.

Results for the low impedance square axial TL was in good agreement with ESA curves and Woo's results, as expected. When compared to ESA's and Woo's

breakdown levels, results for the high impedance square axial TL, were found to be much closer to Woo's empirical results for coaxial lines. The results were found to be much higher than ESA's predictions since ESA's models do not account for the electron drift effect and fringing field effect. These effects cause a significant increase in the breakdown voltage. The results were found to be much closer to Woo's empirical results, although slightly higher, because co-axial lines have a uniform field distribution which results in a lower breakdown level, as has been studied in the parallel plate approach in Chapter 2.

Finally this chapter outlines the strengths and advantages of the multipactor model developed in this research. Advantages of the generalized procedure used to develop the model in this research enables it to leverage the strength of modern CEMs to potentially predict multipactor breakdown in any complex commercial structure since the intricacies of the EM field analysis has been abstracted to the CEM. Additionally, results have shown to be accurate with far fewer seed particles than are required by other multipactor models, making this model much more computationally efficient.

5.1 Numerical Engine

With the secondary emission model studied, this section outlines the next major part of the multipactor model which is the numerical algorithm that evaluates the particle trajectory. In section 3.1, the trajectory of the particle was derived analytically, and it can be easily seen that for more intricate geometries deriving an analytical mode could be very challenging and tedious. The numerical engine can evaluate the particle trajectory numerically, based on a set of differential equations of motion. This approach allows the multipactor model to function independent of geometry, since the dimensions of the geometry will only impose the boundary conditions for the particles, and the fields within the device, both of which are abstracted to the CEM as introduced in Chapter 1. Since the fields present in the device can be calculated using any Commercial Electromagnetic Simulator (CEM), the multipactor model developed in this research can function independently of geometry as long as the field information of the device and its boundary conditions are imported into the model. That is to say, the multipaction model developed in this research shifts the complexity of field calculation from the multipactor modeler itself to a CEM. This is a major point of distinction between this research work and many other multipactor simulators. This enables a more flexible multipactor model since the code leverages the advanced field computation capabilities of industry standard CEMs like Ansoft HFSS, to provide more precise results for the multipactor curves. The numerical engine itself has many subcomponents, and each will be explored in detail in the following sections.

For this research work, Ansoft HFSS was the CEM chosen to evaluate the fields within the device, however the same theory applies to other CEMs. The numerical engine creates a list of mesh grid points that will be used to calculate the particle trajectory. These points can be fed into Ansoft HFSS or any other CEM in order to calculate the field information at the grid points. Since the field information at the grid points have to be input into the model before the simulation can be performed, the field information is typically extracted at time $= 0$, however an offset can be added before simulations are performed. The spacing of the grid data can be different in the x,y and z direction, however they must be uniform in their respective dimension. Using the field information delivered by Ansoft HFSS, at a high level, the numerical engine performs the steps below to evaluate each particle's trajectory: Each step is described in detail in following sections.

1. **Locate** eight closest cube grid points to current particle position
2. **Interpolate** the field information (magnitude & phase) from the eight grid points to particle position.
3. **Calculate** particle's current velocity & position given new field information and velocity & position of particle at previous time step
4. **Store** particles current velocity & position; **Check** if particle location satisfies boundary condition
   (a) *If boundary condition is satisfied:* Terminate execution of current particle & load next particle
   (b) *If boundary condition is not satisfied:* Repeat from step 1

As stated earlier the field information extracted from Ansoft HFSS is valid at a specific time step. It would be impractical to require a new simulation in the CEM to get the field information at every time step in the simulation. For this reason, in order to overcome this limitation, a generalized approach for the advancement of time and phase was used. Using this generalized approach, only one CEM simulation ever needs to be performed. Once this field information is fed into the multipactor model, the time and phase are advanced using the approach discussed next.

5.1.1 Time and Phase Advancement

The advantage of using the approach outlined in this section is that it can be used with any CEM, not just Ansoft HFSS. The multipactor code advances time by advancing the phase of the EM field information since:

$$\omega t = \phi \tag{5.1}$$

Using this approach only a single simulation needs to be performed in the CEM at a specific time step. The following steps briefly detail the actual steps performed to advance time within the numerical algorithm:

1. Configure grid spacing according to accuracy required in breakdown prediction [typically grid spacings of 1 mil is sufficient for reasonable accuracy and computation time]

2. Use Ansoft HFSS to extract field information on grid data in region of interest or entire device at a specific time step such as time = 0

3. Ensure that field information in extracted data include: Magnitude of real and imaginary components of fields, resolved to Cartesian coordinates. In other words, the extracted data should have :

   (a) Grid point position in Cartesian coordinates

   (b) (Mag($\text{Field}_{\text{Re},i}$), Mag($\text{Field}_{\text{Im},i}$) where i = x,y,z

4. Calculate phaseshift of grid point (ϕ_d) as:

$$\phi_{d_i} = \arctan\left(\frac{\text{Im}(Field)_i}{\text{Re}(Field)_i}\right) \quad \text{where } i = x, y, z \tag{5.2}$$

5. Calculate total phaseshift (ϕ_{tot}) as the sum of ϕ_d and the advancement of phase (time) in current iteration:

$$\begin{aligned} \phi_{tot_i} &= \phi_{d_i} + \phi_t \\ &= \phi_{d_i} + \omega t \quad \text{where } t = current\ time,\ i = x, y, z \end{aligned} \tag{5.3}$$

The total phaseshift is an important quantity that is used in the trilinear cube interpolation described in the next section. Although a simple technique, this approach is an important step in ensuring the generalized approach of the model developed in this research. Since any CEM is capable of extracting the field information required above, this advantage of this approach is evident. In essence the multipactor model developed in this research does not need to be tightly integrated with any EM solver, since this task is abstracted to the any CEM. This along with the surface normal calculation method in section 4.2 makes the model developed in this research generalized, and gives it the advantage of leveraging the advanced EM modelling techniques used by industry-standard EM solvers. Other multipactor models that use specialized EM solvers such as SLANS and Superfish [33], are not widely used in the commercial space industry and are limited in the structures they are able to analyze. The multipactor model presented in this research does not have this limitation since it leverages the advanced EM modelling techniques used by CEMs, therefore the model developed in this research with *one additional code*, has the potential to be used to predict multipactor breakdown in any commercial microwave device.

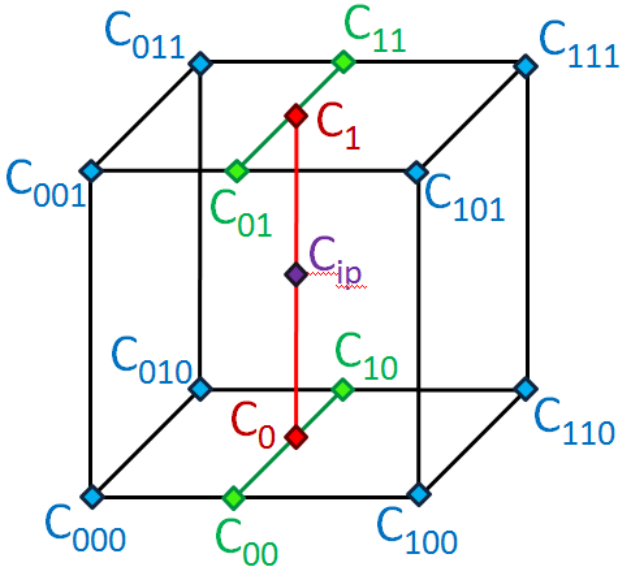

Figure 5.1: Cube showing Trilinear Cubic Interpolation

5.1.2 Field Interpolation

In order to numerically calculate the particles position and velocity for a given time, the particles previous position and velocity and the field information at the particles current location are required. This section outlines the Trilinear Cube Interpolation algorithm that is used to calculate the field at the particle's current location. As an example, assuming the grid points located from C_{000} to C_{111} as shown in Figure 5.1, the algorithm works sequentially first from the outer edges of the cube at the grid points and progressing toward the particle's location.

A sequence of seven steps is required to calculate the field information for every interpolation point (ip). As shown in 5.1 the first step interpolates the eight grid points on the edges of the cube to four points $(C_{00}, C_{01}, C_{10}, C_{11})$ within the same planar surface as the grid points. In other words, the first four equations interpolate along the x-axis. This is done by the following four equations:

$$C_{00} = \left(\frac{abs\left(ip_x - C_{100_x}\right)}{abs\left(C_{100_x} - C_{000_x}\right)}\right) \cdot f(C_{000}) + \left(\frac{abs\left(ip_x - C_{000_x}\right)}{abs\left(C_{100_x} - C_{000_x}\right)}\right) \cdot f(C_{100}) \quad (5.4)$$

$$C_{10} = \left(\frac{abs\left(ip_x - C_{010_x}\right)}{abs\left(C_{010_x} - C_{110_x}\right)}\right) \cdot f(C_{110}) + \left(\frac{abs\left(ip_x - C_{110_x}\right)}{abs\left(C_{010_x} - C_{110_x}\right)}\right) \cdot f(C_{010}) \quad (5.5)$$

$$C_{11} = \left(\frac{abs\left(ip_x - C_{011_x}\right)}{abs\left(C_{011_x} - C_{111_x}\right)}\right) \cdot f(C_{111}) + \left(\frac{abs\left(ip_x - C_{111_x}\right)}{abs\left(C_{011_x} - C_{111_x}\right)}\right) \cdot f(C_{011}) \quad (5.6)$$

$$C_{01} = \left(\frac{abs\left(ip_x - C_{001_x}\right)}{abs\left(C_{001_x} - C_{101_x}\right)} \right) \cdot f(C_{101}) + \left(\frac{abs\left(ip_x - C_{110_x}\right)}{abs\left(C_{001_x} - C_{101_x}\right)} \right) \cdot f(C_{001}) \quad (5.7)$$

where $f(C_{aaa})$ holds the field values stored at that point. In other words, this is a function of the field information extracted from the CEM for every grid point. The next step interpolates the four points to the point where the planar projection of the interpolation point falls. These points are C_0 and C_1 in 5.1. This is done by the following two equations:

$$C_0 = \left(\frac{abs\left(ip_y - C_{00_y}\right)}{abs\left(C_{00_y} - C_{10_y}\right)} \right) \cdot f(C_{10}) + \left(\frac{abs\left(ip_y - C_{10_y}\right)}{abs\left(C_{00_y} - C_{10_y}\right)} \right) \cdot f(C_{00}) \quad (5.8)$$

$$C_1 = \left(\frac{abs\left(ip_y - C_{01_y}\right)}{abs\left(C_{01_y} - C_{11_y}\right)} \right) \cdot f(C_{11}) + \left(\frac{abs\left(ip_y - C_{11_y}\right)}{abs\left(C_{01_y} - C_{11_y}\right)} \right) \cdot f(C_{01}) \quad (5.9)$$

Finally the field information is calculated at the interpolation point (C_{ip}) as:

$$\begin{aligned} C_{ip} &= \left(\frac{abs\left(ip_z - C_{1_z}\right)}{abs\left(C_{0_z} - C_{1_z}\right)} \right) \cdot f(C_0) + \left(\frac{abs\left(ip_z - C_{0_z}\right)}{abs\left(C_{0_z} - C_{1_z}\right)} \right) \cdot f(C_1) & (5.10) \\ &= f(C_{ip}) & (5.11) \end{aligned}$$

Here the field information at the particle location is $f(C_{ip})$ and these are the values that are used to calculate the velocity and position of the particle in the next time step. The model was tested for varying grid sizes from 10 mil step sizes down to 0.1 mil step sizes. It was found through numerous test cases that a step size of 1 mil is sufficient for reasonable accuracy of breakdown results. For cases where the field intensity changes dramatically, smaller step sizes could be chosen within the model.

5.1.3 Trajectory Differential Equations

Once the field information at the particle location has been found, a set of differential equations are solved to compute the particle velocity and position. As with any set of differential equations, initial conditions for the particles must be properly set in order to model their trajectory properly. In this work, initial conditions for the particles are set randomly. Due to the probabilistic nature of secondary emission process, the model requires range of values for all initial conditions such

as launch energies (velocities), launch positions, and launch directions. The multipactor model then randomizes the values within the predefined limits set by the user. The differential equations are setup for the Cartesian coordinate system as:

$$\frac{dv_x}{dt} = \left(\frac{q}{m}\right) \cdot |E_x| \tag{5.12}$$

$$\frac{dv_y}{dt} = \left(\frac{q}{m}\right) \cdot |E_y| \tag{5.13}$$

$$\frac{dv_z}{dt} = \left(\frac{q}{m}\right) \cdot |E_z| \tag{5.14}$$

$$\frac{ds_x}{dt} = v_x \tag{5.15}$$

$$\frac{ds_y}{dt} = v_y \tag{5.16}$$

$$\frac{ds_z}{dt} = v_z \tag{5.17}$$

The numerical solver chosen to solve this set of differential equations is quite important due to the adaptability of step size and accuracy of the results. In this work, the Dormand-Prince [50], [51] numerical solver was used. This solver falls in the Runge-Kutta family of solvers since it builds on the Runge Kutta 4th order solver, and uses six function evaluations to calculate 4th and 5th order accurate solutions. The error between the two solutions is used as the error for the 4th order results. Dormand-Prince was chosen since it has an extended range of absolute stability [50] and has the ability to deal with extremely large variations (orders of magnitude) in the EM fields within the device. Dormand Prince solver is an extremely robust integration method since it has the ability to perform extremely small integration steps that are required when tracking the particle during curved trajectories and can also increase the step size for to allow for rougher integrations steps during straight trajectories. The computing time limitation calls for the adaptive capability of the integration method, while not sacrificing accuracy. Additionally, Dormand Prince solver has been found to be more efficient than the Runge-Kutta-Fehlberg solvers [50].

5.2 Multipactor Model Algorithm

As introduced in chapter 1, and shown in Fig. 1.1 (repeated below for convenience) this research uses a generalized procedure to develop an efficient method for multipactor modeling. Component 1 in Fig. 5.2 is discussed in Chapter 5, and components 2 and 3 are presented earlier in this chapter. Together the three components make up the generalized procedure that is used to develop an efficient multipactor model that could be used to analyze complex structures found in the commercial space industry.

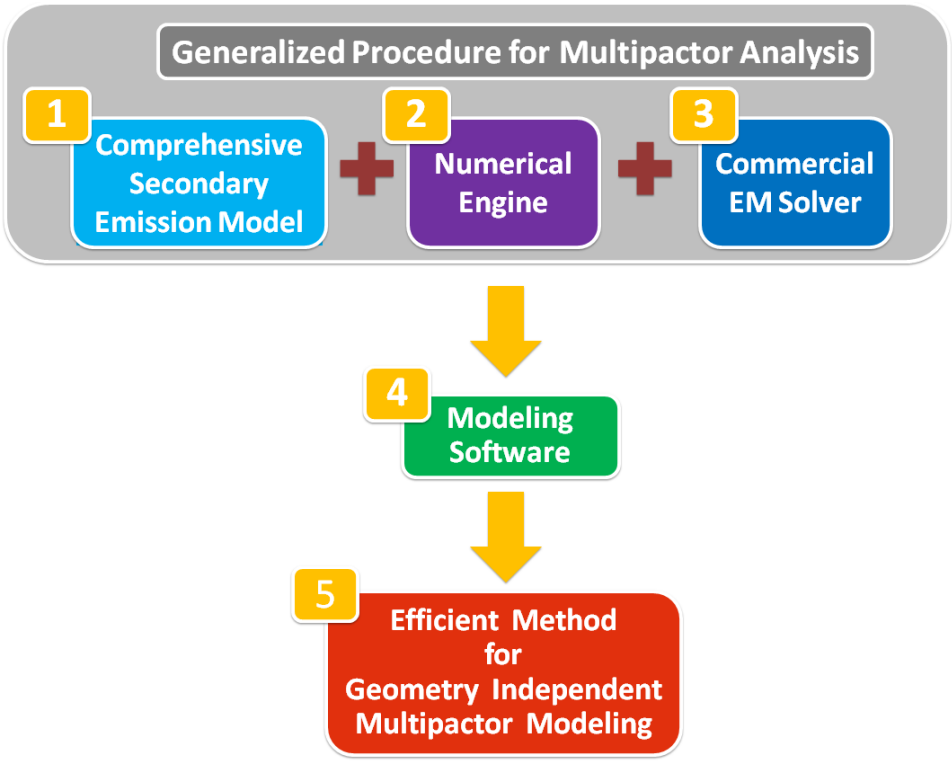

Figure 5.2: Generalized Procedure used in this research to develop an efficient method for geometry independent multipactor modeling

Each component was then translated into a programmatic algorithm and eventually to modeling software in order to implement the multipactor model presented in this thesis. This implementation is shown as Component 4 in 5.2. The implementation process is relatively trivial since it is just a matter of computer programming, therefore only a brief overview of the implementation of the developed multipactor model is provided, since it is not a major part of this research.

The algorithm used to implement the multipactor model is briefly discussed below. The steps outlined in this section can be viewed programmatically using the algorithm flowchart at the end of this section.

User Input

In order to use the multipactor model to predict the breakdown levels of a RF device, there are a number of parameters that have to be initialized. Most of these parameters have been initialized to default values but these values can be changed to see the effects the changes have on the breakdown threshold. Some of the basic parameters that must be initialized before a simulation can start are number of seed particles, energy and position spread of seed particles, frequency of RF carrier and number of particle generations to be simulated. Due to the

probabilistic nature of secondary emission process, the model requires a range of values for all initial conditions such as launch energies (velocities), launch positions, and launch directions. The multipactor model then randomizes the values within the predefined limits set. Parameter ranges can be set to be as large or constrained as required, in order to see the effects on the breakdown prediction.

Additionally, the secondary emission properties of the coating material on the RF device must also be set. These parameters include the SEY (δ), surface condition parameters k_{sv} and $k_{s\theta}$ and E_{max} as discussed in Chapter 4.

A number of different plots can also be generated during such as a particle trajectory plot in the structure in 2D and/or 3D, individual particle tracker plots, SEY discretization error plots and mesh grid plots.

Loading Queue

According to the initialization ranges, seed particles are then loaded into a particle event queue (Q). All particles are initialized randomly using a uniform probability distribution based on the user input range. The parameters that are randomized are launch phase (all seed particles are launched randomly within the first half cycle of the RF field), launch position, launch energy and launch direction.

Numerical Engine

Once the seed particles have been loaded into the Q, the numerical engine loads the first particle in the Q that is still active (track flag equals 1). For each active particle, the numerical engine performs the following steps:

***Step* 1 :** Find eight closest grid points to particle location

***Step* 2 :** Advance to the next time step and calculate the phase information for each grid point (See Chapter 5)

***Step* 3 :** Interpolate field and phase information from eight grid points to current particle location (See Chapter 5)

***Step* 4 :** Solve particle equations of motion using differential equations and the Dormand-Prince RK45 solver (See Chapter 5)

***Step* 5 :** Apply boundary conditions of geometry
- *If impact does not occur* go to Step 1. If maximum number of cycles are reached, deactivate particle (Trackflag equals zero) and skip to Step 7.

- *If impact does occur*, go to Step 6.

***Step* 6 :** Log impact even in Secondary Q

***Step* 7 :** Load next active particle in Q and go to Step 1.
- *If no more active particles exist*, skip to Step 8

Secondary Emission

Once all the previous generation particles have been tracked, the secondary array is processed according to the secondary emission model discussed in Chapter 5.

***Step* 8 :**Calculate impact angle using velocity vector and surface normal

***Step* 9 :** Load surface conditions (for example: polished surface vs. rough surface) and material properties such as SEY_{max} etc. (See Chapter 4)

***Step* 10 :** Calculate SEY yield according to material properties and discretize SEY using uniform distribution. (See Chapter 4)

***Step* 11 :** For each true secondary electron: assign launch energy based on primary impact energy, and direction. Load into Q (See Chapter 4)

***Step* 12 :** Set number of active Rediffused and Backscattered particles (See Chapter 4) and activate within Q

***Step* 13 :** For each active primary particle: calculate launch energy and direction.(See Chapter 5)

***Step* 14 :** If maximum number of simulation generations have not been reached, load first active particle in Q and go to Step 1.

In order to give the reader additional insight, a simplified flowchart depicting the actual implementation of the multipactor model developed in this research is provided next.

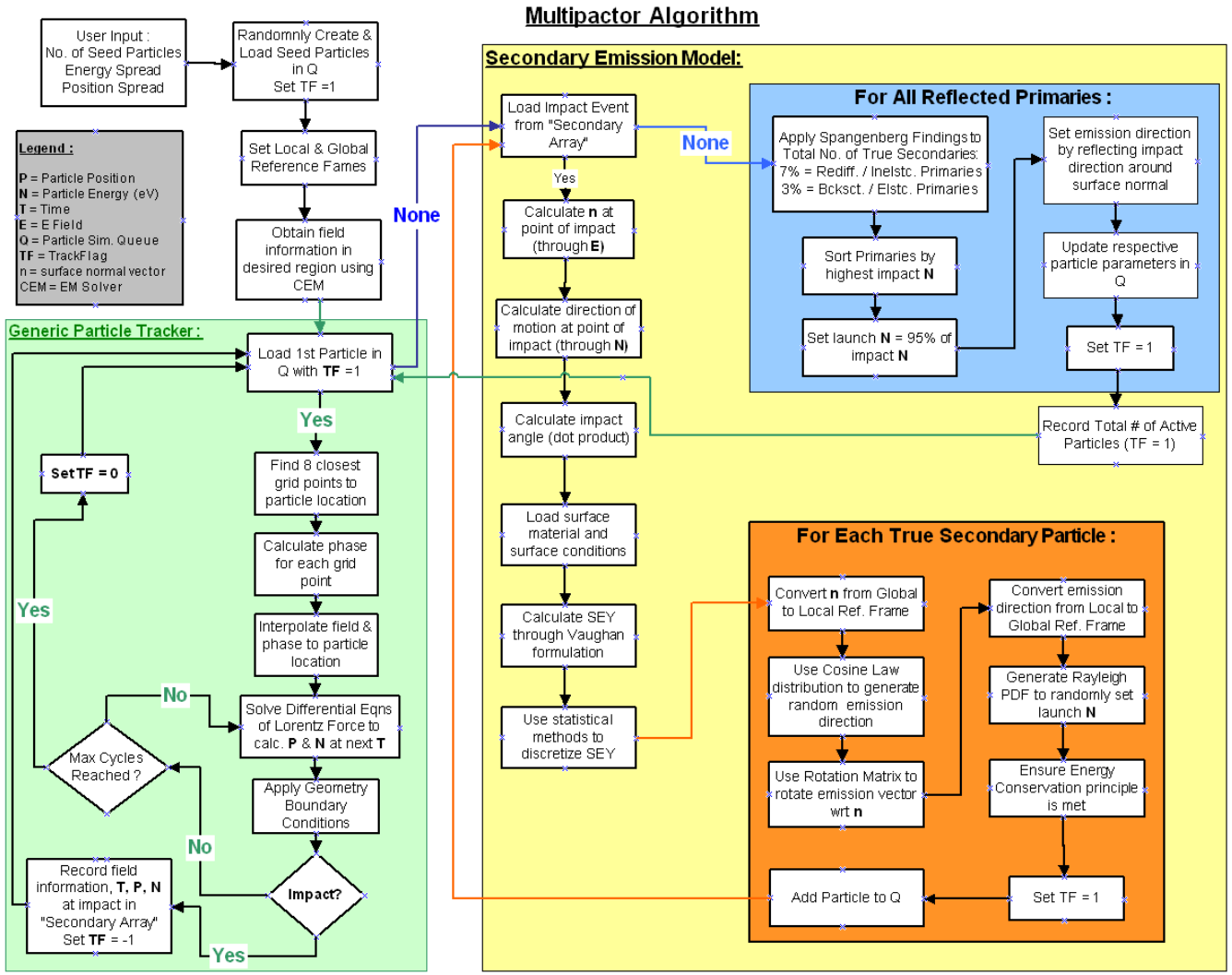

Final Simulator Algorithm Flowchart

5.3 Simulation Results

This section presents the results for simulations performed for various orders for the waveguide and square-axial transmission lines. For simulations in the RWG, 50 seed particles were launched, with a launch energy randomly distributed between 0 to 4 eV. Launch directions were not restrained in any axis, and seed particles were launched near the center of the waveguide. Seed particles were launched at random phases in the first half cycle of the RF field and surface conditions for the material was set to 'smooth' Power was increased in variable step sizes for greater accuracy of the predicted breakdown voltage. The results of the simulations were compared using three sources.

The first is ESA's widely used Multipactor Calculator (discussed in section 2.2.5) and the second source was Sazontov et. al. models (discussed in section 2.2.6) The ESA curves were chosen since they are the industry standard at the European Space Agency [6] and the commercial space industry. Models by Sazontov et. al. were chosen due to the number of their algorithms that provided good agreement between results. Finally, the 'Woo report' (discussed in section 2.1.4) was chosen since it is considered a very import work in the area of multipaction analysis for axial transmission lines and has tremendous number of citations in this research area. Since many other multipactor models are not widely available for public use [34][7][14][36], these models could not be tested.

5.3.1 Waveguide Simulations

For multipactor breakdown prediction in waveguides, simulations were performed using the analytical engine and the numerical engine for comparison. The analytical engine (MP_A) calculates the field information as described in Chapter 3, and solves the analytical equations of particle motion derived earlier. This results in extremely fast computation times for the analytical version. In fact, the analytical engine is used first to obtain rough regions of breakdown, and the numerical engine is then used to obtain more realistic results. The numerical engine (MP_N) detailed in Chapter 5, coupled with the field information from Ansoft HFSS is used to predict the breakdown voltage once a breakdown region was found analytically. Typically, the numerical simulations were started at $100V$ below the analytical breakdown voltage, to correctly predict the onset of multipactor breakdown.

The same Secondary Emission model was used in both simulations. The results can be found in the Table 7.1, note that the numerical results are always higher than the analytical results. This is due in part to the fact that there are some simplifications made in the derivation of the analytical equations of motion, as described in Chapter 3. The simplifications were made in order to simplify the analysis, but introduced an error in the position of the particle over small time increments. As the transit time of the electrons in the gap increases, the error

compounds, resulting in larger discrepancies between the numerical and analytical versions of the model. This trend is clear in the Table 7.1.

Additionally, Sazontov results are typically higher than the results obtained from the model developed in this research. This is because Sazontov's models use Vaughan's formulation for secondary emission, but the model does not consider high energy reflected particles[35]. As was explained in section 4.5.3, most multipactor models do not account for reflected high energy particles which has the effect of lowering the breakdown threshold as evidenced by the results of the numerical engine when compared to Sazontov. Finally, the breakdown levels of this research work shows a substantial increase in voltage for higher orders when compared to the ESA results. In fact, the higher the order, the larger the discrepancy. This is due to the fact that the ESA curves use a parallel plate geometry that assumes a constant field between the plates. This modeler uses the field information of a waveguide, therefore the particles are driven by a non-uniform field. Since particles in vacuum tend to drift from a region of high field to regions of lower fields, this implies that the a higher breakdown voltage is required to offset this drift, since particles that drift toward the low field regions will not eventually decelerate and fall out of resonance or generate only low-energy impacts producing no true secondary electrons. This is the reason why the space industry finds the ESA curves to be quite conservative in their breakdown prediction levels when testing for multipaction in a lab environment, where waveguides tend to breakdown at significantly higher levels than that predicted by ESA. This means that ESA typically underestimates the power handling capability of the device.

Higher Order Multipaction in Rectangular Waveguides

Fig.5.3 shows the different particle growth curves for the different power levels for 9th order multipaction with a 10 mil gap at 56 GHz as the input power is increased. Fig.5.3 shows the corresponding increase in voltage levels until the breakdown level of 1150 V_p as recorded in Table 7.1 is reached. The figure shows the particle growth versus generation number for various peak voltages from $800V_p$ to $1500V_p$ where the seed particles are considered first generation, the secondary particles created by the first generation are called second generation and so on. It is important to note that 5.3 does not depict the particle growth versus time, which has a different characteristic. Note that although the curves in Fig.5.3 are for the case mentioned above, the curve will have the exact same exponential characteristic for any device in the mulitpaction region, regardless of the device and multipactor order. As such the trends seen in electron population growth (Fig.5.3) are not geometry dependent. It is clear from the curves that between $800V_p$ to $975V_p$ there is no substantial population growth. This is because the field strength is too weak to cause significant secondary emission from the walls. However this region could be called an equilibrium region, where the electrons being absorbed and lost due to being out of phase compensate for the few secondary electrons being created, and so population

growth does not converge to zero, nor does it increase exponentially in a reasonable about of time, which is why this region could be called a steady-state region. Between $975V_p$ to $1050V_p$ the field strength is now strong enough to cause impacts with sufficient energy for secondary emission. However, the second requirement for multipaction which is the resonance condition has not been initialized. At $1150V_p$ both conditions are now met with SEY > 1, and the resonance condition for electron growth. We can see the effects of these phenomena by the exponential growth in the particles in relatively few generations. Finally increasing the power above this threshold, sends the waveguide into deep breakdown where by the particle population growth accelerates exponentially in just a few generations, as can be seen by the curves of $1250V_p$ and $1500V_p$. Table 7.1 summarizes the simulation results of the waveguide simulations for 1st order to 9th order and compares the results with ESA and Sazontov et. al.

Order	Freq (GHz)	Gap (mm)	Fd (MHz-cm)	Z (Ω)	ESA (V_{pk})	Sazontov (V_{pk})	MP_A (V_{pk})	MP_N (V_{pk})
1	10	0.254	254	16.308	262	240	224	235
3	10	0.508	508	32.617	385	425	403	427
5	34	0.254	863	10.334	688	760	659	674
7	44	0.254	1117	10.218	826	990	815	870
9	56	0.254	1422	10.154	1023	1345	1032	1150
19	10	2.54	2540	163	1796	3000	2051	2136

Table 7.1 - Multipactor Brakedown Results for Waveguide

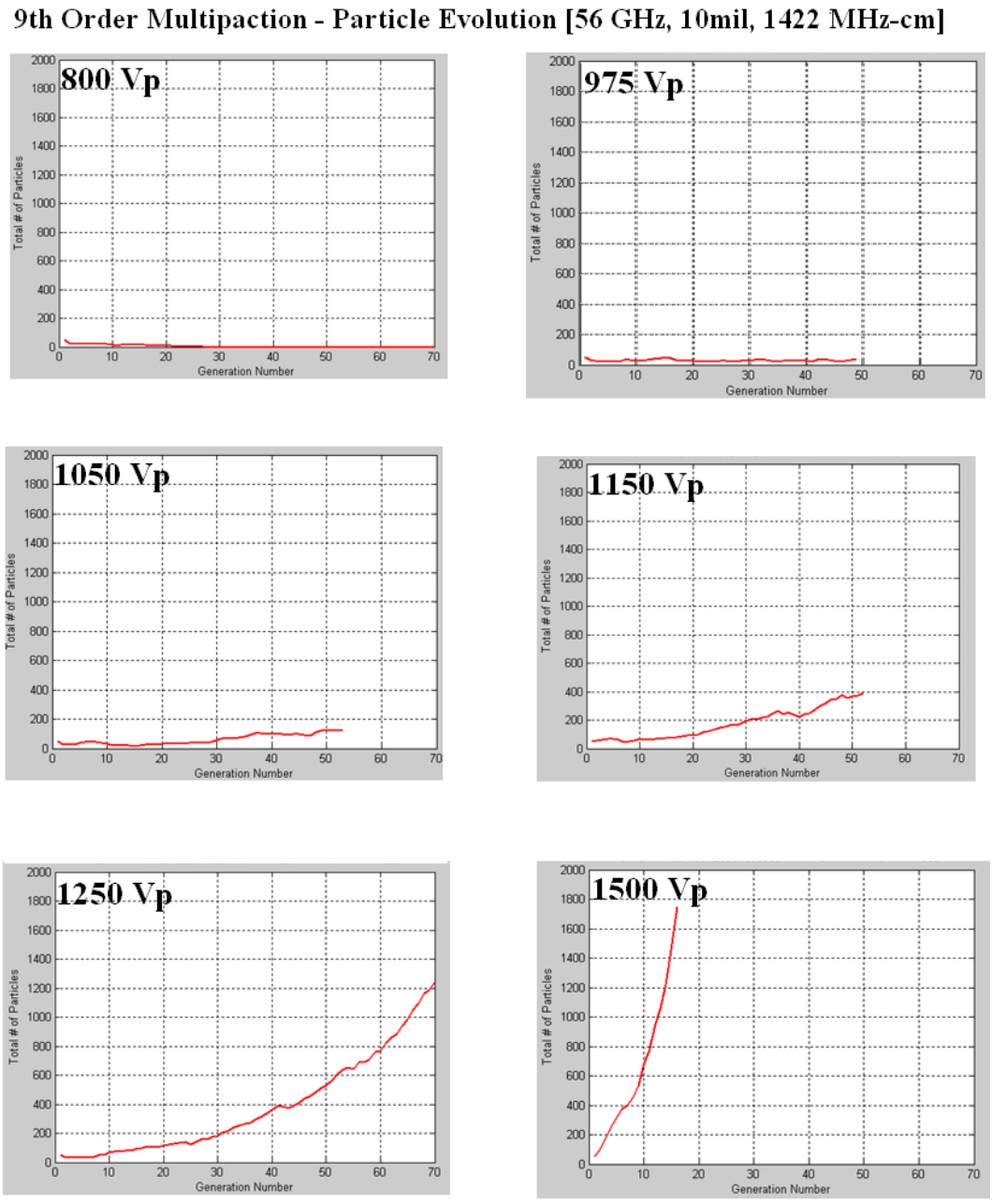

Figure 5.3: Particle Growth Curves for 9th Order Multipaction in Waveguides

5.3.2 Square-Axial Transmission Line

Simulations were also performed using a square axial transmission line structure to see the effects of fringing fields on the breakdown voltage. The first set of simulations was performed on a square axial transmission line with an impedance of 30 ohms. The outer conductor was sized at 100 mils and the inner conductor is 60 mils for a ratio of 1.6. With the impedance this low, the breakdown voltage of this structure should be quite close to that of the breakdown voltage of the parallel plate. To understand why this is so, refer to Fig.5.4 and Fig. 5.5, note that the field lines in this structure are quite uniform and directed along the x or y axis. Therefore, the field representation of this structure is quite similar to that of the parallel plate geometry. In fact, as the impedance of the square axial decreases, the field representation of the square-axial structure looks increasingly like that of a parallel plate geometry. The simulations were performed for 1st and 3rd order multipaction and as expected the breakdown voltage predicted by this model is quite close to the levels predicted by ESA and Sazontov as shown in Table 7.2.

Order	Freq (GHz)	Gap (mm)	Fd (MHz-cm)	Dimensions (mil)	Z (Ω)	ESA (V_{pk})	Sazontov (V_{pk})	MP_N (V_{pk})
1	0.75	0.508	76.2	Outer = 100 Inner = 60	16.308	43	40	46
3	1.5	0.508	152.4	Outer = 100 Inner = 60	32.617	93	85	96

Table 7.2 - Multipaction Breakdown Results for 30 ohm Square-Ax TL

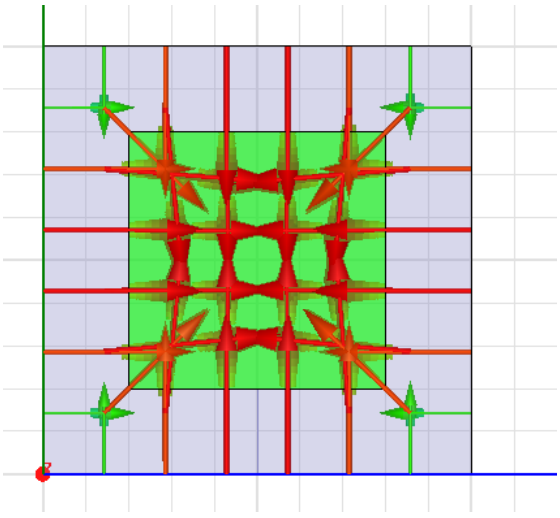

Figure 5.4: 2D view of Field vectors for 30 ohm square-axial TL [OC = 100 mil, IC = 60mil]

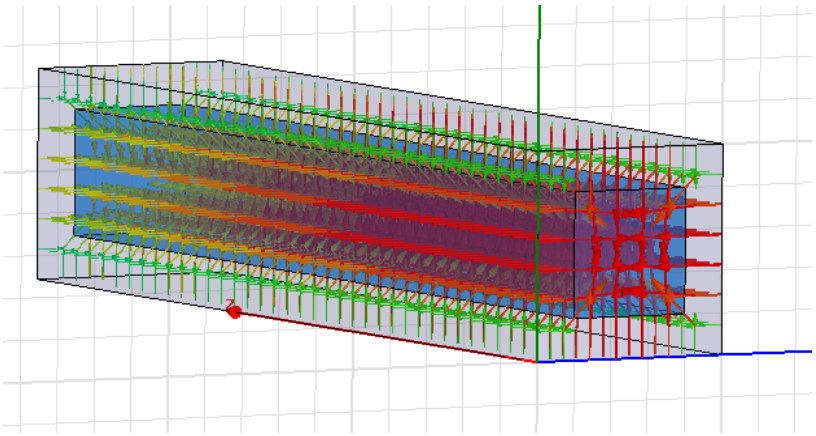

Figure 5.5: 3D view of Field Vectors for 30 ohm square-axial TL [OC = 100mil, IC = 60mil]

A second set of simulations were also performed, increasing the outer conductor from 100 mils to 300 mils. With an impedance of 91 ohms, the expectation is for the results from the numerical simulator to start diverging from the prediction levels made by the other charts. An impedance of 91 ohms was chosen in order to compare prediction results with Woo [23]. Note that since the gap size is large and a parallel plate approximation does not apply, Sazontov's multipaction results are not compared. The ESA curves are still used since its Multipactor Calculator has the option to calculate breakdown voltages for square axial lines. However, the difference between the calculator's predictions for the parallel-plate versus square-axial line was very small (less than 10 V_{peak}) which implies that the multipactor model used for the square axial lines are not very accurate. This inaccuracy is shown because the difference between the breakdown levels of a parallel-plate and a square-axial line of the same gap size is expected to be quite large (more than 100 V_{peak}) due to fringing fields [27]. Table 7.3 shows that the Woo's results although higher than ESA's predicted results are still lower than the results predicted by this model. This is expected since Woo's experimental results were obtained using a coaxial where the field is uniform. The field in the square-axial TL as shown in Fig. 5.6, is non uniform. In fact the figure shows the existence of four low field regions in each of the four corners of the structure. These low field regions cause the "electron drift" effect which is discussed later. It is important to note however, that due to these low field regions in the square-axial structure a higher breakdown voltage is required since electrons that enter these regions tend to decelerate quickly and impact with a lot less energy. Since coaxial TL has a uniform field profile, there are no low field regions and therefore no electron drift, which results in a lower breakdown level being predicted. This is similar to the case where a parallel plate approximation typically predicts lower breakdown levels than real waveguide multipaction simulations, since the PP approach assumes a uniform field.

For first order multipaction, the increase in breakdown predicted by the numerical simulator, although not very large is still significant. Referring to Fig. 5.6 and Fig. 5.7, it is clear that the field vectors are now starting to bend toward the outer walls at the corners of the conductors. This is because the gap size has increased by 100 mil (from 20 mil to 120 mil) and the effects of the fringing field are starting to become more pronounced. As electrons travel across the gap, they tend to drift toward the area of lower field intensity, and the longer an electron remains in the gap the more marked this effect becomes. The electron drift effect is the reason for the higher predicted breakdown voltages generated by the simulator.

As mentioned earlier, the increase is noticeable in 1st order multipaction but not large, however, for 3rd order multipaction, there is more than a 300% increase in the predicted breakdown. For higher orders this increase would be larger. As the multipaction order increases, electrons stay in the gap for longer periods of time since their transit times increase. This pushes the electrons further into the lower field region, and as a result a higher voltage is required to drive these particles into resonance. In this case it is clear that a parallel plate approximation of the structure will be highly inaccurate.

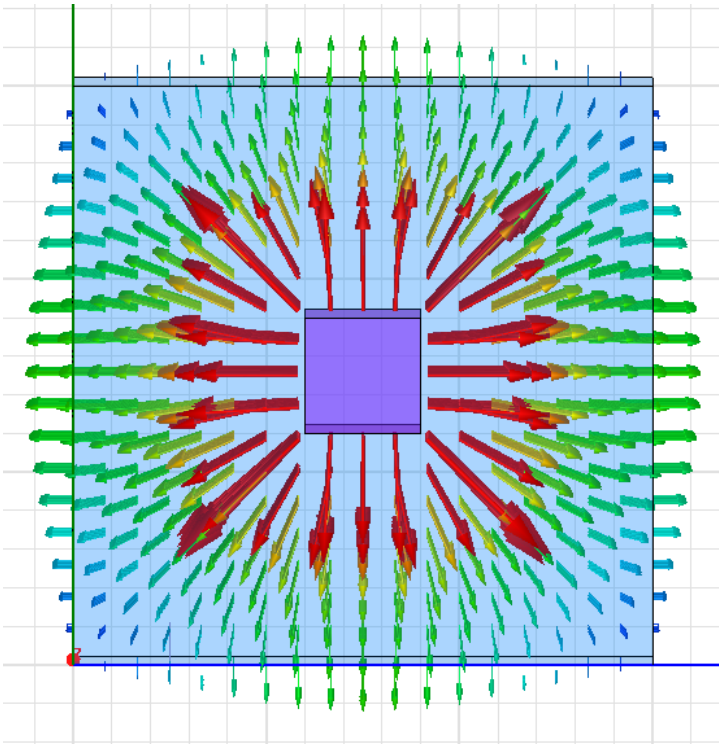

Figure 5.6: 2D view of Field vectors for 90 ohm square-axial TL [OC = 300 mil, IC = 60mil]

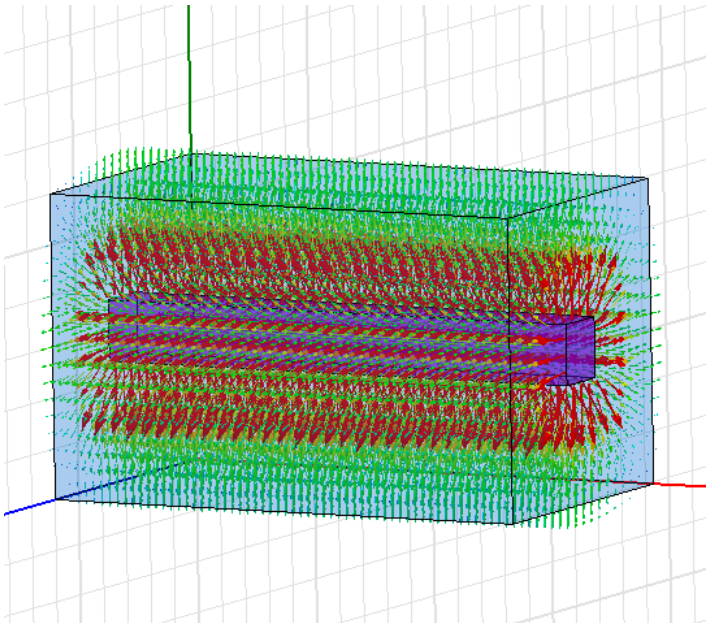

Figure 5.7: 3D view of Field Vectors for 90 ohm square-axial TL [OC = 300mil, IC = 60mil]

Order	Freq (GHz)	Gap (mm)	Fd (MHz-cm)	Dimensions (mil)	Z (Ω)	ESA (V_{pk})	Woo (V_{pk})	MP_N (V_{pk})
1	0.75	3.048	228.6	Outer = 300 Inner = 60	90.98	213	196	234
3	1.5	3.048	457.2	Outer = 300 Inner = 60	90.98	307	780	950

Table 7.3 - Multipaction Breakdown Results for 91 ohm Square Axial TL

Fig. 5.8 shows the particle trajectories within the structure as the voltage was increased from $270V_p$ to $603V_p$. For third order multipaction, the predicted breakdown level of the structure was $950V_p$. The simulator provides a 2D and 3D perspective on particle trajectories for a better analysis of the breakdown. The field vectors shown in Fig. 5.6 show the non-uniformity of the field in strength and direction. This field non-uniformity significantly increases the breakdown threshold since it is a lot harder for the resonant condition to be created and sustained since the particles are not confined to a small region of uniform field within the structure. The frequency-gap product plays a very critical role here since it directly impacts the transit times of the electrons. For very low Fd products in the low first order range, the non-uniformity will not affect the results since the wavelength of the field will be quite large. However for third order and above, the effects of this phenomenon can be shown as follows.

Fewer seed particles were set up for this simulation and launch parameters such as energy and direction were randomly assigned according to a uniform distribution. The seed particles were located in a region midway in the gap to show the effects of the fringing fields as electrons got farther away from the center of the gap where the field is uniform (Fig. 5.6). The only parameter changed between each simulation was the power, which was increased steadily until the breakdown threshold was found. The particle trajectories are colored according to their generation. For example, the trajectory of the seed particles are always red, the trajectories of the first set of secondaries are blue, third generation particles are green, fourth generation are magenta, fifth generation are black, then light-blue and finally all higher generations are colored yellow.

At $270V_p$ in Fig. 5.8 it can be seen that although the electrons impact the wall, there is almost no secondary emission. Only one secondary particle (blue) is emitted which strikes the inner conductor but almost all impacts at this voltage are low energy impacts and multipaction cannot occur.

At $430V_p$ the field is stronger and impacts create some secondary electrons, however after five generations electron population goes to zero. This is because although SEY > 1, but the resonance condition has not been created. This can be seen by the fact that although there were quite a few second generation particles created (blue), subsequent generations (green, magenta and black) do not create appreciable secondary emission due to their low energy impacts. In fact, a closer look at the 3D perspective shows that two sixth generation particles (light blue) were created at the impact site of the fifth generation (black) but they are out of phase and returned to the outer wall. The second generation electrons (blue) also return to the outer wall before impacting the inner wall, which in this case implies low energy impacts. This is verified since only one third generation (green) particle is emitted. Note that at this voltage level, no electrons impacted the inner conductor.

The voltage is then increased to 603 V_p, and this case is quite similar to the one discuss for $430V_p$. Although SEY >1, the resonance condition is not sustained, and though there are more higher generation particles emitted, eventually the population growth converges to zero. This time a few particles come very close to impacting the inner conductor before the field changes phase and they are driven to the outside wall. Note that according to the ESA curves, the structure should have been in deep breakdown at this voltage since their voltage breakdown level was around $300V_p$, but this is clearly not the case as can be seen by the particle trajectories.

Fig. 5.9, shows the particle trajectories for higher voltages. For $853V_p$, the emergence of upper generation particles (yellow) can be seen for the first time which indicates that the voltage breakdown threshold of the structure is being approached. Note the density of the particles in the left side of the structure and also that particles are now starting to come quite close to the inner conductor

and in a few cases even impact the inner conductor. These trends indicate that the voltage breakdown potential is close to this voltage. Within this range of voltage levels, the particle growth typically displays a form of equilibrium, where the number of particles being absorbed or lost (out of phase condition) compensate for the new particles being created, and a steady state is reached. This is intuitive, since the particle growth curves show a middle region of equilibrium where by the particle population does not converge to zero nor does it increase exponentially in a reasonable amount of time.

At $950V_p$, we can finally see significant secondary emission and noticeable upper generation (yellow) particles. Note the impacts on the inner conductor have now increased, which indicates that we are at the onset of multipaction. Although there are regions within the structure that are not in breakdown (right side) it is important to point out that secondary emission is occurring even when particles travel from once face of the outer conductor to another face of the outer conductor. Since we are at the onset of the breakdown, this implies that over time the population growth will have an exponential characteristic, this becomes more clear in the discussion of the next figure. It is interesting to see the effects of electron drift in at $950V_p$. Although the electron density looks uniform throughout the left region of the structure, a careful examination of the trajectory colors reveals that upper generation particle spend more time in the low field region than in the high field region. This is seen by the yellow and light blue trajectories. Most of these trajectories are in the upper and lower corners of the outer conductor where the field is weakest. The lower generation particles (red, dark blue, magenta) are concentrated in the middle of the gap which is the high field region. This is expected because over time the electrons diffuse to lower field regions according to the field profile of the structure.

Note that all simulations were initialized with only 50 seed particles which shows the efficiency of this multipactor model when compared to other models that require around 500 particles for convergence (FEST [26]) or even 1000 particles (MEST [7],[31]) and even up to many thousands of particles (MDS [36]) for good results for similar rectangular based structures.

To enable a better understanding of the particle behavior during breakdown Fig.5.10 shows different stages of the breakdown as time increases in the same simulation. The simulation was done at $1200Vp$ in order to be in deep multipaction. Fig. 5.10 A and B shows the particle trajectories for the first few generations. The seed particles were placed in the center of gap on the left. Note that due to the strong field intensity most of the electrons are oscillating between the gap in this region. Although a few electrons have travelled to other regions in the early stages of the breakdown the plasma is localized. Note that since the operating regime is now inside the multipaction boundary, the particle trajectories are not as curved as in lower voltages. Comparing the shape of trajectories between Fig. 5.10 and Fig. 5.9 or even Fig. 5.8, it can be seen that trajectories at $1200Vp$ are much more straight and focused. This is because the field intensity is so strong it overpowers the energy of the electrons and drives them back and forth between the inner and

outer conductor walls according to the phase of the RF field. Most of the particles in the early stages do not have the ability to escape this region which is why the particle density in A and B are exactly where the seed particles were placed. This is a very strong indication that this operation point is deep within the multipaction boundary, and the particle growth will be exponential in a very short period of time.

As time increases however, it is inevitable that some particles will escape the region due to the statistical nature of this phenomenon. Some of the other multipactor codes would focus only on a specific region, and assume that particles that leave this region to be lost since they have escaped the region of multipaction. Their argument is that if particles leave the region, they will eventually decelerate whereby they either will take part in low energy impacts or get absorbed into the walls. While this is true, the model developed in this research continues to track particles outside the region, and the emergence of additional multipacting regions can been seen in Fig. 5.10C and D. A few of the secondary electrons that escaped from the high density region in A, have now created two more breakdown regions that are clear in D. Another interesting note when compared to Fig. 5.9 and Fig. 5.8 is that relatively few particles drift into the low field region of the structure. This is because the operating regime is now in deep multipaction that the field intensity is so large it is extremely difficult for the particles to escape to low field regions. Instead when particles escape one high field region, they are almost immediately driven to another high field region, completely bypassing the low field region in between. This trend is clearly seen in Fig. 5.10C and D as shown by the extremely few particles in the corner regions (lower field regions) of the structure. When comparing the electron density between the corner-low field regions in Fig. 5.10C which is in deep multipaction and the same region in the diagram for $950Vp$ which is at the onset of multipaction, this very interesting trend is clearly shown.

To summarize, although electron drift is the primary reason the breakdown voltage is higher when compared to the parallel plate predictions made by ESA, one multipaction is underway, electron drift does not seem to have a major effect. It can be said from the analysis stated in this section that the primary effect of electron drift, then is to delay the onset of multipaction to much higher breakdown levels.

5.4 Contributions of Multipactor Model

Since the particle trajectory information is critical in determining the onset of multipactor breakdown, most multipactor models can only analyze selected structures due to limitations in their modelling approach. Additionally, according to published results most multipactor models require a large number of seed particles to converge to accurate results for multipactor prediction.

The generalized approach taken during the course of this research has used key techniques to address the limitations of other multipactor models in recent

development. Section 5.4.1 briefly summarizes these key techniques. Section then summarizes how the key techniques contribute to the main contributions of this research.

5.4.1 Key Techniques

In order to address the limitations of current multipactor models described throughout this thesis, the multipactor model developed in this research has used the following key techniques:

1. Abstraction of EM field analysis from the multipactor model itself, to any industry accepted standard commercial EM solver such as Ansoft HFSS.

2. Advancement of time and phase approach that requires only one CEM simulation at a specific time step to predict the multipactor breakdown level of the structure. The time and phase of the EM field within the structure are advanced then within the model itself since multiple simulations with the CEM to predict multipactor breakdown is impractical.

Additionally, in order for the multipactor model developed in this research to be used for complex arbitrary geometries, it was found that the secondary emission model had to be quite robust and come as close as possible to representing the actual physical process of secondary emission. As a result, this multipactor model does not use many of the simplifying assumptions employed by other multipactor models. In order to accurately predict the breakdown level of complex RF structures the following key techniques were considered in the SEM:

1. The careful modeling of the inelastically and elastically reflected primary electrons such that the susceptibility curves for multipactor breakdown are broadened. This effect cannot be predicted by many other models [8],[30],[26] since they do not account for high energy reflected primary particles.

2. The individual tracking of secondary electrons such that no enhanced counter function or macro-particle approach is used, resulting in more accurate modeling of particle trajectories in fringing fields and non-uniform fields. This is because this model maintains the probabilistic nature of the emission process that significantly affects breakdown levels in non-uniform field structures.

3. The emission of 'out of phase' particles that result in an enlarged phase-range and the lowering of the multipactor breakdown level [43]. This is a more realistic representation of the secondary emission process, and with some extra analysis could be used to model hybrid multipactor modes.

4. Coupling of primary impact energy with the energy distribution of the secondary electron emission energy to provide a realistic range of energies for particle emission. Without this consideration, some model use a very narrow-band approximation of energies as in [46] and [5], which is not a realistic representation of the physical emission process.

5.5 Key Contributions

The key techniques used in the multipactor model developed in this research has three main contributions that are summarized below:

1. The first contribution of this research is that this multipactor model could be used to predict the multipactor breakdown level for complex geometries that cannot be analyzed using other multipactor models in recent development. This is because:

   (a) The multipactor model includes the effects of high energy primary electrons, out of phase electron emission and the coupling of primary impact energy with secondary emission energy. Macroparticle simplifications are also not made in this model, and taken together the inclusion of all these techniques allows for a highly accurate representation of the physical emission process. Therefore this model can accurately model the multipactor discharge in difference scenarios, for example in non-uniform field structures and even in fringing fields since the model accounts for the 'electron drift' effect.

An additional note must be made here. Since the field information of the RF device is calculated using any Commercial Electromagnetic Simulator (CEM), the multipactor model developed in this research can function independently of geometry (i.e. for complex structures) as long as the boundary conditions are imported into the model. Therefore an additional 'plugin' would be required to extract the boundary conditions (i.e the walls of the structure) from the CEM solver. Once these boundary locations can be extracted from the CEM, the model can be used as presented in this thesis since it is a generalized approach. Note that the task of creating this 'boundary extraction' plugin is simply a matter of programming and in essence is a relatively trivial task. This will be part of the future work of this research.

2. The second contribution of this research is that the multipactor model converges to accurate multipactor prediction results with significantly fewer seed particles when compared to other models. This is because the generic approach used during the course of this research enabled the inclusion of advanced emission effects such as high energy primary electrons, out of phase

electron emission and the coupling of primary impact energy with secondary emission energy and subsequently the electron drift effect. The inclusion of these effects results in a vigorous and robust SEM that converges to accurate breakdown results when compared to other multipactor models.

For example, simulations in MDS have required 100,000 seed particles [36], convergence in FEST multipactor model depends on the number of seed particles used in the simulation, however, FEST requires around 500 particles for rectangular structures[26]. MEST has published requirements of 1000-2000 particles for rectangular structures [31]. In comparison, results using this model have converged to accurate breakdown results for just 50 particles. The reason for this is that due to the probabilistic nature of the emission process, other models require a much larger sample set of seed particles to obtain accurate results since those models do not account for all the phenomenological characteristics of the secondary emission process that are included in this research. Therefore, to compensate for this inaccuracy, other models require more seed particles for convergence of their results

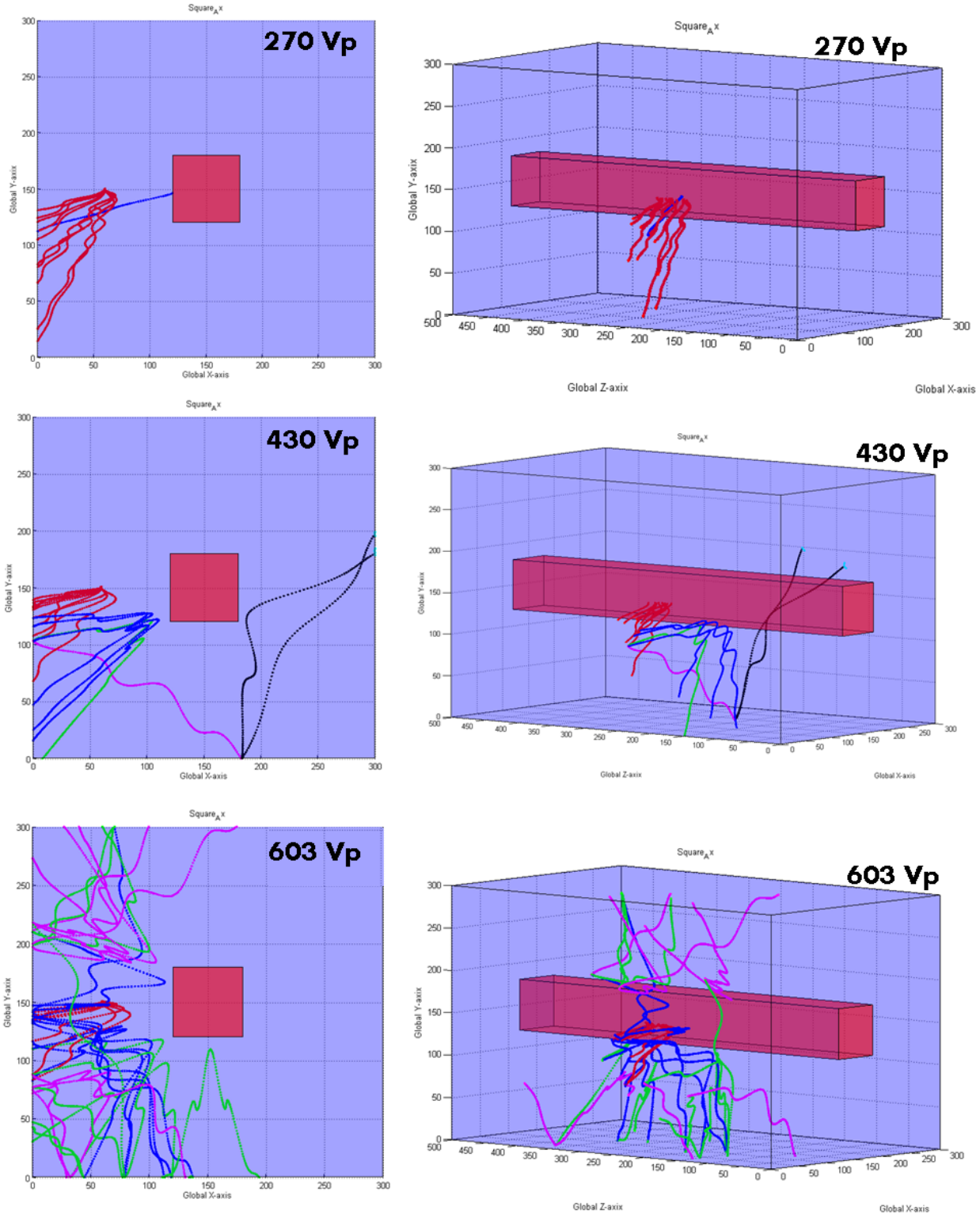

Figure 5.8: Figure 7.6: Particle Trajectories in SQ-AX [OC=300mil, IC=60mil Freq. =1.5 GHz Voltage = 270Vp-603Vp]

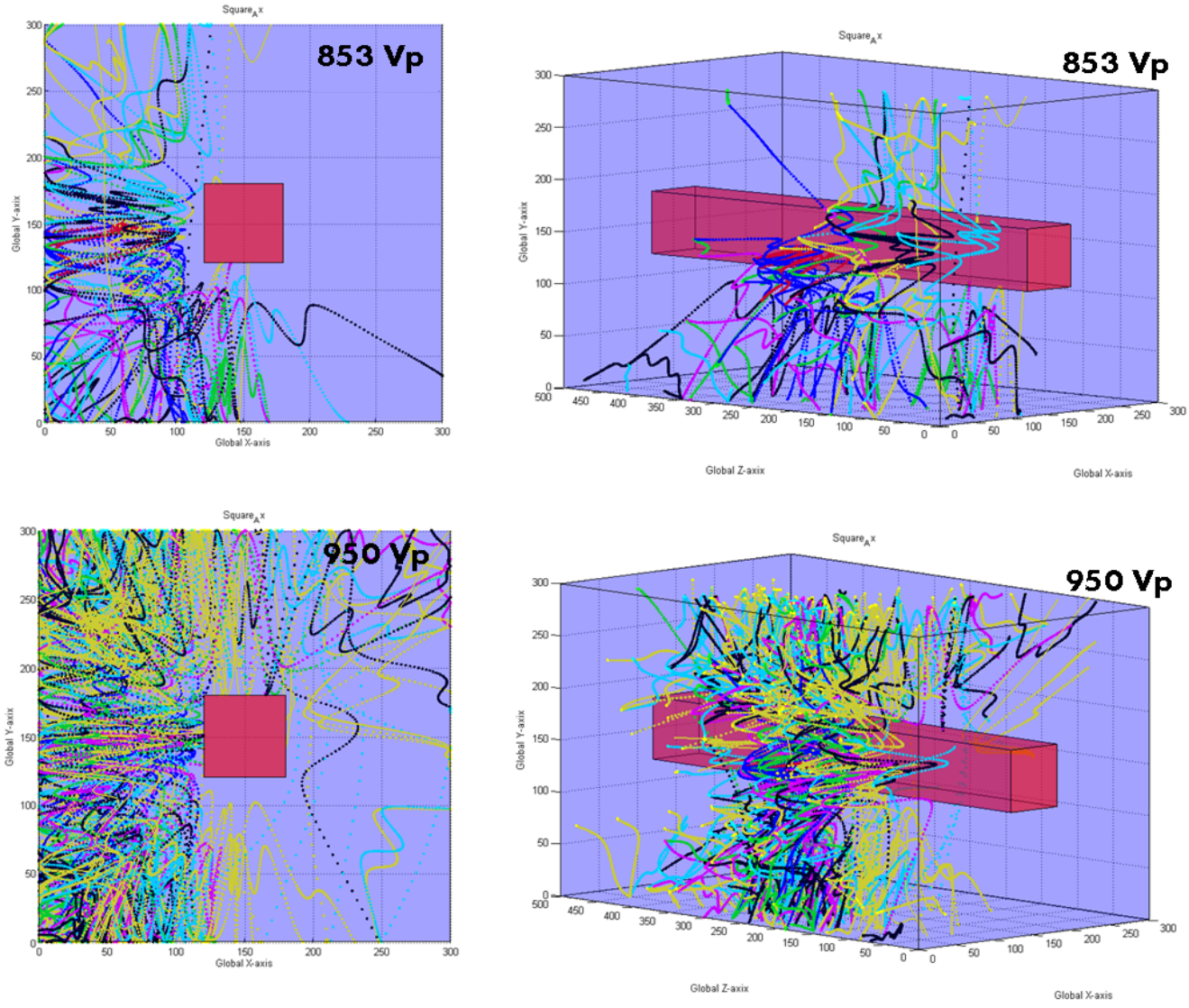

Figure 5.9: Particle Trajectory in Sq-Ax [OC=300mil, IC=60mil Freq. =1.5 GHz Voltage = 853Vp-950Vp]

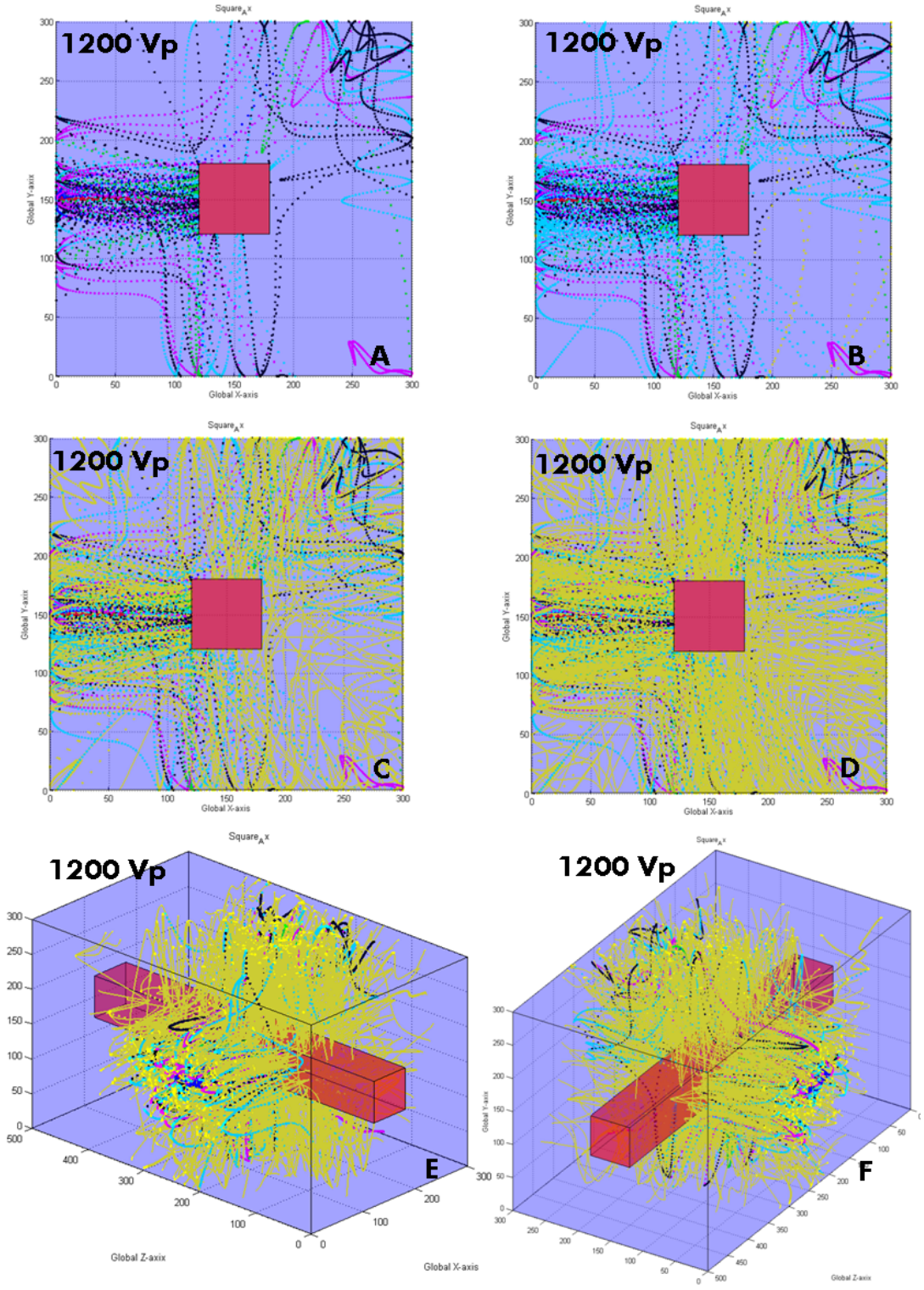

Figure 5.10: Particle Trajectories for third order multipaction breakdown in SQ-AX [OC=300mil, IC=60mil] at 1.5 GHz and 1200 Vp

Chapter 6

Conclusion and Future Work

6.1 Contribution of Research

In this research work, a generalized procedure was used to develop a multipactor model that is simplified, efficient and could be used to analyze more complex structures when compared to other multipactor models in development.

The first contribution of this research is that the approach taken in developing the multipactor model, abstracts the complexity of the EM field analysis from the multipactor model itself, and moves it to any industry accepted standard commercial EM Solver such as Ansoft HFSS. This allows this multipactor model to be used with a higher degree of confidence within the space industry since this model leverages the accuracy of industry standard EM solvers. As a result this model is expected to be well-received within the space industry.

The second contribution of this research is that the model takes into consideration many aspects of the physical process of secondary emission that other multipactor models do not consider. The result is a very robust secondary emission model that converges to accurate results with significantly fewer seed particles when compared to other models. Therefore this model is less computationally intensive, yet more accurate than other models due to the advanced secondary emission modeling techniques used in this research. For example, simulations in MDS have required 100,000 seed particles [36], convergence in FEST multipactor model depends on the number of seed particles used in the simulation, however, FEST requires around 500 particles for rectangular structures[26]. MEST has published requirements of 1000-2000 particles for rectangular structures [31]. The multipactor model developed in this research converges to accurate breakdown results with as little as 50 particles for the same structures as used in other models.

The third contribution of this research is that this multipactor model could be used to predict multipactor breakdown in any arbitrary microwave device. Previous work on multipactor models are tightly integrated with specialized EM solvers. This means that other models can only analyze selected geometries within the

EM solver's library. Due to the generalized approach taken in this research, the application of this model is not limited to selected geometries but rather could potentially be applied to more complex microwave structures that are of commercial use within the space industry.

6.2 Conclusion

This work focused on developing a generalized procedure for a multipactor model that can efficiently predict the breakdown levels of complex structures that are found in the space-industry.

The secondary emission model was quite challenging to design, however a robust SE model was finally developed that accounts for many of the complexities in the physical secondary emission process, that is not considered by other multipactor models.

This multipactor model also abstracts the complexity of the EM field analysis from the multipactor model itself, and moves it to any industry accepted standard commercial EM Solver such as Ansoft HFSS. This allows this multipactor model to leverage the accuracy of industry standard EM solvers, while greatly simplifying the process of multipactor prediction. Additionally, due to the generalized approach taken during the development of the secondary emission model, this model could potentially be used to predict multipaction in geometrically complex structures used within the space industry.

The model developed in this research takes into consideration many aspects of the physical process of secondary emission that other multipactor models do not consider. Therefore this model converges to prediction results with significantly fewer seed particles when compared to other models. It has been shown that this model converges to accurate breakdown results with as little as 50 particles for the same or more complex structures as used in other models. Other models require anywhere from 500 particles [31],[26] to a 100,000 particles [36].As a result this model is less computationally intensive, yet more accurate than other models due to the advanced secondary emission modeling techniques used in this research.

Results of multipactor breakdown levels for rectangular waveguide and square axial transmission lines were found to be in good agreement with ESA curves and models by Sazontov et.al., in cases where the uniform field approximation hold true (i.e. low order multipaction in RWGs and low impedance square axial transmission lines).

In other simulations such as high impedance square-axial transmission lines or high order waveguide multipaction simulations the results between the models deviate noticeably. The reason for this is the different electron dynamics in the secondary models chosen by each model. Since the model developed in this research considers advanced secondary emission characteristics, it is able to more accurately

predict the multipactor breakdown levels for the aforementioned structures, with far fewer seed particles.

Also, differences between the model developed in this research and some of the other models in development include the ability to account for backscattered primaries and rediffused primaries which is a noticeable phenomenon in multipaction testing and has been revealed by empirical current measurement during breakdown. In summary, simulation results show that the models developed are quite robust, as numerous cases were run for the different structures with no errors and good results.

6.3 Future Work

Although different structures have been simulated using this code, more irregular shaped structures found in industry should tested, although a few modifications will have to be made to the boundary condition engine first. The secondary emission models used in the code are extensive, but the model tracks each particle independently from each other. That is, space charge or electron cloud effects are not considered. This means that the electron dynamics between the electrons such as mutual repulsion that causes the saturation phenomenon in breakdown cannot be modelled. Including this effect would give invaluable insight into the behavior of the plasma that is created during breakdown and how it affects the scattering parameters and generates noise and harmonics in the microwave device. In addition, the magnetic field information could also be added to the equations of motion in order to predict breakdown for very high orders of multipaction. Finally, since the secondary models are completely probabilistic, numerous distribution functions are used to assign secondary electron yield, energy and direction. Some of the major distribution functions used in many models include uniform distribution, Poisson distribution and Maxwell distribution to name a few. An advanced feature would allow the user to define the probability distribution functions to be used in the simulation, to observe the effect each distribution has on particle trajectory and eventually predicted breakdown levels. This has large implications for academic research in secondary emission modelling. The same could be done for the numerical engine in that the numerical integrator could be user defined between Runge-Kutta, Velocity Veret, Leap Frog or even more exotic numerical integrators. The differences between the accuracy and computation time in the context of studying multipaction breakdown has not been studied yet in any detail.

References

[1] M.Furman and M. Pivi, "Probabilistic models for the simulation of secondary emission," *Physical Review Special Topics-Accelerators and Beams*, 2002.

[2] A. Woode and J. Petit, "Design data for the control of multipactor discharge in spacecraft microwave and rf systems," *Microwave Journal*, vol. 35, pp. 142–155, 1985.

[3] D. Grosso, "Scrubbing process of cu surfaces induced by electron bombardment," *Proceedings of European Particle Accelerator Conference*, pp. 1619–1621, 2008.

[4] J. Vaughan, "Multipactor," *IEEE Transactions on Electron Devices*, vol. 35, pp. 1172–1180, 1985.

[5] A. Perez, C. Vicente, and C.Tienda, "Multicoax: A software tool for predicting multipactor rf breakdown," *Procedings of the 5th International Workshop on Multipactor, Corona and Passive Intermodulation in Space RF Hardware (MULCOPIM)*, pp. 27–34, 2005.

[6] C. Vicente and M. Mattes, "Multipactor breakdown prediction," *IEEE Trans. Elec. Devs.*, pp. 1055–1058, 2005.

[7] J. de Lara and F. Perez, "Cest and mest: Tools for the simulation of radio frequency electric discharges in waveguides," *Simmulation Modeling Practice and Theory*, pp. 1438–1452, 2008.

[8] E. Somersalo, "Electron multipacting in rf structures," *TESLA Report*, 1994.

[9] C. Vicente, "Microwave breakdown prediction in rectangular waveguide based components," *IEEE MTT-S International Microwave Symposium Digest*, pp. 17–20, 2005.

[10] G. Francis and A. Engel, "Growth of the high-frequency electrodeless discharge," *Mathematical and Physical Sciences*, vol. 246, pp. 143–180, 1952.

[11] S. Riyopoulos, D. Chernin, and D. Dialetis, "Theory of multipactor in crossed fields," *Phys. Plasmas*, vol. 2, pp. 3194–3213, 1995.

[12] M. Alfonseca, "Langevin simulation of rf corona discharges for space hardware," *5th International Workshop on Multipactor, Corona and Passive Intermodulation in Space RF Hardware*, vol. 112, pp. 681–685, 2005.

[13] H. Selier, "Secondary electron emission in scanning electron microscope," *J. Appl. Phys*, vol. 54, 1983.

[14] D. Chernin, A. Drobot, and M. Kress, "A model of secondary emission for use in computer simulation of vacuum electronic devices," *IEEE International Technical Digest, Electron Devices Meeting*, pp. 773–776, 1993.

[15] R. Udiljak, "Multipactor in low pressure gas and in nonuniform rf field structures," *PhD Thesis-Chalmers University of Technology Sweden*, 2007.

[16] R. Vaughan, "Secondary emission formulas," *IEEE Trans. Elec. Devices*, vol. 40, pp. 1963–1967, 1993.

[17] L. Myers, "Electron optics theoretical and practical," *Chapman and Hall*, pp. 309–325, 1939.

[18] M. Greenblatt, "A scintillation counter for thermal neutrons," *Rev. Sci. Instr*, vol. 20, p. 646, 1949.

[19] A.Hatch, "Electron bunching in the multipacting mechanism of high frequency discharge," *Journal of Applied Physics*, vol. 32, p. 1086, 1961.

[20] J. Sombrin, "Effect multipactor," *CNES Technical Report*, vol. 83, 1983.

[21] A.Hatch and H.Williams *The Physical Review*, vol. 112, pp. 681–685, 1958.

[22] A. Woode and J. Petit, "Diagnostic investigations into the multipactor effect and susceptibility zone measurements and parameters affecting a discharge," *ESTEC Working Paper*, 1989.

[23] R. Woo, "Final report on rf voltage breakdown in coaxial transmission lines," *Jet Propulsion Laboratory Working Report, NASA*, 1970.

[24] E. Gjonaj, "Particle-in-cell simulations: techniques and applications," *Proceedings on OCPEM Workshop*, 2003.

[25] V. Boria. and B. Gimeno, "Waveguide filters for satellites," *IEEE Microwave Magazine*, pp. 60–70, 2007.

[26] C. Vicente, "Fest3d-a simulation tool for multipactor prediction," *Procedings on the 5th International Workshop on MULCOPIM*, 2005.

[27] D. Wolk and C. Vicente, "An investigation of the effect of fringing fields on multipactor breakdown, breakdown," *5th International Workshop on Multipactor, Corona and Passive Intermodulation in Space RF Hardware*, pp. 12–15, 2005.

[28] S. Anza and C. Vicente, "Enhanced prediction of multipaction breakdown i passive waveguide components including space charge effects," *IEEE MTT-S International Microwave Symposium Digest*, pp. 1095–1098, 2008.

[29] S. Humphries and N. Dionne, "Modeling secondary emission in a finite element multipactor code," *Proceedings of the 9th Workshop on RF Superconductivity*, pp. 390–396, 1999.

[30] S. Humphries and D. Rees, "Electron multipactor coe for high power rf devices, electron multipactor code for high-power rf devices," *Proceedings of Particle Accelerator Conference*, pp. 2428–2430, 1997.

[31] J. de Lara and F. Perez, "Multipactor prediction for on-board spacecraft rf equipment with the mest software tool," *IEEE Transactions on Plasma Science*, pp. 476–484, 2006.

[32] M. Gusarova and V. Kaminskii, "Evolution of 3d simulation multipactoring code multp," *Problems of Atomic Science and Technology*, pp. 123–126, 2008.

[33] F. Krawczyk, "Status of multipacting simulation capabilities for scrf applications," *Proceedings on the 10th workshop on RF Superconductivity*, 2001.

[34] L. Kravchuk and G. Romanov, "Multipactoring code for 3d accelerating structures," *20th International LINAC Conference*, 2000.

[35] A. Sazontov, D. Anderson, N. Vdocicheva, and M. Buyanova, "Simulations of multipactor zones taking into account realistic properties of secondary emission," *Proceedings of 4th International Workship on MULCOPIM*, 2003.

[36] J. Peuch, "Research activities on microwave discharge phenomena," *MULCOPIM 2005*, 1998.

[37] D. M. Pozar, *Microwave Engineering*. J. Wiley and Sons, 2005.

[38] K. McKay, "Secondary electron emission," *Advances in Electronics*, vol. 1, 1948.

[39] R. Lye and A. Dekker, "Theory of secondary emission," *Phys Rev*, vol. 107, pp. 977–981, 1957.

[40] A. Beck and H. Ahmed, *An Introduction to Physical Electronics*. Hodder and Stoughton Educational, 1968.

[41] A. Shih and C. Hor, "Secondary emission properties as a function of the electron incidence angle," *IEEE Trans. Elec. Devices*, vol. 40, pp. 824–829, 1993.

[42] T. Moller and J. Hughes, "Effieciently buildings a matrix to rotate one vector to another," *Journal of Graphics Tools*, vol. 4, 2000.

[43] R. Seviour, "The role of elastic and inelastic electron reflection in multipactor discharges," *IEEE Transactions on Electron Devices*, vol. 52, pp. 1927–1930, 2005.

[44] T. Everhart and M. Chung, "Role of plasmon decay in secondary electron emission in the nearly-free-electron metals," *Phys. Rev. B*, 1977.

[45] C. de Lara, "Multipactor electron simulation tool (mest)," *IEEE Tans*, pp. 547–550, 2004.

[46] J. Han, "Secondary electron emission in photocathod rf gun," *Physical Review special topics - Accelerators and Beams*, 2005.

[47] K. Spangenberg, *Vacuum Tubes*. McGraw-Hill, 1948.

[48] E. Somersalo, "Computational methods for analyzing electron multipacting in rf structures," *Particle Accelerators*, pp. 107–141, 1998.

[49] R. Geng, "Multipacting simulations for superconducting cavities and rf coupler waveguides," *IEEE Proceedings of Particle Accelerator Conference*, pp. 264–268, 2003.

[50] J. Dormand and P. Prince, "A family of embedded runge-kutta formulae," *Journal of Computational and Applied Mathematics*, vol. 6, pp. 19–26, 1980.

[51] G. Devanz, "A 2d multipactor simulator code for rf components and accelerating cavities," *Proceedings of EPAC*, pp. 1366–1368, 2000.